Modélisation du problème direct de la magnéto et électroencéphalographie : méthodes numériques et calibration.

Sylvain Vallaghé

PhD THESIS

prepared at
INRIA Sophia Antipolis

and presented at the
University of Nice-Sophia Antipolis
Graduate School of Information and Communication Sciences

A dissertation submitted in partial fulfillment of the requirements for the degree of

DOCTOR OF SCIENCE
Specialized in Control, Signal and Image Processing

EEG and MEG forward modeling : computation and calibration

Sylvain VALLAGHÉ

Advisor	Dr. Maureen Clerc	Ecoles des Ponts et Chaussees, France
Reviewers	Pr. Carsten Wolters	University of Muenster, Germany
	Pr. Jens Haueisen	Technical University Ilmenau, Germany
Examiners	Pr. Stéphane Lanteri	INRIA Sophia Antipolis, France
	Pr. Valérie Perrier	University of Grenoble, France
	Dr. Fabrice Wallois	University of Picardie, France

UNIVERSITÉ NICE-SOPHIA ANTIPOLIS - UFR Sciences

École Doctorale STIC
(Sciences et Technologies de l'Information et de la Communication)

THÈSE

pour obtenir le titre de
DOCTEUR EN SCIENCES
de l'UNIVERSITÉ de Nice-Sophia Antipolis
Discipline: Automatique, Traitement du Signal et des Images

présentée et soutenue par

Sylvain VALLAGHÉ

Modélisation du problème direct de la magnéto et électroencéphalographie : méthodes numériques et calibration.

Thèse dirigée par Maureen CLERC

Sountenue le 8 décembre 2008

Composition du jury:

Rapporteurs	Dr. Carsten Wolters	Université de Muenster, Allemagne
	Pr. Jens Haueisen	Technical University Ilmenau, Allemagne
Examinateurs	Pr. Stéphane Lanteri	INRIA Sophia Antipolis, France
	Pr. Valérie Perrier	Université de Grenoble, France
	Dr. Fabrice Wallois	Université de Picardie, France

Contents

Présentation générale

CONTEXTE DE CE TRAVAIL

L'étude des mécanismes du cerveau qui sous-tendent la cognition (perception, motricité, langage, mémoire) est un domaine de recherche couramment désigné sous le nom de neurosciences cognitives. Dans ce domaine, un enjeu important pour la compréhension du cerveau est de mettre en relation la fonction avec la localisation, autrement dit de comprendre quelles zones du cerveau sont impliquées dans le traitement d'une tâche bien précise. Les premiers résultats de localisation proviennent de la neuropsychologie, grâce a l'étude des changements comportementaux dues à une lésion cérébrale bien localisée, et des techniques d'électrophysiologie, qui consistent à mesurer l'activité électrique des neurones par l'implant d'électrodes dans le cerveau (le plus souvent chez l'animal). Les progrès dans la localisation des fonctions cérébrales sont aujourd'hui fortement liés à l'utilisation de plusieurs techniques d'imagerie cérébrale qui permettent d'étudier le cerveau humain de manière quasi non-invasive, et donc de procéder à des expériences sur de nombreux sujets, même sains.

Les techniques de neuroimagerie structurelle sont apparues au début des années 70 avec le scanner à rayons X, puis se sont développées avec l'apparition de l'IRM dans les années 80. Ces modalités génèrent une image 3d contrastée des différentes parties de l'anatomie du cerveau, et en particulier permettent d'identifier la localisation et l'extension d'une lésion cérébrale. Dans le cadre de la recherche en neurosciences cognitives, l'imagerie structurelle apporte des éléments pour interpréter les observations comportementales en neuropsychologie. En déterminant à quelles lésions correspond un déficit cognitif donné, il est possible d'établir que la région cérébrale lésée intervient dans le mécanisme sous-jacent.

La neuroimagerie fonctionnelle dépasse la simple image anatomique et cherche à caractériser le cerveau en action. Son utilisation classique en neurosciences cognitives consiste à faire effectuer une tâche à un sujet et à mesurer l'activité cérébrale corrélée à cette tâche. Suivant les techniques d'imagerie fonctionnelle, il est possible de retrouver plus ou moins précisément quelle region du cerveau etait activée et à quel moment. Sachant que l'activité cérébrale est essentiellement électrique, on peut distinguer deux groupes parmi ces techniques :

- **Les méthodes métaboliques**
  Ces méthodes permettent de mesurer un changement du métabolisme relié à l'activité cérébrale. La plus connue est l'imagerie par résonance magnétique fonctionnelle (IRMf), qui permet de mesurer le taux d'oxygénation du sang dans le cerveau. Dans les régions qui consomment de l'énergie, l'afflux de sang oxygéné augmente et donc l'IRMf permet de localiser les régions de forte activité cérébrale. La technique de l'IRMf permet de générer une image 3d précise, mais le temps d'acquisition est de l'ordre d'une seconde : une suite temporelle d'images IRMf n'a donc pas la résolution nécessaire pour suivre en détails la dynamique des processus cognitifs (de l'ordre de 10 ms). On peut également citer la technique de tomographie par émission de positrons (TEP) qui mesure les modifications de débit sanguin par injection d'un traceur radioactif. Cette technique est de moins en moins utilisée en neurosciences cognitives car elle a une résolution temporelle encore plus faible que l'IRMf.

- **Les mesures directes de l'activité électrique**
  La technique la plus connue, l'électroencéphalographie (EEG), est en fait la

toute première méthode de neuroimagerie non invasive. Sa mise au point date de 1929, par le neurologue Hans Berger. Son principe consiste à mesurer le potentiel électrique à la surface de la tête d'un patient, à l'aide d'un casque muni d'électrodes. En dehors de toute autre source électrique artificielle, le potentiel électrique mesuré est censé provenir seulement de l'activité électrique du cerveau. Son avantage en comparaison des méthodes métaboliques est que la résolution temporelle est uniquement limitée par l'électronique de mesure, et typiquement le signal est mesuré avec une fréquence d'échantillonage de 5 kHz, bien supérieure à la dynamique de l'activité cérébrale. La magnétoencéphalographie (MEG) est une technique très similaire à l'EEG, mais elle mesure autour de la tête le champ magnétique au lieu du potentiel électrique. Son intérêt réside dans le fait que, contrairement au potentiel électrique, le champ magnétique est peu déformé par son passage au travers des tissus organiques (notamment le crâne).

Ainsi, grâce à leur haute résolution temporelle, l'EEG et la MEG offrent théoriquement la possibilité de suivre en détails les processus de la dynamique de l'activité cérébrale. Une caractéristique de ces mesures vient pourtant limiter leur capacité d'imagerie : ce sont des mesures de surface qui en tant que telles ne donnent qu'une information grossière sur la localisation de l'activité électrique ayant généré le champ électromagnétique mesuré. Pour pouvoir estimer la position des sources du signal électromagnétique, il faut recourir à des méthodes mathématiques d'analyse du signal. Ce problème de localisation de source rentre dans une catégorie de problèmes mathématiques désignés sous le nom de problèmes inverses, qui ont en général la caractéristique d'être mal posés : le nombre de mesures est insuffisant pour déterminer parfaitement la position des sources du signal. La résolution de ce problème inverse passe par une étape initiale de modélisation du phénomène étudié, dite problème direct. Dans le cas de l'EEG et de la MEG, le phénomène étudié est la propagation du champ électromagnétique depuis une source localisée dans le cerveau jusqu'aux capteurs situés à la surface de la tête du patient. La qualité de la modélisation de ce phénomène influe directement sur la précision des méthodes de localisation de source. Il est donc nécessaire dans cette étape de modélisation de se rapprocher au plus près des caractéristiques réelles de propagation du champ électromagnétique à travers les différents tissus organiques qui composent la tête.

Le travail de cette thèse s'inscrit dans cette étape de modélisation. Les enjeux actuels de la modélisation du problème direct se situent à deux niveaux :

- La propagation du champ électromagnétique est décrite par des equations aux dérivées partielles (EDP). Dans des milieux décrits par des géométries complexes, comme c'est le cas pour les modèles de tête obtenus à partir d'IRM structurelles des patients, la résolution de ces EDP nécessite l'utilisation de méthodes numériques souvent coûteuses en mémoire et en temps de calcul. Cela est un frein à l'utilisation de géométries complexes qui décrivent avec précision la géométrie de la tête, et la plupart des expérimentateurs en EEG et MEG utilisent encore des descriptions sphériques de la tête, pour lesquelles les solutions des EDP du champ électromagnétique sont facilement calculables.

- Les conductivités électriques des tissus organiques qui composent la tête sont mal connues, alors que ces propriétés affectent la propagation du champ électro-

magnétique (en particulier le potentiel électrique). Dans la plupart des modèles de tête, les valeurs de conductivités utilisées proviennent de mesures *in vitro* des tissus, et ne rendent pas compte de la réalité des tissus dans leur milieu naturel. Afin que les modèles de tête reproduisent au mieux la réalité, des méthodes non invasives d'estimation de conductivité *in vivo* sont développées.

Dans cette thèse, nous présentons des contributions originales sur les deux aspects de la modélisation du problème direct. L'organisation du manuscrit se compose d'une introduction et de deux parties. L'introduction est censée donner au lecteur un aperçu rapide du domaine de recherche lié à l'imagerie fonctionnelle avec l'EEG et la MEG. Une emphase particulière est mise sur la modélisation du problème direct, qui conclut cette introduction. La première partie présente nos contributions sur les méthodes pour la résolution numérique des EDP du champ électromagnétique dans des géometries complexes. La seconde partie quant à elle s'intéresse au problème des conductivités dans les modèles de tête en EEG et MEG.

PRÉSENTATION DU MANUSCRIT

Introduction

Cette partie permet de comprendre la nature des signaux observés en EEG et MEG, quelles sont les méthodes pour localiser les sources de ces signaux et enfin comment se déroule le processus de modélisation du problème direct.

Le **chapitre 1** expose les bases du signal mesuré en EEG et MEG. La section 1 explique quels sont les mécanismes physiologiques à la base de l'activité électrique des neurones du cerveau. Nous expliquons ensuite dans la section 2 comment le champ électromagnétique produit par l'activité électrique du cerveau peut être mesuré à la surface de la tête. Enfin nous illustrons en section 3 le problème de l'échelle des sources observables en EEG et MEG qui dépasse la taille du simple neurone.

Le **chapitre 2** présente les caractéristiques de l'EEG et de la MEG lorsqu'elles sont utilisées en tant que modalités d'imagerie fonctionnelle. La section 2 illustre le type de mesures que l'on peut observer en EEG et MEG, et le problème inverse de localisation de sources est ensuite expliqué (section 3). La localisation de sources dépend de l'hypothèse que l'on fait sur la distribution de l'activité cérébrale, ce qui conduit à différents modèles de sources (section 4). Enfin, nous présentons dans la section 5 les méthodes les plus couramment utilisées en localisation de source.

Le **chapitre 3** développe en détails les différentes approches pour la modélisation du problème direct. Nous rappelons tout d'abord les équations classiques d'électromagnétisme qui s'appliquent dans le cas de l'EEG et la MEG (section 1). Nous expliquons ensuite comment résoudre ces équations dans des géométries de plus en plus complexes : un milieu infiniment homogène (section 2), un conducteur à géométrie sphérique (section 3) et enfin des géométries réalistes de la tête (section 4). Un concept utile pour le calcul du champ électromagnétique dans le cas de l'EEG et de la MEG est la réciprocité : il permet d'intervertir la position des sources et des capteurs. Ce concept est expliqué dans la section 5. Enfin nous présentons le problème du choix des conductivités dans les modèles de tête (section 6).

Première partie - Résolution du problème direct

Cette première partie concerne les méthodes de résolution du problème direct dans des géométries réalistes et complexes. Dans le chapitre 4, nous présentons une nouvelle méthode par éléments finis utilisant une simple grille cartésienne comme maillage du domaine, tout en gardant une description précise de la géométrie grâce aux représentations par fonctions implicites des différents tissus composant la tête. Dans le chapitre 5, nous utilisons la méthode de l'adjoint afin de dériver des EDP réciproques générales, applicables en EEG et MEG pour tout type de capteur.

Chapitre 4 - Représentations implicites pour la méthode des éléments finis

Habituellement, résoudre le problème direct par la méthode des éléments finis (FEM) nécessite de réaliser un maillage qui suit la géométrie du domaine considéré. L'approche la plus commune est de construire un maillage tétrahédrique. La construction de ce maillage doit à la fois respecter la géométrie et certains critères de qualité numérique (homogénéité des tétrahèdres). Les méthodes automatiques de génération de maillage créent parfois des défauts qui nécessitent une interaction de la part de l'utilisateur afin d'assurer la qualité finale du maillage. Le procédé de création de maillage est donc parfois laborieux. A l'inverse, si le problème direct est résolu par la méthode des différences finies (FDM), seulement une grille cubique du domaine est nécessaire. De plus, cette grille peut etre directement adaptée depuis la grille d'une image IRM du sujet. L'étape compliquée du maillage est donc évitée. Cependant, la description de la géometrie du domaine est moins bonne que dans le cas de la FEM, puisque les différents tissus sont alors décrits par des domaines "en escalier". Nous proposons donc une méthode qui combine à la fois la simplicité de la grille cubique de la FDM avec la description précise de la géometrie obtenue avec la FEM. C'est en fait une méthode éléments finis, où les fonctions de bases sont trilinéaires par morceaux, correspondant à l'interpolation classique des images 3d sur une grille cubique. La description précise des différents tissus de la tête est alors prise en compte par l'utilisation de description implicites (levelsets) sur la grille. La pleine compréhension de ce chapitre nécessite quelques connaissances sur la méthode des éléments finis, il peut donc être utile de se référer à l'appendice A qui explique en détails la FEM tétrahédrique classique. Ce chapitre est adapté d'une publication [80] présentée au workshop *MMBIA* de la conférence *ECCV 2007*.

Chapitre 5 - EDP réciproques générales obtenues par la méthode de l'adjoint

Lorsque la solution du problème direct est calculée avec la FDM ou la FEM, on utilise l'approche réciproque afin de limiter le coût computationnel de ces méthodes numériques. Dans ce cas, on résout une EDP différente. Par exemple, en EEG, l'EDP du potentiel électrique généré par une source a l'intérieur d'un domaine Ω est :

$$\begin{cases} \nabla \cdot (\sigma \nabla V) = \nabla \cdot \mathbf{J}^{\mathrm{p}} \text{ in } \Omega \\ \sigma \nabla V \cdot \mathbf{n} = 0 \text{ on } \partial\Omega \end{cases}$$

alors que l'EDP réciproque, correspondant au potentiel généré par une injection de courant au bord du domaine, est :

$$\begin{cases} \nabla \cdot (\sigma \nabla V) = 0 \text{ in } \Omega \\ \sigma \nabla V \cdot \mathbf{n} = \delta_{\mathbf{r}_1} - \delta_{\mathbf{r}_2} \text{ on } \partial\Omega \end{cases}$$

ou $\mathbf{r}_1$ et $\mathbf{r}_2$ sont les points où le courant est injecté. Dans ce cas où l'on considère des mesures ponctuelles du potentiel électrique, l'EDP réciproque est donnée directement par le théorème de réciprocité de Helmholtz. L'EDP réciproque pour le champ magnétique ne s'obtient pas de manière aussi directe : elle a été calculée pour des mesures ponctuelles dans [74]. Dans ce chapitre, nous proposons d'utiliser la méthode de l'adjoint comme un outil général pour la formulation des EDP réciproques, aussi bien en EEG qu'en MEG. L'avantage de cette méthode est que les EDP réciproques peuvent facilement être modifiées pour intégrer des mesures non-ponctuelles, afin de prendre en compte la surface des électrodes EEG ou la géométrie des capteurs MEG (magnétomètres, gradiomètres). Ce chapitre est adapté d'un article soumis au journal *Physics in Medicine and Biology*.

Seconde partie - Calibration des conductivités

Cette seconde partie traite du problème du choix des conductivités dans les modèles directs en EEG. Nous présentons une analyse de sensibilité globale des modèles à trois couches (chapitre 6) ainsi qu'une méthode pour la calibration des conductivités avec des potentiels évoqués somesthésiques (chapitre 7).

Chapitre 6 - Analyse de sensibilité globale des topographies EEG par rapport aux conductivités

Le potentiel électrique est déformé lors de sa propagation à travers des tissus dont les conductivités électriques changent brutalement. C'est pourquoi le choix des conductivités dans un modèle électromagnétique de la tête est déterminant pour la topographie du potentiel à la surface, et affecte par la même la localisation de sources en EEG. Pour mieux comprendre quels sont les paramètres de conductivité du modèle de tête qui sont importants vis à vis des topographies EEG, il est nécessaire d'effectuer une analyse de sensibilité. Quand le modèle est linéaire par rapport à ses paramétres, une analyse de sensibilité locale est suffisante pour comprendre complètement le modèle. Mais le potentiel électrique a une dépendance fortement non-linéaire aux conductivités du modèle de tête, donc une analyse de sensibilité locale n'est pas suffisante dans ce cas. Nous présentons dans ce chapitre une analyse de sensibilité globale, qui permet de capturer toute la variabilité des topographies EEG par rapport aux conductivités. Cette analyse de sensibilité globale est basée sur des méthodes de décomposition de variance, dont les principes généraux sont expliqués dans l'appendice B. Ce chapitre est adapté d'un article soumis au journal *IEEE Transactions on Biomedical Engineering*.

Chapitre 7 - Calibration des conductivités par l'utilisation de potentiels évoqués somesthésiques

La modalité la plus courante pour l'estimation des conductivités d'un modèle direct EEG est la Tomographie par Impédance Électrique (EIT). Le principe de cette technique est d'injecter un courant sur le scalp du patient entre deux électrodes d'un casque EEG, et de mesurer le potentiel électrique ainsi généré sur les autres électrodes du casque. A partir de la donnée du courant injecté et du potentiel mesuré, la conductivité du modèle de tête peut être estimée. Dans le chapitre 6, l'analyse de sensibilité démontre que les topographies EEG ne sont pas sensibles

aux mêmes paramètres de conductivité selon que la source électrique est dans le cerveau ou sur le scalp. Par conséquent, dans une optique de localisation de sources, il semble plus intéressant de calibrer le modèle de tête avec une source électrique située dans le cortex. Nous proposons donc dans ce chapitre une méthode pour calibrer les conductivités à l'aide de potentiels évoqués somesthésiques. Ce chapitre est adapté d'une publication [101] présentée à la conférence *ISBI 2007*.

LISTE DE PUBLICATIONS

Journaux

- Sylvain Vallaghé, Maureen Clerc, "A global sensitivity analysis of three and four-layer EEG conductivity models", *IEEE Transactions on Biomedical Engineering*, 2008, accepté pour publication.
- Sylvain Vallaghé, Théodore Papadopoulo, Maureen Clerc, "The adjoint method for general EEG and MEG sensor-based lead field equations", *Physics in Medicine and Biology*, 2008, accepté pour publication.

Conférences

- Sylvain Vallaghé, Maureen Clerc, "In vivo conductivity estimation using somatosensory evoked potentials and cortical constraint on the source", *IEEE Proceedings of ISBI 07*, Washington DC, USA, 2007.
- Théodore Papadopoulo, Sylvain Vallaghé, "Implicit meshing for finite element methods using levelsets", *Proceedings of MMBIA 07*, Rio de Janeiro, Brazil, 2007.
- Sylvain Vallaghé, Maureen Clerc, "Conductivity estimation for EEG: what is relevant ?", *IEEE Proceedings of NFSI & ICFBI 07*, Hangzhou, China, 2007.

General overview

CONTEXT OF THIS WORK

The study of brain mechanisms that underlie cognition (perception, motivity, language and memory) is a research field commonly referred to as cognitive neuroscience. In this domain, an important issue for further understanding of the brain is to establish the connection between function and localization, i.e. to find what parts of the brain are involved in the processing of a particular task. The first results of localization come from neuropsychology, by studying behavioral changes due to a well localized cerebral lesion, and electro-physiology technologies, that consist in measuring neurons electrical activity by implanting electrodes in the brain (mostly on animals). Nowadays, advances in the brain function localization are strongly linked to the use of several neuroimaging techniques that allow to study the human brain in an almost noninvasive way, and so to perform experiments on many subjects, even healthy.

Structural neuroimaging technologies appeared at the beginning of the seventies with x-ray Computed Tomography (CT), then developed with the arrival of MRI in the eighties. These methods generate a contrasted 3D image of the brain anatomy, and in particular allow to identify the localization and the extension of a cerebral lesion. Within the framework of cognitive neuroscience research, structural imaging brings elements to interpret behavioral observations in neuropsychology. By determining to which lesions corresponds a given cognitive deficit, it is possible to establish that the damaged cerebral region is involved in the underlying mechanism.

Functional neuroimaging goes beyond the simple anatomic image and aims at characterizing the brain in action. Its classical use in cognitive neuroscience consists in making a subject execute a task and in measuring the cerebral activity correlated to this task. Depending on the functional imaging technology, it is possible to find more or less precisely which region of the brain was activated and at which moment. We can distinguish two groups among these techniques :

- **Metabolic methods**
  These methods measure a change in metabolism linked to cerebral activity. The most known is functional Magnetic Resonance Imaging (fMRI), that allows to measure the blood oxygenation level in the brain. In regions that consume energy, oxygenated blood flow increases and so fMRI allows to localize regions where a high cerebral activity is taking place. The fMRI modality generates a precise 3d image, but the acquisition time is of about one second : a temporal series of fMR images do not have a sufficient temporal resolution to follow in detail the dynamics of cognitive processes (duration of about 10 ms). We can also cite the Positron Emission Tomography (PET) that measures blood flow changes by injection of a radioactive label. This technique is less and less used in cognitive neuroscience because it has a temporal resolution even more limited than fMRI.

- **Direct measures of the electrical activity**
  The most known technique, electroencephalography (EEG), is in fact the very first noninvasive neuroimaging method. Its realization by neurologist Hans Berger dates back to 1929. Its principle consists in measuring the electric potential at the surface of the patient's head, thanks to a helmet with electrodes. Apart from all other artificial electrical sources, the electric potential

measured is supposed to be only generated by brain electrical activity. Its advantage compared to metabolic methods is that the temporal resolution is only limited by the measurement electronics, and typically the signal is measured with a sampling frequency of 1 kHz, much higher than the dynamics of cerebral activity. Magnetoencephalography (MEG) is a technique very similar to EEG, but it measures above the head surface the magnetic field instead of the electric potential. Its interest lies in the fact that, contrary to the electric potential, the magnetic field is not very distorted by its propagation through organic tissues (notably the skull).

Hence, thanks to their high temporal resolution, EEG and MEG theoretically offer the possibility to follow in detail the dynamics of cerebral activity processes. A characteristic of these measures yet limit their imaging capacity : they are surface measures that, as such, only give a crude information on the localization of electrical activity that generated the measured electromagnetic field. To be able to estimate the position of electromagnetic signal sources, one needs to have recourse to mathematical methods of signal analysis. This problem of source localization falls in a category of mathematical problems designated as inverse problems, that generally have the characteristic of being ill-posed : the number of measurements is insufficient to perfectly determine the positions of signal sources. Before solving this inverse problem, an initial modeling of the studied phenomenon is required, called forward problem. In the case of EEG and MEG, the studied phenomenon is the electromagnetic field propagation from a source in the brain to the sensors located at the head surface. The quality of the models of this phenomenon has a direct effect on the accuracy of the source localization methods. It is hence necessary to build head models that correspond as well as possible to the real electromagnetic field propagation in the organic tissues of the head.

The work presented in this thesis focuses on this electromagnetic head modeling. There are actually two main issues with regard to the forward problem :

- The electromagnetic field propagation is described by partial differential equations (PDE). In complex media with complicated geometries, such as realistic head models built from structural MRI of the subjects, solving these PDEs requires to use numerical methods which are generally computationally expensive, both in memory and in time. It hence limits the use of complicated geometries that describe precisely the head geometry. Most experimenters in EEG and MEG still use spherical descriptions of the head, for which quasi-analytical solutions were developed.

- The electrical conductivities of the organic tissues of the head are not well known, nevertheless these properties affect the electromagnetic field propagation (especially the electric potential). For most head models, the conductivity values come from *in vitro* measurements, which does not account for the reality of tissues in their natural environment. For the head models to correspond as well as possible to reality, methods are developed for *in vivo* conductivity estimation.

In this thesis, we present contributions on these two issues of the forward problem. The manuscript is composed of an introduction and two parts. The introduction is meant to give the reader an overview of the research field linked to functional

brain imaging with EEG and MEG. We particularly emphasize the forward modeling problem, which ends this introduction. The first part presents our contributions on the numerical methods for the electromagnetic PDEs in complicated geometries. The second part focuses on the problem of the conductivities for EEG and MEG head models.

MANUSCRIPT OVERVIEW

Introduction

This part explains how the signal observed with EEG and MEG is generated, what are the methods for source localization and finally how is performed the forward problem modeling.

Chapter 1 introduces the physiology of the EEG and MEG signals. Section 1 explains the physiological mechanisms that are responsible for the neuronal electrical activity. We then present in section 2 how the electromagnetic field generated by brain electrical activity can be measured at the head surface. This chapter ends with section 3, illustrating the scale problem of the sources that are detectable with EEG and MEG, which are far greater than a single neuron.

Chapter 2 presents the characteristics of EEG and MEG when they are used as brain functional imaging modalities. Section 2 shows the types of measures that are recorded with EEG and MEG, and the inverse problem of source localization is introduced in section 3. The source localization depends on the hypotheses with regard to the distribution of brain activity, and as a consequence different source models can be used (section 4). Finally, we explain in section 5 some of the most common methods for source localization.

Chapter 3 presents in detail the different approaches for the forward problem modeling. We first start by recalling the classical equations of electromagnetism that apply to EEG and MEG (section 1). Then we explain how to solve these equations in more and more complex geometries : an infinite homogeneous medium (section 2), a conductor with a spherical geometry (section 3) and finally realistic head geometries (section 4). To compute the electromagnetic field in the case of EEG and MEG, it is sometimes useful to use the reciprocity concept, which basically states that source and sensors can be interchanged. This concept is explained in section 5. The last section presents the problem of the choice of conductivities in head models (section 6).

Part I - Forward problem computation

This first part deals with the computation of the forward models : we present a new Finite Element Method (FEM) which uses a simple cubic grid as a mesh while keeping a precise description of the interfaces between the head tissues (chapter 4), and a general framework for reciprocity in EEG and MEG (chapter 5).

Chapter 4 - Implicit meshes for Finite Element Methods

Using the FEM to solve the forward problem requires to mesh the head domain with respect to the different head tissues. The common technique is to build a tetrahedral

mesh. This mesh must at the same time be a good representation of the underlying geometry and respect some quality criteria (tetrahedra homogeneity). Automatic techniques for mesh generation sometimes create defects which require user interaction to ensure the final quality of the mesh. As a consequence, the process of mesh generation is sometimes laborious and time consuming. On the contrary, when using a Finite Difference Method (FDM) to solve the forward problem, the meshing step simply consists in defining a cubic grid, which moreover can be directly taken from the MRI cubic grid. The complicated meshing of the FEM is hence avoided. Yet the description of the geometry in FDM is not as good as the FEM, because the different tissues are described as staircase domains. We thus propose a method for the forward problem computation which combines both the simplicity of the cubic grid of the FDM and the precise description of the interfaces of the FEM. It is actually a FEM method, which uses a cubic grid (usually the MRI grid) with an element basis of trilinear functions. The precise description of the interfaces between tissues is then taken into account by using their levelset representations on the grid. For a better understanding of this chapter, appendix A gives the details of the classical tetrahedral FEM method. This chapter is based on an article presented at the *MMBIA* workshop of the conference *ICCV 2007* [80].

Chapter 5 - The adjoint method for general sensor-based lead field equations

Usually, to use EEG or MEG source localization methods, one has to solve the forward problem for many possible locations of the brain sources (between 10^3 and 10^5). When the forward problem is solved in complex geometries with numerical methods, this can be computationally too expensive. This problem is avoided by considering a reciprocal approach, where the sources and the sensors are interchanged. In this case, the forward problem has to be solved for the different possible locations of the sensors (between 50 and 300), which considerably reduces the computational cost. The reciprocal approach consists in considering a different electromagnetic field PDE. For instance, in EEG, the electric potential generated by a source $\mathbf{J}^{\mathrm{p}}$ in a domain Ω satisfies the PDE :

$$\begin{cases} \nabla \cdot (\sigma \nabla V) = \nabla \cdot \mathbf{J}^{\mathrm{p}} \text{ in } \Omega \\ \sigma \nabla V \cdot \mathbf{n} = 0 \text{ on } \partial\Omega \end{cases}$$

and the reciprocal PDE, corresponding to the electric potential generated by a current injection, is the following :

$$\begin{cases} \nabla \cdot (\sigma \nabla V) = 0 \text{ in } \Omega \\ \sigma \nabla V \cdot \mathbf{n} = \delta_{\mathbf{r}_1} - \delta_{\mathbf{r}_2} \text{ on } \partial\Omega \end{cases}$$

where $\mathbf{r}_1$ and $\mathbf{r}_2$ are the points where the current is injected. In this case, where the electric potential and pointlike measurements are considered, the reciprocal PDE that has to be solved is directly given by Helmholtz's reciprocity theorem. The reciprocal PDE for the magnetic field is not as straightforward to obtain : it has been formulated for pointlike measurements in [74]. In this chapter, we propose to use the adjoint method as a general framework to derive the reciprocal PDE, both in EEG and MEG. The advantage of this formulation is that the reciprocal PDE can also be extended to non-pointlike sensors, in aim to take into account the area of

the EEG electrodes or the geometry of the MEG sensors (magnetometers, gradiometers). This chapter is adapted from an article submitted to the journal *Physics in Medicine and Biology*.

Part II - Conductivity calibration

This second part deals with the problem of the choice of conductivity values in EEG forward models : we present a global sensitivity analysis of the three-layer head models (chapter 6), and a method for conductivity calibration with somatosensory evoked potentials (chapter 7).

A global sensitivity analysis of the three-layer conductivity models for EEG

The propagation of the electric potential is affected by the changes of electrical conductivity in the head. As a consequence, the choice of the conductivities in a head model has an effect on the topographies of the electric potential, which directly affects the source localization with EEG. To better understand what conductivities of the head model are important with respect to the EEG topography, it is necessary to perform a sensitivity analysis. When considering a linear model, it is sufficient to perform a local sensitivity analysis to fully understand the model. But the electric potential has a strong non-linear dependency on the conductivity of the head model, so a local sensitivity analysis is not sufficient in this case. We thus present in chapter 6 a global sensitivity analysis, which is able to capture all the variability of the EEG topographies with respect to the conductivities of the head model. This global sensitivity analysis is performed using a variance-based method, hence the appendix B gives an overview of this type of methods. This chapter is adapted from an article submitted to the journal *IEEE Transactions on Biomedical Engineering*.

Conductivity calibration with somatosensory evoked potentials

A common modality for conductivity estimation of the EEG forward models is Electrical Impedance Tomography (EIT). In this technique, a current is injected between two scalp electrodes, and the conductivities of the head model are inferred from the resulting scalp potential measurements. The sensitivity analysis presented in chapter 6 reveals that the EEG scalp topographies have a different sensitivity to the conductivities whether the source is in the brain or on the scalp surface. As a consequence, the conductivity model can be better calibrated when the source configuration is similar to the one considered for brain source localization. We thus propose in chapter 7 a method for conductivity calibration using somatosensory evoked potentials. This chapter is based on an article presented at the *ISBI 2007* conference.

LIST OF PUBLICATIONS

Journals

- Sylvain Vallaghé, Maureen Clerc, "A global sensitivity analysis of three and four-layer EEG conductivity models", *IEEE Transactions on Biomedical Engineering*, 2008, accepted for publication.
- Sylvain Vallaghé, Théodore Papadopoulo, Maureen Clerc, "The adjoint method for general EEG and MEG sensor-based lead field equations", *Physics in Medicine and Biology*, 2008, accepted for publication.

Conferences

- Sylvain Vallaghé, Maureen Clerc, "In vivo conductivity estimation using somatosensory evoked potentials and cortical constraint on the source", *IEEE Proceedings of ISBI 07*, Washington DC, USA, 2007.
- Théodore Papadopoulo, Sylvain Vallaghé, "Implicit meshing for finite element methods using levelsets", *Proceedings of MMBIA 07*, Rio de Janeiro, Brazil, 2007.
- Sylvain Vallaghé, Maureen Clerc, "Conductivity estimation for EEG: what is relevant ?", *IEEE Proceedings of NFSI & ICFBI 07*, Hangzhou, China, 2007.

Introduction

CHAPTER 1

PHYSIOLOGY OF EEG AND MEG

Contents

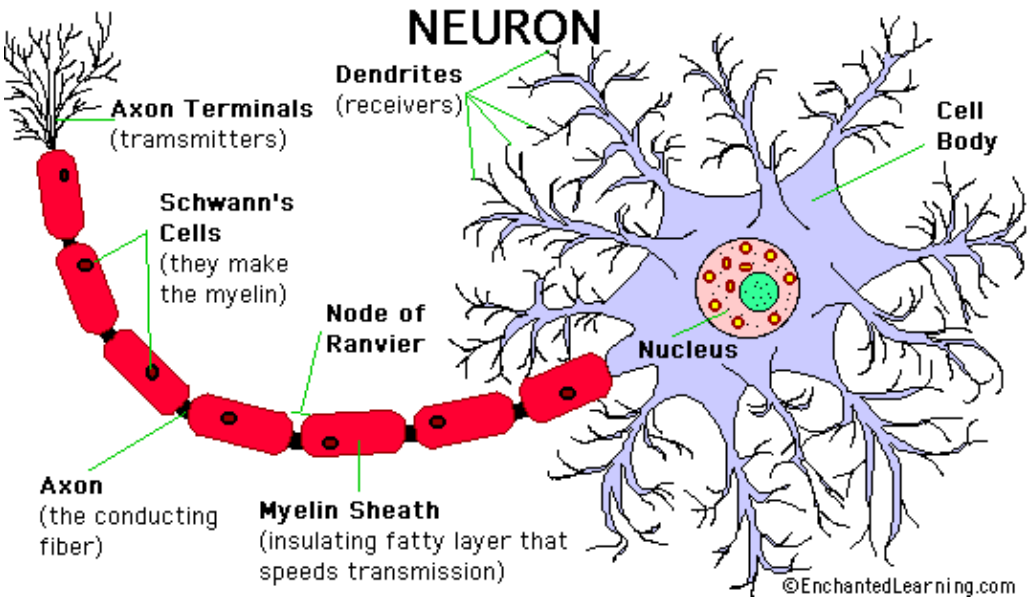

Figure 1.1: Neuron diagram. Source : enchantedlearning.com.

1 NEURAL ORIGIN OF THE BRAIN ELECTROMAGNETIC FIELDS

The human brain is a very complex structure composed of around 100 billions of small elementary units : the neurons. The neurons are linked together and each neuron can have up to 10000 connections. The neuron is a cell with a special shape : it is composed of a soma or cell body, containing the nucleus, a dendritic tree and an axon, as shown in figure 1.1. It can be viewed as a signal receiver, processor and transmitter : the signal coming from the dendrites is processed at the soma and generates (or not) an action potential which is carried along the axon towards other neurons. The signal moving along the dendrites, called post-synaptic potential, is different from the signal moving along the axon, the action potential. We briefly describe the ion mechanisms [54] responsible for these two types of potential :

- **Post-synaptic potential**
  The junction between the axon terminal of a neuron and a dendrite or the soma of another neuron is called a synapse. It can be a direct electrical junction, but most of the time synapses are chemical : when an action potential reaches the end of an axon terminal, it releases neuro-transmitters. When a neuro-transmitter molecule touches the other neuron, the membrane permeability is affected and specific ions (Na+ and K+) penetrate inside, increasing the resting state potential of about 10mV with a duration of 10ms. This is called a post-synaptic potential. It is shown in figure 1.2a.

- **Action potential**
  When many post-synaptic potentials are summing up, the membrane potential of the soma can reach locally a certain threshold which makes the neuron "spike" : some voltage-sensitive channels open, allowing positive ions to flow

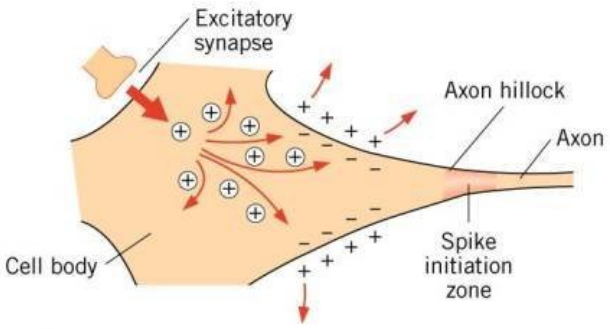

(a) Post-synaptic potential. Source : psy.jhu.edu.

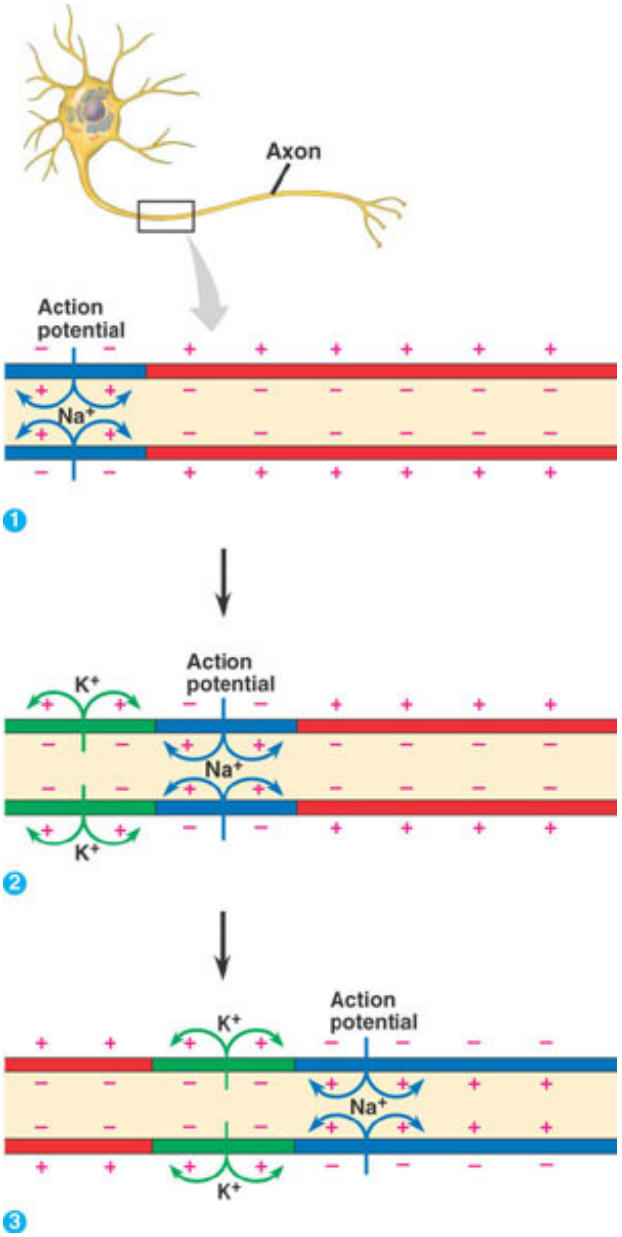

(b) Action potential propagation. Source : kvhs.nbed.nb.ca.

Figure 1.2: Neuron signals.

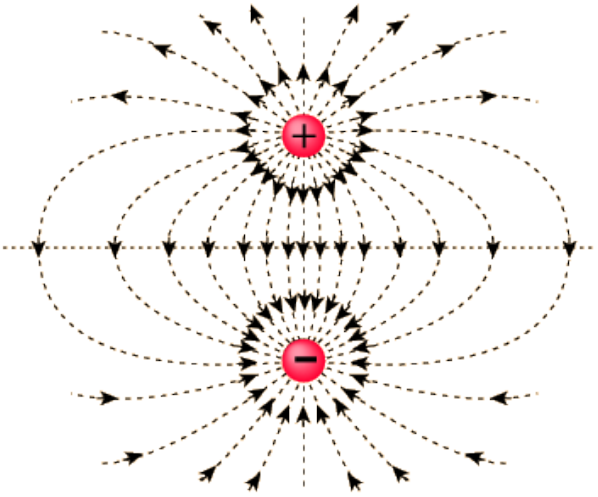

Figure 1.3: The electric field generated by an electric dipole (source hyperphysics.phy-astr.gsu.edu).

inside the cell, and the potential inside the neuron is increased suddenly. The potential comes back rapidly to its resting state (in 1ms), with the help of other voltage-sensitive channels that allow a compensating outward current. Because of this peak of potential, the nearby regions reach the threshold and spike too : the action potential thus propagates along the axon. It is shown in figure 1.2b.

These two types of potentials create some very small currents in the neuron which can be approximated by mathematical dipoles. In electrostatics, an electric dipole is the configuration obtained when two charges, one negative and one positive, are coming close to each other along a certain axis. A dipole is defined by its position (where the charges are located), and its moment, a vector pointing from the negative to the positive charge and whose amplitude is given by the magnitude of the charges times the distance between them. An electric dipole creates an electromagnetic field : the figure 1.3 shows the shape of the electric field lines.

We can extend this concept of electric dipole to a current dipole. The most simple current configuration is to consider a simple wire between two points which are respectively a source and a sink of current. Physiologically, if we consider a neuron, when a dendrite receives an increase of positive ions due to an excitatory synapse, there is a current source at the dendrite and a sink of current at the soma, and the current flows in the wire represented by the dendrite. When the source and the sink of current are coming close to each other, we have a current dipole configuration. Like the electric dipole, it is defined by a position (where the source and sink are located), and a moment, a vector pointing from the source to the sink and whose amplitude is given by the magnitude of the current times the distance between the source and the sink. The electromagnetic field generated by a current dipole has exactly the same shape than the electromagnetic field of an electric dipole. As shown by figure 1.4, the current generated by a post-synaptic potential corresponds to a single current dipole aligned with the dendrite, whereas the action potential can be represented as two opposite current dipoles aligned with the axon. For the action

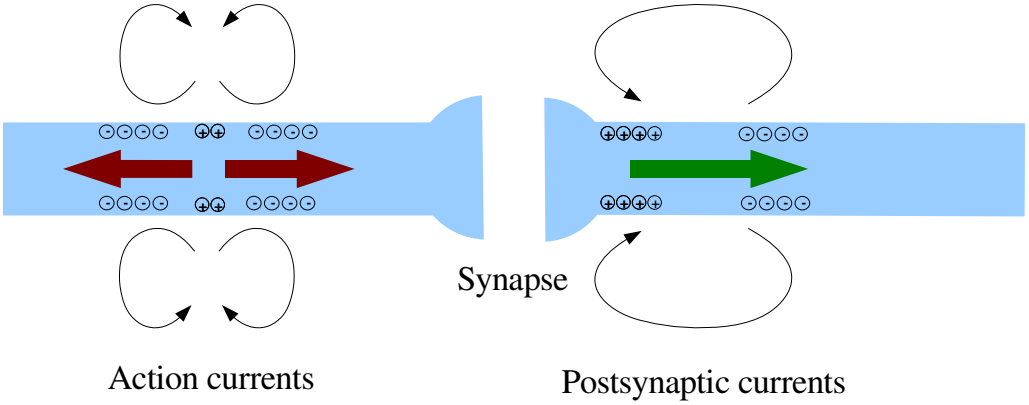

Figure 1.4: External currents generated by action and post-synaptic potential. There is a clear difference between the dipolar and quadrupolar structures.

potential, the two opposite dipoles correspond to a quadrupole. In a simple infinite homogeneous medium, the electric potential at a position $\mathbf{r}$ generated by a dipole at the origin is :

$$V(\mathbf{r}) = K\frac{\mathbf{q}\cdot\mathbf{u}}{r^2} \quad ,$$

where K is a constant, $\mathbf{q}$ is the dipole moment, $\mathbf{u}$ is the unit vector in the direction of $\mathbf{r}$ and r is the norm of $\mathbf{r}$ (distance between the dipole and the observation point). The electric potential thus decreases as the inverse of the square of the distance. For a quadrupole, the electric potential is :

$$V(\mathbf{r}) = K\frac{1}{r^3}\sum_{i,j} q_{ij}u_i u_j \quad ,$$

where q_{ij} are the quadrupole moments and u_i are the components of the vector $\mathbf{u}$. In this case, the potential decreases as the inverse of the cube of the distance. The same difference of decrease rate also holds for the magnetic field. It means that if a dipole and a quadrupole located at the same positions are observed from a long distance, the electromagnetic field of the quadrupole is negligible compared to the field of the dipole. As a consequence, when the brain electromagnetic field is measured outside the head (”far” from the neurons), it is commonly accepted that the electromagnetic field generated by the action potential is negligible with respect to the one generated by post-synaptic potentials.

Still, the post-synaptic potentials of one neuron alone cannot generate an electromagnetic field sufficient to be measured outside the head. To give an idea, it is necessary to sum the field amplitudes of about 10^4 neurons to produce a field amplitude that is detectable outside the head [72]. Furthermore, the amplitude of the fields generated by many dendrites completely sum only if the dendrites have the same direction and orientation. For instance, stellate cells which have dendrites in all directions can not produce a measurable field. Only the class of neurons called pyramid cells have the regular organization that is required to sum the fields generated by their post synaptic potentials. The pyramidal neurons are located mostly in the gray matter of the cortex (see section 3.1), and they all have a thick dendrite (called apical dendrite) extending towards the exterior of the cortex, perpendicularly to its surface, as shown by figure 1.5 and 1.6. These neurons constitute about 70% of

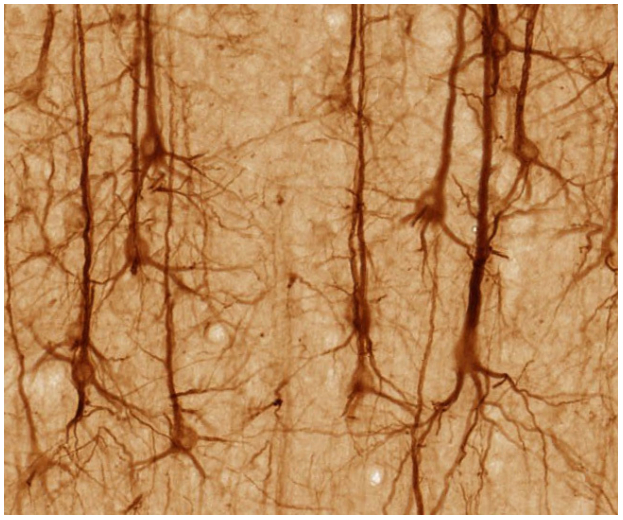

Figure 1.5: Pyramidal neurons in medial prefrontal cortex of macaque. Source brainmaps.org.

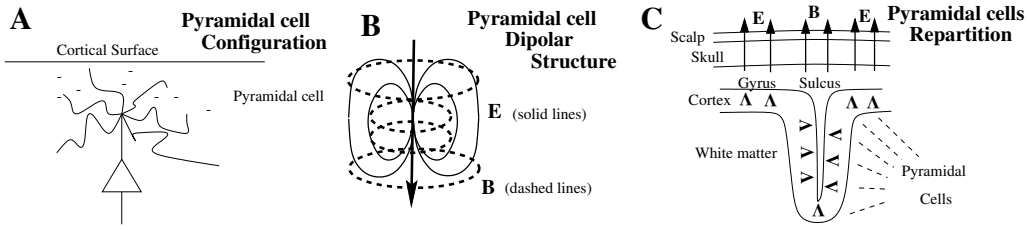

Figure 1.6: Pyramidal cells in the cortex and the corresponding electromagnetic field (**E** is the electric field, **B** is the magnetic field).

the neo-cortex, and their density is such that theoretically the simultaneous activation of an area of $1mm^2$ of the cortex would be detectable, even if experimental studies showed that the minimal detectable activity has an area of about $100mm^2$ [41].

2 NON-INVASIVE MEASURES OF THE BRAIN ELECTRIC ACTIVITY

Because the electric activity of the neurons produces an electromagnetic field, it is possible to detect at a distance the brain activity when the corresponding electromagnetic field is sufficiently strong. This offers the possibility to get information about the brain activity from outside the head, in a non-invasive way. An electromagnetic field is composed of two parts, the electric field and the magnetic field, which can both be measured in different ways. As a consequence, two modalities have been developed for measuring the brain electromagnetic field outside the head : one measures the electric potential and is called electroencephalography, the other measures the magnetic field and is called magnetoencephalography.

Figure 1.7: An EEG equipment : the electrode helmet is placed on the head of the subject, then the signal is processed through an amplifier and digitalized on a computer (Odyssée project team, INRIA Sophia Antipolis).

Figure 1.8: A MEG equipment : the helmet equipped with SQUID sensors is immersed in helium (Magnetoencephalography center, La Timone, Marseille).

2.1 Electroencephalography (EEG)

This modality is the oldest one. Human EEG recordings started in 1920 with the German physiologist and psychiatrist Hans Berger. The recording is obtained by placing electrodes which measure the electric potential on the scalp of the subject. Nowadays, these electrodes are connected to an amplifier and the signal is then digitalized and stored on a computer. The advantage of this device is its simplicity and cheap cost. Unfortunately, the low conductivity of the skull tends to diffuse the electric potential, and at the surface of the scalp, the potential only reflects coarsely the underlying brain activity. The number of electrodes on a modern EEG helmet is usually 32, 64 or 128.

2.2 Magnetoencephalography (MEG)

The magnetic field generated by the human brain was first measured by David Cohen in 1968, using only a copper induction coil as the detector. The main problem is

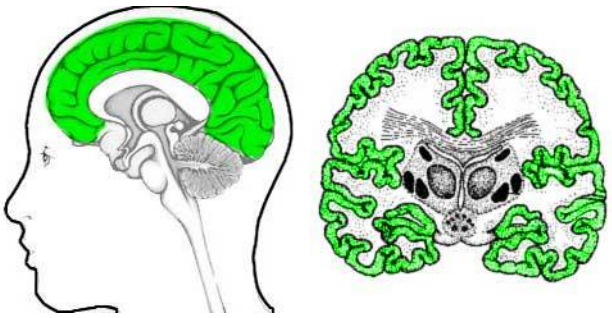

Figure 1.9: The cerebrum is shown in green on the left. The gray matter of the cerebral cortex is shown on the right.

the weakness of the signal generated by the brain activity, a magnetic field with an intensity of a few femtoteslas ($1fT = 10^{-15}T$). In comparison, the Earth's magnetic field has an intensity of about $10^{-5}T$. David Cohen made the measurements in a magnetically shielded room to reduce the magnetic background noise, but it was not sufficient to get a clear signal. In 1969, Zimmerman and colleagues finished the development of the SQUID (superconducting quantum interference device), a detector using supra-conductors which can measure very small variations of the magnetic field. A few years later, Cohen measured again the brain magnetic field using a single SQUID detector and a better magnetic shielded room. This time the signals were comparable to EEG. Nowadays, the MEG systems contain between 150 and 300 SQUID sensors, covering most of the head. A MEG system is very expensive compared to EEG, because the SQUID sensors need to operate at very low temperature, and for this reason are immersed in liquid helium. Moreover, most often a magnetic shielded room has to be built to use the system. Nevertheless, the magnetic field is much less sensitive to the low conductivity of the skull than the electric potential, and the magnetic field observed outside the head is a sharper representation of the underlying brain activity. That is why in spite of their cost, more and more MEG systems are being built.

3 EEG AND MEG : WHAT ARE WE LOOKING AT ?

Anatomically speaking, the brain of vertebrates is composed of many different structures, which can be classified with respect to the different stages of the development of the central nervous system. There are five major divisions, starting with the spinal chord and ending with the cerebrum. In humans, the cerebrum, which contains the cerebral cortex, is very developed and thus completely surrounds all the other (and "older") parts of the brain (figure 1.9a). The outermost layer of the cerebrum, called the gray matter, is formed by neurons, and the white matter below the gray matter is formed by axons. As a consequence, the neurons of the gray matter are the closest of the head surface, and other neurons of the brain have their cell body in the center, far from the head surface, due to the space taken by the white matter (figure 1.9b). Because of the decrease rate of the electromagnetic field, it is assumed that the signal measured with EEG and MEG comes mainly from the neu-

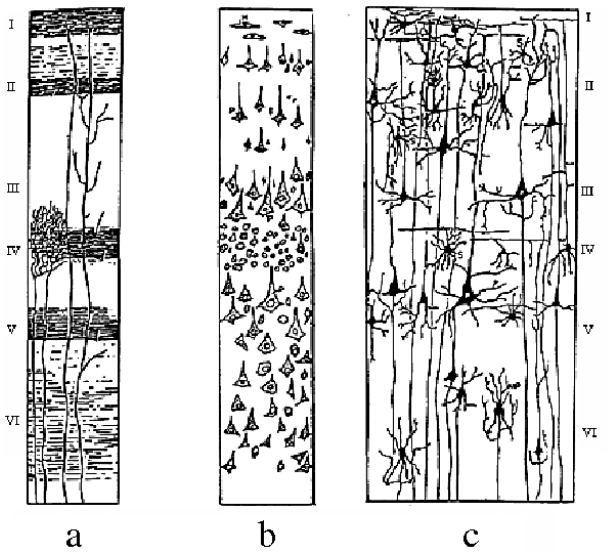

Figure 1.10: Cortical layers. Layer organization of the cortex (a) Weigert's coloration shows myelinated fibers (axons) and so the connections inside and between layers, (b) Nissl's coloration only reveals cell bodies (c) Golgi's coloration shows the whole cells (From [75]).

rons of the gray matter, especially the part of the gray matter located closely under the skull, which is part of the cortex. The cortex is involved in higher functions of the brain such as sensory perception, motor commands, consciousness, language, and so EEG and MEG can be used to measure the brain activity during cognitive tasks.

3.1 Basic organization of the cortex

The cortex is mainly composed of gray matter formed by neurons and their unmyelinated fibers. The white matter below the gray matter of the cortex is formed predominantly by myelinated axons interconnecting different regions of the central nervous system. First of all, it has been proved that the gray matter has a horizontal organization in layers composed of different cell types (see figure 1.10). The number of layers, their cell composition, their thickness and organization are not the same over the whole surface of the cortex. These differences led neuroanatomists to divide the cortex into small regions called areas (figure 1.11) whose characteristics were homogeneous and that corresponded to different functions, e.g., vision or motion. Generally speaking, most of the cortex is made up of six layers of neurons, from layer I at the surface of the cortex to layer VI, deeper, that lies close to the white matter. For humans, its thickness varies from 3 to 6 mm.
More detailed information about cortical structure and function can be found in [51, 82, 52]. The organization of the cortex is not only laminar. It has been observed that neurons located in a column perpendicular to the cortex tend to be connected to each other and to respond to precise stimulations with similar activities throughout the layers. They form a cortical column. Several studies have shown biological evidence for such small aggregates of about one hundred neurons, 20 up to 50 μm wide, called minicolumns (see e.g. [10, 71]). Larger columnar structures have been also

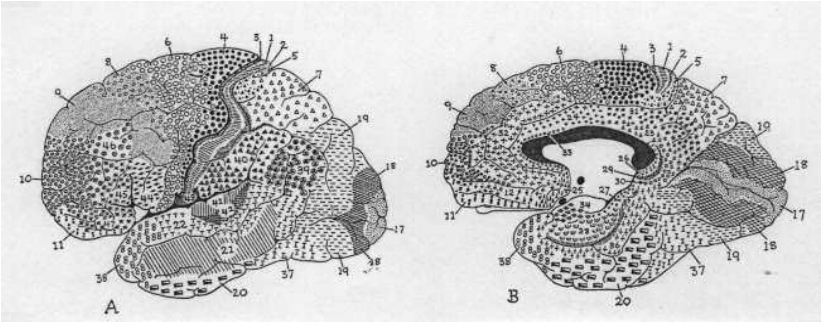

Figure 1.11: Cortical areas. In 1909, Brodmann [9] divided the cortex into 52 cytoarchitectonic areas according to the thickness of the cortical layers. For example, layer IV is very thin in the primary motor cortex (area 4) while it is very thick in the primary visual cortex (area 17).

observed. For instance, Mountcastle in [70] showed that neurons inside columns of 300 to 500 μm of diameter displayed similar activities. Those physiological units are usually called macrocolumns.

3.2 Models of brain electric activity for EEG and MEG

As we explained in section 1, the post-synaptic electrical activity of a neuron can be modeled by a current dipole. Nevertheless, this dipole has a very weak intensity and its electromagnetic field can not be measured with EEG or MEG. Only the summation of the activity of more than 10^4 neurons with the same dipolar structure can generate a detectable signal. Such a structure, where many neurons have dendrites all parallel to each other, can be found in the pyramidal neurons of the gray matter. The density of the pyramidal cells in the cortex is such that the simultaneous activation of about $100mm^2$ of the cortex is sufficient to produce such a signal.

The consequence for EEG and MEG is that the brain activity is observed at a macroscopic scale with respect to the size of a neuron. What is measured is the electrical activity of assemblies of neurons. The typical size of the neuron assemblies observable with EEG or MEG is bigger than the size of cortical columns but smaller than the size of a cortical area. For the last three decades, neuroscientists have been building models of neuron assemblies [63, 116, 28, 50, 107, 98], based on the knowledge of neuronal dynamics, but the dynamics of such assemblies is far from being completely understood.

It leads to the problem of the modeling of the brain electric activity for EEG and MEG. The main assumption is that the measurements reflect the activity of one or several assemblies of neurons. For one assembly, the EEG or MEG measurements only reflect its average activity, and it is usually considered that the intrinsic dynamics of the group of neurons is unknown. As a consequence, for EEG and MEG, the most common model of the brain activity is to use a finite set of simple electric sources (such as dipoles). Each source is meant to reflect the average activity of the assembly of neurons surrounding it. As explained in chapter 3, section 2.1, because the area of a neuron assembly is small compared to the distance to the observation point (the EEG-MEG sensors), a dipole located at the center of the area can generate a very similar electromagnetic field as when the whole area is activated (figure 1.12).

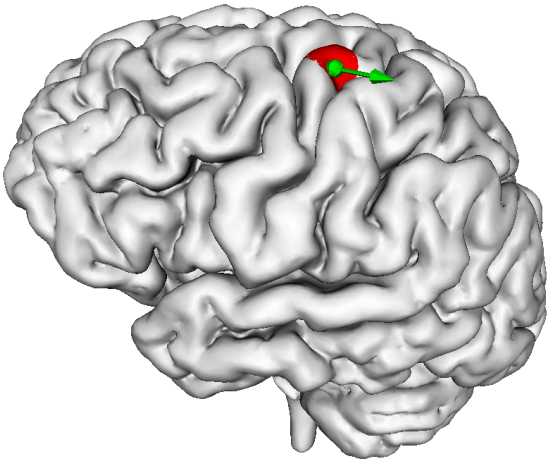

Figure 1.12: The activity of a small region of the brain can be approximated by a current dipole. The position of the dipole (the dot) is at the center of the activated cortex area and the moment of the dipole (the arrow) corresponds to the average orientation of the pyramidal neurons in this region (perpendicular to the cortical surface).

CHAPTER 2

BRAIN FUNCTIONAL IMAGING WITH EEG AND MEG

Visualizing the brain in function means localizing in space and time the activity of the brain. Because the activity of the brain is mainly electrical, and because this electrical activity produces an electromagnetic field outside the head, EEG and MEG measurements give an information on this activity, and can then be used for brain functional imaging.

Contents

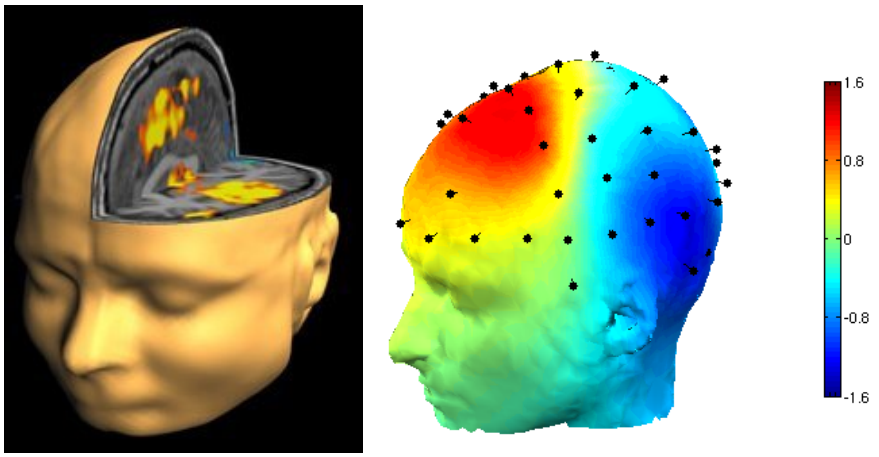

(a) fMRI (b) EEG

Figure 2.1: On the left, the statistically significant brain activity is evaluated using fMRI (source hitl.washington.edu). On the right, an image of the electric potential at the head surface is given by the average of EEG measurements (evoked potential).

1 INTRODUCTION

Medical imaging underwent a revolution when the x-ray computed tomography (CT) was introduced about 30 years ago. It was then possible to look almost non-invasively at a three-dimensional image of the anatomy of organs within the living human. After CT, other imaging techniques appeared, like positron emission tomography (PET) and magnetic resonance imaging (MRI). With the development of PET and MRI came the opportunity to not only look at the anatomy but also to evaluate the function of organs. With these new imaging techniques, researchers interested in the function of the human brain were presented with an opportunity to examine how brain function correlates with mental activities. It contributed significantly to the understanding of the human brain, and developed the field of cognitive neuroscience.

Nevertheless, PET and fMRI (functional MRI) are limited by the temporal resolution they offer (of the order of the second) and also by the quantity they measure (glucose or oxygen uptake) which is indirectly related to brain activity. As a consequence, one brain image produced with PET or fMRI reflects the average brain activity over a period of time of about one second or more. Many temporal dynamics of the brain are not captured by these imaging modalities, because the typical frequencies of the brain activity are way above 1 Hz.

On the contrary, because the electromagnetic field propagates at the speed of light, the EEG and MEG measurements give instantaneous information about the electrical activity of the neurons. Moreover, EEG and MEG can be recorded at a frequency of $1kHz$ or more, which is superior to the frequencies of the brain activity. These measurements hence allow to follow in details the temporal dynamics of the brain, in a non-invasive way. The difference with PET and fMRI is that EEG and MEG do not give a 3d image of the brain but only an image of the electromagnetic field at the surface of the head (figure 2.1).

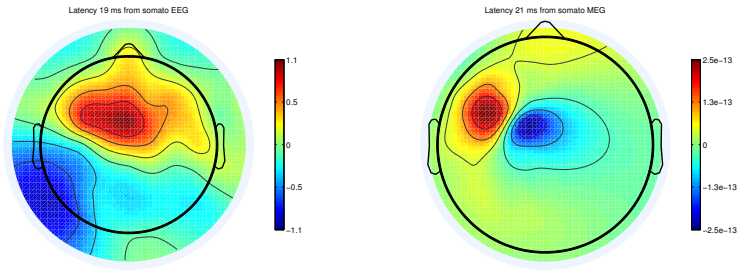

(a) EEG (b) MEG

Figure 2.2: The subject is presented with an electrical stimulation of the median nerve located at the right wrist. This stimulus is repeated about a thousand times and the EEG or MEG measurements are then averaged to extract the activity which is correlated and locked in latency with the stimulus. This is called evoked activity. On this figure the evoked potential/magnetic field is shown 20 ms after the stimulus onset (top view of the sensors on/above the subject's head).

2 EEG-MEG AS FUNCTIONAL BRAIN IMAGING MODALITIES

The study of the brain dynamics first started with EEG, and for many years researchers and clinicians only used the surface EEG recordings. From the topography of the electric potential at the electrodes, and their knowledge about brain anatomy and functions, they could infer the location of the brain activity at a very coarse spatial resolution. Figure 2.2 shows typical EEG and MEG topographies that are generated by a simple stimulation of the right wrist of a subject. If we compare it with the electric potential and magnetic field generated by a simple dipole (figure 2.3a), one can tell that the source of the brain electrical activity is very likely located in the left hemisphere, at the center with respect to the front and the back of the brain. This is in agreement with the knowledge that the left hemisphere mainly processes the information concerning the right part of the human body, and that the sensory information is processed in the so-called somatosensory cortex, located posterior to the central sulcus of the cortex (figure 2.3b). It is important to note the difference between EEG and MEG topographies : for the same brain source, the topography at the head surface is more focal in MEG than in EEG. It means that the MEG has a better capacity to distinguish between two activities with close locations in the brain. This is due to the fact that the magnetic field is not very sensitive to the electrical conductivities of the head tissues, and thus propagates almost like in an homogeneous conductor. On the contrary, the electric potential is sensitive to the conductivity, and is affected by the low conductivity of the skull which tends to diffuse the electric potential at the surface of the head.

The topographies of EEG and MEG measurements can give an information on the location of the brain activity, but the ultimate goal of the brain functional imaging is to generate a 3d image of the brain activity. That is why research is carried out in the EEG-MEG field to find methods for localizing the electrical activity responsible for the electromagnetic field observed at the surface of the head. These

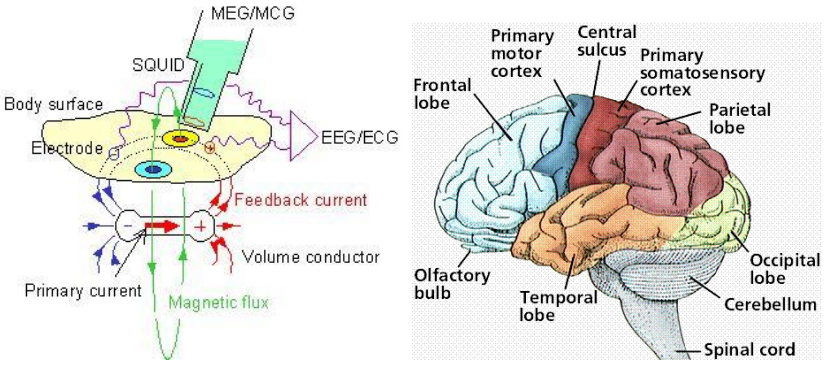

(a) Dipole field (b) Somatosensory cortex

Figure 2.3: On the left, the figure shows the lines of the electromagnetic field generated by a single dipole (Source biomagnetism.kriss.re.kr). The dipole field has a very characteristic shape : at the surface, the EEG and MEG measurements show two peaks, one positive and one negative, located on both sides of the dipole location. With EEG, these two peaks are aligned with the dipole moment, whereas for MEG the two peaks are aligned perpendicularly to the dipole moment. On the right, the location of the somatosensory cortex is shown among other main parts of the brain (Source emc.maricopa.edu).

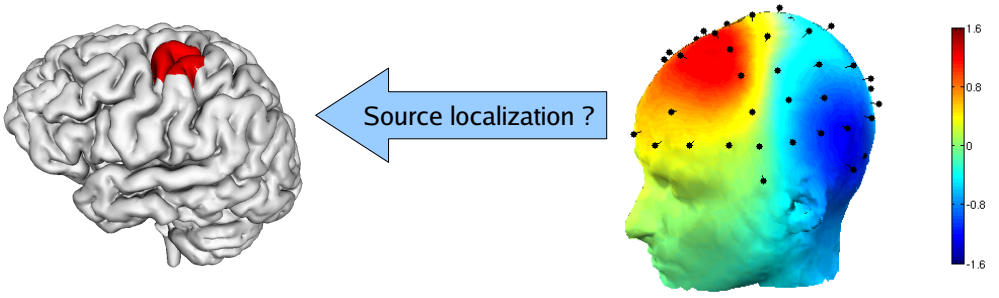

Figure 2.4: An illustration of the source localization problem : inferring the distribution $\mathbf{J}^{\mathrm{p}}$ of active electrical sources (left) from sensor data (right).

methods try to estimate a solution to the *source localization problem*, which can be stated as : how to pass from the surface measurements to the underlying brain activity (figure 2.4) ?

3 THE SOURCE LOCALIZATION PROBLEM

We assume that we have a model which describes the propagation of the electromagnetic field in the head. It means that for any distribution of electrical sources in the brain, which can be represented as a vector field of $\mathbb{R}^3$ denoted $\mathbf{J}^{\mathrm{p}}(\mathbf{r})$ (this notation is explained in chapter 3), we are able to compute the corresponding electromagnetic field in the whole head domain. For instance, for the electric potential $V(\mathbf{r})$, we have a model f such that $V = f(\mathbf{J}^{\mathrm{p}})$. How to build and compute such a

model is referred to as the forward problem and is explained in chapter 3.

Now suppose we have some measurements $v_1, \ldots, v_n$ of the electric potential at some electrode positions $\mathbf{r}_1, \ldots, \mathbf{r}_n$. To localize the brain activity, we would like to find the distribution $\mathbf{J}^\mathrm{p}$ that best explain the measurements. If we have a model $V = f(\mathbf{J}^\mathrm{p})$, we want to find $\mathbf{J}^\mathrm{p}$ such that the difference between the model simulation V and the real potential is as small as possible. Because the real potential is measured only at the electrodes placed at the surface of the head, we can only compare the real potential and the model simulation at the electrode positions, i.e. compare $V(\mathbf{r}_i)$ and v_i. For example, we can look for $\mathbf{J}^\mathrm{p}$ that minimizes the quantity

$$\sum_{i=1}^{n} (V(\mathbf{r}_i) - v_i)^2 \quad \text{with} \quad V = f(\mathbf{J}^\mathrm{p}) \ .$$

The source localization problem is the problem of finding such a $\mathbf{J}^\mathrm{p}$. The problem is exactly the same with MEG but with a model for the magnetic field $B = g(\mathbf{J}^\mathrm{p})$ and magnetic measurements $b_1, \ldots, b_n$.

The source localization problem falls in the category of inverse problems. An inverse problem occurs when the values of some model parameters must be obtained from the observed data. In our case, we have a model $V = f(\mathbf{J}^\mathrm{p})$, some observed data $v_1, \ldots, v_n$ (the measurements), and we want to obtain the values of the model parameter $\mathbf{J}^\mathrm{p}$. Inverse problems are typically ill posed, as opposed to the well-posed problems more typical when modeling physical situations where the model parameters or material properties are known (which is the case for the forward problem). The three conditions for a well-posed problem were suggested by Jacques Hadamard : a solution exists, the solution is unique and the solution depends continuously on the data. In particular, the source localization problem in EEG or MEG does not satisfy the uniqueness condition. It is well known in electromagnetism since Helmholtz that in certain conductors, there are some configurations of electrical sources that produce no electromagnetic field outside the conductor. Such sources are called silent sources. Adding a silent source to a solution of the source localization problem would not change the electromagnetic field outside the head, and so the solution is not unique. Because of this, in the inverse problem, one needs to make explicit any available a priori information on the model parameters. In the source localization problem, the model parameters are the values of the vector field $\mathbf{J}^\mathrm{p}$, representing the sources of electrical activity in the brain. The a priori information on the brain sources can be made explicit by using constraining models for $\mathbf{J}^\mathrm{p}$.

4 SOURCE MODELS

4.1 Dipolar models

A possible assumption about the brain activity is that it is sparse and focal. In other words, at a given time, the activity occurs at a small number of places in the cortex, and at each place the area of the cortex which is active is small (compared to the distance to the sensors). In this case, as explained in chapter 1, section 3.2

and chapter 3, section 2.1, the activity of each area can be represented by one single dipole, called equivalent current dipole (ECD). The goal of the source localization problem is then to find the parameters of the dipoles (six for each dipole, position and moment). Different approaches can be used to estimate these parameters. The most common simply consists in minimizing the residual error between the model and the measurements, this is called the least-squares dipole fit. The details of this method are explained in section 5.2. Other methods are based only on analytical considerations, but are restricted to a spherical description of the head [4, 11, 5]. In general, for the solution to be unique, the number of parameters to be estimated should not be greater than the size of the data [2] (given by the number of sensors, typically 64 for EEG and 150 to 300 for MEG).

Most of the time, the brain activity has a complex structure, for which the dipolar models are not very well suited, but they can still give good results when considering the evoked activity at short latencies. It has been shown that for sensory or motor experiments, the solutions obtained with dipolar models are correct with respect to the anatomic and functional knowledge of the brain [95]. The precision of the source localization with dipolar models has been evaluated to be a few millimeters with MEG [99] and about one centimeter with EEG [114, 58].

The simplest approach with dipolar models is to find the dipole parameters at a given time instant [92, 53, 108], which is usually at a peak observed in the evoked activity. If the dipole parameters are evaluated at several successive time instants, then the dipoles are moving with respect to time, this is the *moving dipole* approach. But considering the sample rate of EEG and MEG (more than 1 kHz), and the duration of post-synaptic potentials (10 ms), it is expected that the brain activity does not change too much between two time samples. The dipole localization can thus be performed on a small time window [89], so that there is more data available for the same number of parameters to be estimated. If only the position parameters are evaluated on the whole time window, but the moment is evaluated at each time sample, then the dipole can rotate over time, this is the *rotating dipole* approach. With a fixed position over time, the amplitude courses of the dipoles reflect the activity of the corresponding areas.

One drawback of the dipolar approaches is that the number of sources has to be chosen a priori. Most of the time it is chosen with respect to the knowledge of the experiment which is considered, but it can also be determined more or less automatically using the residual error between the model and the data, or by analyzing the spectrum of the data. Another limitation of the dipolar models is that it is not well suited to explain a complex activity in the brain, which occurs for late responses to a stimulus, or when the experiment is more complex than just a sensory or motor task.

An example of source localization with a dipolar model is given by figure 2.5.

4.2 Scanning approaches

This approach is closely related to the dipolar approaches, as it also estimates the positions of several dipoles that best explain the measurements. But the way to achieve such a result is quite different. In the scanning methods, the space of the head domain is sampled at many locations, usually following a regular grid, and at each location the probability of a dipole being present is evaluated. Then the dipole positions are given by the local maxima of an evaluating function over the

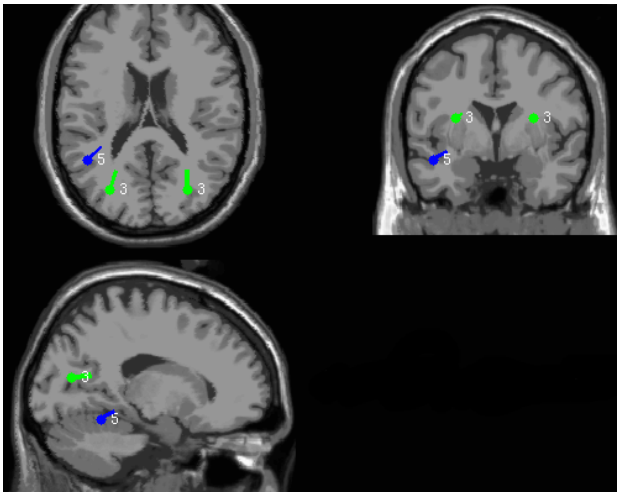

Figure 2.5: Three dipoles are localized using the dipole fit method. They are shown on different cross sections of the MRI of the subject. The dot gives the position and the bar gives the moment of each dipole. Source : eeglab.

head domain. The most common scanning method in EEG and MEG is the MUSIC method [69], which is explained in section 5.3. Another class of scanning methods fall in the category of the spatial filters, also called beamformers. For each sample point of the head domain, a spatial filter that can be applied to the data is computed, such that it theoretically extracts only the contribution of a dipole located at this given point [103]. When these filters are applied to the real data, they give at each point the estimated contribution of a dipole to the measurements. In this case, the dipole positions are again obtained for the local maxima among the contributions of all points. These approaches are usually more robust than the classical dipolar methods, but they can fail to reconstruct two different source positions when the temporal activities of these two sources are highly correlated. An example of source localization with the MUSIC method is given by figure 2.6.

4.3 Distributed source models

These methods were developed to bypass the limitations inherent to the dipolar approaches. The idea is to reconstruct an approximation of the whole source distribution, represented by the vector field $\mathbf{J}^p$. The most common approximation is to sample the totality or a part of the head domain, and to evaluate the values of $\mathbf{J}^p$ at each space sample. In other words, a dipole is positioned at each sample point, and the moments of all these dipoles are estimated at the same time. When using distributed source models, the number of parameters to estimate is far greater than the size of the data, due to the space sampling size (with just a simple grid $10 \times 10 \times 10$, there are 1000 dipole moments to estimate, i.e. 3000 parameters, and the number of sensors is at most 300). This is a situation often encountered in inverse problems, and in these cases, regularization techniques may be used to introduce assumptions on the solution and thus ensure its uniqueness. Different methods have been developed for distributed source models, depending on how the space is sampled (defining the source space) and what regularization is used. The general approach is explained in section 5.4.

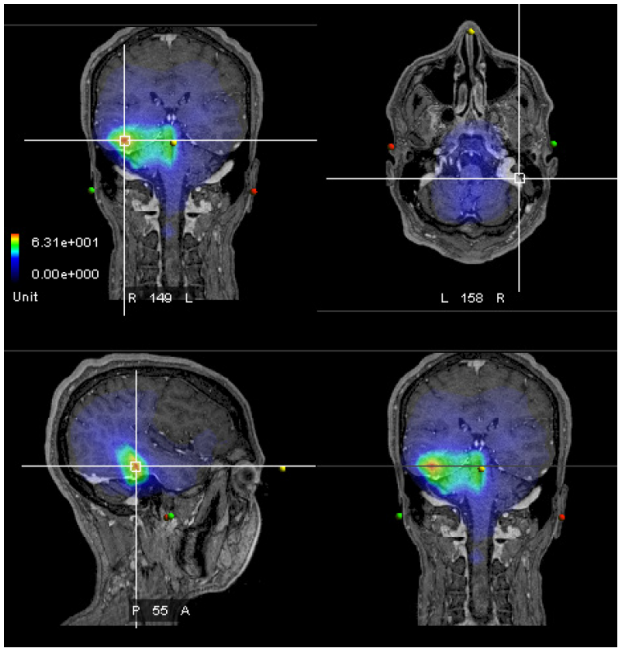

Figure 2.6: The MUSIC method computes in the brain space a map of the probability of a dipole being present. The peaks of the map gives the most probable locations of the brain activity.

Several regularizations for the distributed source models in EEG and MEG have been introduced [15, 42, 81], with general sampling of the head space. But it is possible to restrict the source space based on the a priori information that the brain activity is located in the gray matter of the cortex. This is done by segmenting an anatomical MRI of the subject to get a description of the cortical surface, and then distributing dipoles only on this surface and not in the whole head space [20]. The solution can be even more constrained by assuming that the moments of the dipoles are perpendicular to the cortical surface, which is coherent with the orientation of pyramidal neurons.

The main limitation of the distributed source approaches is that the regularization techniques that are used most of the time impose constraints on the solution which are defined mathematically (minimum norm of the solution, its gradient or its Laplacian), but which produce estimates of the solution that are not realistic physiologically (often the solutions are too smooth). One way to circumvent these problems is to incorporate information about the cortical structure and function in the regularization [3].

The figure 2.7 shows an example of solution obtained with a distributed source model.

5 METHODS

We now briefly describe some of the methods that fall in the different categories presented in the previous section.

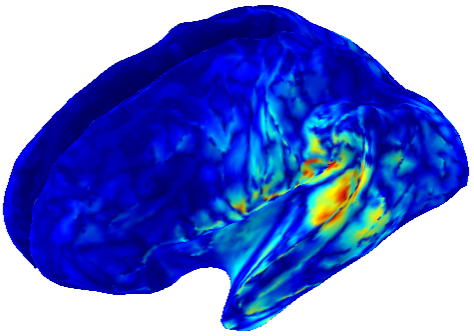

Figure 2.7: The distributed sources methods generally generate an image of the amplitude of the dipoles on the cortex. Here the cortex is unfolded to ease the visualization in the sulci. The red corresponds to a high amplitude and the blue to a zero amplitude.

5.1 Definitions

In this section, we introduce some concepts that are shared by most source localization methods. It is known that the electric potential V and the magnetic field $\mathbf{B}$ are linear with respect to the sources, represented by the vector field $\mathbf{J}^{\mathrm{p}}$. As a consequence, any EEG-MEG measurement $m(\mathbf{r})$ at a point $\mathbf{r}$ is a linear functional of $\mathbf{J}^{\mathrm{p}}$, and from the Riesz representation theorem, there exists $\mathbf{L}(\mathbf{r}, \mathbf{r}') : \mathbb{R}^3 \times \mathbb{R}^3 \to \mathbb{R}^3$ such that :

$$m(\mathbf{r}) = \int_{\Omega} \mathbf{L}(\mathbf{r}, \mathbf{r}') \cdot \mathbf{J}^{\mathrm{p}}(\mathbf{r}') dr' \ .$$

The vector field $\mathbf{r}' \to \mathbf{L}(\mathbf{r}, \mathbf{r}')$ is called the *lead field* of the measurement at the point $\mathbf{r}$. If we consider a dipole with position $\mathbf{r}_0$ and moment $\mathbf{q}$, such that $\mathbf{J}^{\mathrm{p}}(\mathbf{r}') = \delta(\mathbf{r}' - \mathbf{r}_0)\mathbf{q}$, where δ is the Dirac distribution, then we simply have :

$$m(\mathbf{r}) = \mathbf{L}(\mathbf{r}, \mathbf{r}_0) \cdot \mathbf{q} \ .$$

In this case, the vector field $\mathbf{r} \to \mathbf{L}(\mathbf{r}, \mathbf{r}_0)$ is called the *forward field* of the dipole at the position $\mathbf{r}_0$. Let us assume that $m(\mathbf{r}) = V(\mathbf{r})$ is a measurement of the potential, one can see that computing $V(\mathbf{r}) = \mathbf{L}(\mathbf{r}, \mathbf{r}_0) \cdot \mathbf{q}$ for all points $\mathbf{r}$ of the space corresponds exactly to solving the forward problem $V = f(\mathbf{J}^{\mathrm{p}})$ where $\mathbf{J}^{\mathrm{p}}$ is a single dipole with position $\mathbf{r}_0$ and moment $\mathbf{q}$. The forward field at a position $\mathbf{r}_0$ can then be computed by solving the forward problem for three dipoles at position $\mathbf{r}_0$ with moments equal to the three Cartesian orientations $(1, 0, 0)$, $(0, 1, 0)$ and $(0, 0, 1)$. As a consequence, one can approximate the function $(\mathbf{r}, \mathbf{r}') \to \mathbf{L}(\mathbf{r}, \mathbf{r}')$ by evaluating the forward field $\mathbf{r} \to \mathbf{L}(\mathbf{r}, \mathbf{r}_i)$ at many dipole positions $\mathbf{r}_i$.

As explained in section 4, for most of the source models, the brain activity is represented by a certain number k of dipoles $(\mathbf{r}_i, \mathbf{q}_i)$. In this case, an EEG-MEG measurement is given by

$$m(\mathbf{r}) = \sum_{i=1}^{k} \mathbf{L}(\mathbf{r}, \mathbf{r}_i) \cdot \mathbf{q}_i \ .$$

If we consider a complete set of n sensors at positions $(\mathbf{r}_{s1}, \ldots, \mathbf{r}_{sn})$, we can write the relation between the sources and the measurements in a simple matrix product :

$$\mathbf{m} = \begin{bmatrix} m(\mathbf{r}_{s1}) \\ \vdots \\ m(\mathbf{r}_{sn}) \end{bmatrix} = \begin{bmatrix} L(\mathbf{r}_{s1}, \mathbf{r}_1)^T & \cdots & L(\mathbf{r}_{s1}, \mathbf{r}_k)^T \\ \vdots & \ddots & \vdots \\ L(\mathbf{r}_{sn}, \mathbf{r}_1)^T & \cdots & L(\mathbf{r}_{sn}, \mathbf{r}_k)^T \end{bmatrix} \begin{bmatrix} \mathbf{q}_1 \\ \vdots \\ \mathbf{q}_k \end{bmatrix} = \mathbf{G}\mathbf{q} \ . \tag{2.1}$$

$\mathbf{G}$ is called the *gain matrix* or sometimes the *lead field matrix*. Normally, to compute the gain matrix, one has to solve one forward problem per column of the gain matrix. If we consider k dipoles with all the Cartesian orientations, then the forward problem needs to be solved $3k$ times.

5.2 Least-squares dipole fit

This method is based on a dipolar model of the brain activity as presented in section 4.1. In this approach, it is assumed that the brain activity is sparse and focal : at a given time, only a few small areas (or *patches*) of the cortex are activated. As a consequence, the activity of each patch can be represented by one dipole, often called *equivalent dipole*. Then the whole brain activity is represented by a small number of dipoles. In this framework, the goal of the inverse problem is to find the positions and moments of these dipoles. One can assume that the number of dipoles is fixed in advance, if not the number of dipoles becomes an unknown of the problem. Generally, the number of dipoles is always assumed to be far inferior to the number of measurements, so that the problem is overdetermined, and it can be shown that there is a unique solution [2]. We present here the simple approach with a fixed number of dipoles k. The projection of the dipoles on the measurement is given by the gain matrix (2.1), which can be written :

$$\mathbf{m} = \mathbf{G}(\{\mathbf{r}_i\})\mathbf{q}$$

where $\mathbf{G}$ depends on the dipole positions $\{\mathbf{r}_i\}$ and $\mathbf{q}$ is the column vector containing all the moments of the dipoles $\mathbf{q} = [\mathbf{q}_i]$. If we have some real measurements $\mathbf{M}$, the goal is to minimize the following cost function :

$$E(\{\mathbf{r}_i, \mathbf{q}_i\}) = \|\mathbf{M} - \mathbf{m}\|^2 = \|\mathbf{M} - \mathbf{G}\mathbf{q}\|^2 \tag{2.2}$$

where $\|.\|$ is the discrete l^2-norm, such that for a vector $\mathbf{u} = [u_j]$, $\|\mathbf{u}\|^2 = \langle \mathbf{u}, \mathbf{u} \rangle = \sum_j u_j^2$. For the sake of simplicity, $\mathbf{M}$ is supposed to be a column vector corresponding to the measurements at a given time t. For given positions $\{\mathbf{r}_i\}$, the moments $\mathbf{q} = [\mathbf{q}_i]$ that minimize E are obtained by a closed formula. The derivative of E with respect to $\mathbf{q}$ is

$$\partial_{\mathbf{q}} E = 2\mathbf{G}^T (\mathbf{M} - \mathbf{G}\mathbf{q}) \ .$$

The minimum is obtained for $\partial_{\mathbf{q}} E = 0$, which gives :

$$\mathbf{q}^* = \left(\mathbf{G}^T\mathbf{G}\right)^{-1} \mathbf{G}^T\mathbf{M} \ . \tag{2.3}$$

We can replace $\mathbf{q}$ by $\mathbf{q}^*$ in (2.2) so that E only depends on the dipole positions $\{\mathbf{r}_i\}$. The minimization of E with respect to the dipole positions is more complicated, be-

cause E depends on the $\{\mathbf{r}_i\}$ via the gain matrix $\mathbf{G}(\{\mathbf{r}_i\})$, which is not linear with respect to the $\{\mathbf{r}_i\}$. In this case, one has to use iterative methods for the minimization of E. Many minimization methods can be used, such as the Nelder-Mead simplex or the Levenberg-Marquardt method, which is particularly adapted to the least square minimization. In all cases, at each iteration of the minimization algorithm, the dipole positions $\{\mathbf{r}_i\}$ are updated, and so $\mathbf{G}(\{\mathbf{r}_i\})$ has to be recomputed, which means solving $3k$ times the forward problem, as explained in section 5.1. If the dipole fit method is applied at each time sample t of the measurements, then the dipole localizations change over time, this is called the *moving dipole* approach. But one can consider a whole set of measurements over a time window, in this case $\mathbf{M}$ is a matrix $n \times T$, where T is the number of time samples. In this case, (2.3) gives a matrix containing the dipole moments varying over time, but the minimization of E still gives k fixed positions. This is called the *rotating dipole* approach.

5.3 MUSIC

The Multiple Signal Classification (MUSIC) is a method used originally for antennas, which was then applied to MEG-EEG source localization [69]. This method is also used to find a small number k of dipoles, but the approach is different, as it is a scanning approach (section 4.2), and requires to consider some measurements over a certain time window. $\mathbf{M}$ is then a matrix $n \times T$ where n is the number of sensors and T the number of time samples. The idea is to use the singular value decomposition (SVD) of the measurements $\mathbf{M} = \mathbf{USV}^T$. If k is inferior to the number of measurements, and the measurements are not too noisy, then all the signal coming from the k dipoles should be spanned by the k first left singular vectors of $\mathbf{U}$, denoted $\mathbf{U}_k$. The remaining vectors of $\mathbf{U}$ should only span noise. In this framework, $\mathbf{P} = \mathbf{I} - \mathbf{U}_k\mathbf{U}_k^T$ is the orthogonal projector onto the noise subspace. We can then define a cost function with respect to a dipole position $\mathbf{r}_i$:

$$E(\mathbf{r}_i) = \frac{\|\mathbf{PG}(\mathbf{r}_i)\|_F^2}{\|\mathbf{G}(\mathbf{r}_i)\|_F^2} \tag{2.4}$$

where $\mathbf{G}(\mathbf{r}_i)$ is the three column matrix extracted from the gain matrix, corresponding to the forward field of the dipole at position $\mathbf{r}_i$. $\|.\|_F$ is the Frobenius norm for matrices, such that $\|\mathbf{A}\|_F^2 = \sum_i \sum_j a_{ij}^2$. Theoretically, if $E(\mathbf{r}_i) = 0$, it means that all the signal that a dipole at position $\mathbf{r}_i$ can generate is in the signal subspace of the measurements. In this case, $\mathbf{r}_i$ is a true source location. In practical situations, it is of course not possible to get $E(\mathbf{r}_i) = 0$. The common strategy is to regularly sample the space where the brain sources should be, which define a set of positions $\{\mathbf{r}_i\}$, and then to find the k best local minima of $E(\mathbf{r}_i)$. These k local minima give directly the k dipole positions, and then the moments of these dipoles are computed with a closed formula like for the dipole fit approach. For this method, the number of times that the forward problem has to be solved depends on how the source space is sampled. We need to compute $\mathbf{G}(\mathbf{r}_i)$ for every space sample $\mathbf{r}_i$. For instance, if we take a regular $10 \times 10 \times 10$ grid enclosing the brain, the forward problem has to be computed for 3000 different dipoles (1000 positions with the three Cartesian orientations).

5.4 Distributed sources

In this approach, many dipoles with fixed positions are regularly distributed in the brain region, and the goal is to estimate the moments of all the dipoles at the same time. It can be seen as a way of estimating a discretization of the primary current $\mathbf{J}^{\mathrm{p}}$. Because the activity measured in EEG-MEG comes from the pyramidal neurons mostly located in the deep layers of the gray matter, the dipoles are generally distributed over a surface corresponding to the interface between white and gray matter. Typically, the cortical surface can be well described with about 10000 dipoles.

Now that the dipole positions are fixed, we have a simple linear relationship between the dipole moments and the measurements :

$$\mathbf{m} = \mathbf{G}\mathbf{q} \ .$$

This can be even more simplified if one assumes that the dipole moments are perpendicular to the cortical surface (because of the pyramidal neuron structure). The orientations are also fixed and the only unknowns are the amplitudes of the dipoles. It gives a similar linear system of smaller dimension $\mathbf{m} = \mathbf{H}\mathbf{s}$. Nevertheless, because of the number of dipoles, the problem is now underdetermined. The closed form (2.3) for finding $\mathbf{q}$ is not valid anymore because in this case $\mathbf{G}$ is a matrix with far more columns than rows, so it cannot be of full rank. Any $\mathbf{q}$ in the kernel of $\mathbf{G}$ is a silent source, and so there is no unique solution.

For the problem to have a unique solution, one has to add more constraints. This is generally done by adding a regularization term R to the cost function :

$$E(\mathbf{q}) = \|\mathbf{M} - \mathbf{G}\mathbf{q}\|^2 + R(\mathbf{q}) \ .$$

If R is strictly convex, then there is a unique minimum to E. The simplest choice for R is the classic Tikhonov regularization :

$$R(\mathbf{q}) = \lambda \|\mathbf{W}\mathbf{q}\|^2 \ ,$$

where $\|\cdot\|$ is the Euclidean norm or l^2-norm, and $\mathbf{W}$ is a matrix which allows to put priors on the solution. If $\mathbf{W} = \mathbf{I}$ is the identity matrix, then the regularization gives preference to solutions with smaller norms, and the effect of regularization can be controlled with the scale factor λ. $\mathbf{W}$ can also be used to discretize the gradient or Laplacian operator, in this case the regularization tends to minimize the norm of the gradient or the norm of the Laplacian of the solution. The matrix $\mathbf{W}$ is also used to incorporate information about the sources : it can put balance between deep and superficial sources, or incorporate the covariance of the sources. The general solution $\hat{\mathbf{q}}$ is then given by the formula :

$$\hat{\mathbf{q}} = \left(\mathbf{G}^T\mathbf{G} + \lambda \mathbf{W}^T\mathbf{W}\right)^{-1} \mathbf{G}^T\mathbf{M} \ ,$$

where the notation $^{-1}$ is meant as a pseudoinverse. The problem is that the square matrix $\left(\mathbf{G}^T\mathbf{G} + \lambda \mathbf{W}^T\mathbf{W}\right)$ has a size corresponding to the number of dipoles, and computing its inverse can be computationally very expensive. Using the matrix

inversion lemma, another closed formula for the solution can be derived :

$$\hat{\mathbf{q}} = (\mathbf{W}^T\mathbf{W})^{-1}\mathbf{G}^T \left(\mathbf{G}(\mathbf{W}^T\mathbf{W})^{-1}\mathbf{G}^T + \lambda\mathbf{I}\right)^{-1}\mathbf{M} \ ,$$

for which the matrix to be inverted, $\left(\mathbf{G}(\mathbf{W}^T\mathbf{W})^{-1}\mathbf{G}^T + \lambda\mathbf{I}\right)$, has now a size equal to the number of sensors. This inverse is computationally cheaper to obtain, provided that $(\mathbf{W}^T\mathbf{W})^{-1}$ can be calculated at low cost.

With the distributed approaches, the gain matrix to be generated is usually big, with a number of columns equal to the number of dipoles that are distributed in the head domain.

6 IMPORTANCE OF THE HEAD MODEL

The section 5 shows that all source localization methods are based on the knowledge of the gain matrix $\mathbf{G}$. For a given source, this gain matrix gives the values at the sensors of the electromagnetic field produced by this source. To be able to generate such a matrix, one needs to build and compute a model which describes how the electromagnetic field propagates in the head. If this model does not reproduce accurately the propagation of the electromagnetic field in a real human head, then the values of the gain matrix are directly affected and the results of the source localization methods are subject to errors. As a consequence, the accuracy of the head model directly affects the accuracy of the source localization methods. This is particularly important for EEG and less for MEG : as explained in section 2, the variation of the electrical conductivity in the head compartment affects the propagation of the electric potential, whereas the magnetic field is less sensitivite to conductivity changes. It has been shown that if the head is described as a simple spherical conductor, the dipole localization errors in EEG can be of the order of 3 cm compared to intracranial localizations [99]. There are two important factors for a good model of the head :

- The shape of the head model : it must represent as well as possible the shape of the head of the subject. In the most simple models, the head is described as a homogeneous spherical conductor for MEG, or as a three or four-layered spherical conductor for EEG, in aim to take into account the low conductivity of the skull and the high conductivity of the cerebrospinal fluid (CSF). Nowadays, MRI is a pretty common modality that can provide a 3d image of the anatomy of the head subjects. It is thus possible to segment the MRI and to get a realistic model of the head, describing precisely the different tissues that compose the head : scalp, skull, CSF, gray matter, white matter.

- The electrical conductivity of the head model : it affects the propagation of the electromagnetic field and must be chosen such that the propagation in the head model approximates as best as possible the propagation in the head of the subject. There is no technique yet to get an accurate 3d image of the human head conductivity. Hence the choice of the conductivity of the head models in EEG and MEG is mainly based on in vitro measures or in vivo measures on animals. Usually, the head model is divided in several compartments corresponding to

homogeneous tissues (scalp, skull, gray matter) and a constant conductivity is associated to each compartment based on the measures that can be found in the literature.

How to build and compute such a model is commonly referred to as the forward problem, and is described in detail in chapter 3.

CHAPTER 3

THE FORWARD PROBLEM

In this chapter, we review the equations and methods for solving the forward problem.

Contents

1 THE PHYSICS OF EEG AND MEG

1.1 Notation

The space we consider is $\mathbb{R}^3$. All vectors are denoted in bold characters. The vector indicating the position of a point r of $\mathbb{R}^3$ is denoted $\mathbf{r}$. In the following, we use vector calculus notation, with the "nabla" operator ∇. For a real function $f(\mathbf{r})$, ∇f is the gradient of f. For a vector field $\mathbf{X}(\mathbf{r})$, $\nabla \cdot \mathbf{X}$ is the divergence of this field (a scalar) and $\nabla \times \mathbf{X}$ is the curl of this field (a vector).

1.2 Maxwell's equations

Maxwell's equations relate the electromagnetic field to the charge density and current density. We denote $\mathbf{E}$ the electric field, $\mathbf{B}$ the magnetic field, ρ the charge density and $\mathbf{J}$ the current density. Maxwell's equations are a set of four partial differential equations :

$$\begin{array}{ll} \nabla \cdot \mathbf{E} = \frac{\rho}{\epsilon} & \nabla \times \mathbf{E} = -\frac{\partial \mathbf{B}}{\partial t} \\ \nabla \cdot \mathbf{B} = 0 & \nabla \times \mathbf{B} = \mu \left(\mathbf{J} + \epsilon \frac{\partial \mathbf{E}}{\partial t} \right) \end{array} \tag{3.1}$$

ϵ is the electrical permittivity of the medium and μ is the magnetic permeability. For human tissues, the magnetic permeability μ is the same as for vacuum $\mu = \mu_0$, whereas the relative electrical permittivity $\epsilon_r = \frac{\epsilon}{\epsilon_0}$ can vary a lot depending on tissue and frequency. For instance, at a frequency of $100Hz$, ϵ_r is around 4×10^6 for gray matter, 5×10^5 for fat and 6×10^3 for compact bone [30]. The relation between the charge density and the current density is

$$\nabla \cdot \mathbf{J} = -\frac{\partial \rho}{\partial t} \ . \tag{3.2}$$

In particular, in a passive (no charge, nor current generator) non-magnetic medium, $\mathbf{J}$ is simply the sum of the ohmic current and the polarization current :

$$\mathbf{J} = \sigma \mathbf{E} + \frac{\partial \mathbf{P}}{\partial t} \ , \tag{3.3}$$

where $\mathbf{P} = (\epsilon - \epsilon_0)\mathbf{E}$ is the polarization and σ is the conductivity of the medium.

1.3 Quasi-static approximation

We explained in chapter 1, section 1 that the post-synaptic potentials have a duration of about $10ms$. As a consequence, it is commonly accepted that the time frequencies of the brain electromagnetic field that can be observed outside the head can rarely exceed $100Hz$. For such low frequencies, the time derivatives in Maxwell's equations can be neglected, this is called the quasi-static approximation.

A justification of the quasi-static approximation can be found in [41]. Let us illustrate it with some orders of magnitude. We know that in a simple medium, the general solution of the electromagnetic wave equation can be written as a linear superposition of planar waves of different frequencies and polarizations. Let us just

consider one planar wave for the sake of simplicity. Its equation is :

$$\mathbf{E}(\mathbf{r},t) = \mathbf{E}_0 e^{i2\pi\mathbf{k}\cdot\mathbf{r}} e^{i2\pi ft} \quad , \tag{3.4}$$

where i is the imaginary unit, $\mathbf{E}_0$ is a real amplitude vector contained in the wave plane, k is a real spatial frequency vector normal to the wave plane ($\mathbf{E}_0 \cdot \mathbf{k} = 0$), and f is the temporal frequency. One of Maxwell's equations including a time derivative is

$$\nabla \times \mathbf{B} = \mu_0 \left(\sigma\mathbf{E} + \epsilon \frac{\partial \mathbf{E}}{\partial t} \right) \quad ,$$

for a passive non-magnetic medium. To neglect the time derivative, we must have $\|\epsilon \frac{\partial \mathbf{E}}{\partial t}\| << \|\sigma\mathbf{E}\|$, which for the planar wave is equivalent to $\kappa = |2\pi f \frac{\epsilon}{\sigma}| << 1$. For the head tissues, at a frequency of $100Hz$, the average permittivity is $\epsilon = 10^5\epsilon_0$ and the average conductivity is $\sigma = 0.3\Omega^{-1}m^{-1}$. With these values, we have $\kappa = 1,8 \times 10^{-3}$, so we can neglect the term $\epsilon \frac{\partial \mathbf{E}}{\partial t}$.

More intuitively, we can just consider the spatial wavelength λ of our planar wave which is given by the relation $c = f\lambda$, where $c = \frac{1}{\sqrt{\mu\epsilon}}$ is the speed of the wave in the medium and f is the temporal frequency of the wave. With a frequency of $100Hz$, it gives us a spatial wavelength of about $10^5 m$. So at the scale of a human head, we can neglect the oscillations of the wave, which gives $\nabla \times \mathbf{E} = 0$ instead of $\nabla \times \mathbf{E} = -\frac{\partial \mathbf{B}}{\partial t}$.

1.4 The electric potential equation

In the quasi-static approximation, we neglect all the time derivatives. As a consequence, the curl of the electric field $\mathbf{E}$ is zero, meaning that it derives from a scalar potential V :

$$\mathbf{E} = -\nabla V. \tag{3.5}$$

In equation (3.3), the term $\frac{\partial \mathbf{P}}{\partial t}$ is null, but because the brain is not a passive medium, we need to add the contribution of a *primary current* $\mathbf{J}^{\mathrm{p}}$ reflecting the brain electrical activity :

$$\mathbf{J} = \mathbf{J}^{\mathrm{p}} + \sigma\mathbf{E} = \mathbf{J}^{\mathrm{p}} - \sigma\nabla V \quad . \tag{3.6}$$

As opposed to the primary current, $\sigma\mathbf{E}$ can be referred to as passive current, ohmic current or volume current. Neglecting the time derivative in (3.2) also states that $\nabla \cdot \mathbf{J} = 0$, which finally leads to the potential equation :

$$\boxed{\nabla \cdot (\sigma \nabla V) = \nabla \cdot \mathbf{J}^{\mathrm{p}} \quad .} \tag{3.7}$$

1.5 The magnetic field equation : the Biot-Savart law

Because $\nabla \cdot \mathbf{B} = 0$, $\mathbf{B}$ derives from a vector potential $\mathbf{A}$:

$$\mathbf{B} = \nabla \times \mathbf{A} \quad ,$$

and we use the classical gauge condition $\nabla \cdot \mathbf{A} = 0$ to avoid the indetermination related to the definition of $\mathbf{A}$. We now have :

$$\nabla \times \mathbf{B} = \nabla \times \nabla \times \mathbf{A} = \nabla (\nabla \cdot \mathbf{A}) - \Delta \mathbf{A} = -\Delta \mathbf{A} \ .$$

Maxwell's equation $\nabla \times \mathbf{B} = \mu_0 \mathbf{J}$ becomes $\Delta \mathbf{A} = -\mu_0 \mathbf{J}$, which is a Poisson equation. If we impose $\mathbf{A}(\infty) = 0$ (no magnetic field at infinity), it has a general solution in $\mathbb{R}^3$:

$$\mathbf{A}(\mathbf{r}) = \frac{\mu_0}{4\pi} \int_{\mathbb{R}^3} \frac{\mathbf{J}(\mathbf{r}')}{\|\mathbf{r} - \mathbf{r}'\|} dr' \ .$$

Taking the curl, we obtain the Biot-Savart law :

$$\mathbf{B}(\mathbf{r}) = \frac{\mu_0}{4\pi} \int_{\mathbb{R}^3} \mathbf{J}(\mathbf{r}') \times \frac{(\mathbf{r} - \mathbf{r}')}{\|\mathbf{r} - \mathbf{r}'\|^3} dr' \ .$$

Because the current can be written as $\mathbf{J} = \mathbf{J}^{\mathrm{p}} - \sigma \nabla V$, we can transform the Biot-Savart law into :

$$\boxed{\mathbf{B}(\mathbf{r}) = \mathbf{B}_0(\mathbf{r}) - \frac{\mu_0}{4\pi} \int_{\mathbb{R}^3} \sigma \nabla V(\mathbf{r}') \times \frac{(\mathbf{r}-\mathbf{r}')}{\|\mathbf{r}-\mathbf{r}'\|^3} dr' \ ,} \tag{3.8}$$

with

$$\mathbf{B}_0(\mathbf{r}) = \frac{\mu_0}{4\pi} \int_{\mathbb{R}^3} \mathbf{J}^{\mathrm{p}}(\mathbf{r}') \times \frac{(\mathbf{r} - \mathbf{r}')}{\|\mathbf{r} - \mathbf{r}'\|^3} dr' \ .$$

With this formulation, $\mathbf{B}_0$ is often referred as the *primary* magnetic field while the second term is called the *secondary* magnetic field.

2 UNBOUNDED HOMOGENEOUS MEDIUM

If we consider a conductor which consists of the whole space with a constant conductivity σ, then equation (3.7) becomes

$$\Delta V = \frac{1}{\sigma} \nabla \cdot \mathbf{J}^{\mathrm{p}} \ ,$$

which is a Poisson equation of general solution

$$V(\mathbf{r}) = \frac{1}{4\pi\sigma} \int_{\mathbb{R}^3} \frac{\nabla \cdot \mathbf{J}^{\mathrm{p}}(\mathbf{r}')}{\|\mathbf{r} - \mathbf{r}'\|} dr' \ ,$$

with V vanishing at infinity. Applying the divergence theorem, it becomes

$$\boxed{V(\mathbf{r}) = \frac{1}{4\pi\sigma} \int_{\mathbb{R}^3} \mathbf{J}^{\mathrm{p}}(\mathbf{r}') \cdot \frac{(\mathbf{r}-\mathbf{r}')}{\|\mathbf{r}-\mathbf{r}'\|^3} dr' \ .} \tag{3.9}$$

For the magnetic field, we can take σ out of the integral in (3.8) because it is constant :

$$\mathbf{B}(\mathbf{r}) = \mathbf{B}_0(\mathbf{r}) - \frac{\mu_0 \sigma}{4\pi} \int_{\mathbb{R}^3} \nabla V(\mathbf{r}') \times \frac{(\mathbf{r} - \mathbf{r}')}{\|\mathbf{r} - \mathbf{r}'\|^3} dr' \ . \tag{3.10}$$

Using the identity

$$\nabla V(\mathbf{r}') \times \frac{(\mathbf{r}-\mathbf{r}')}{\|\mathbf{r}-\mathbf{r}'\|^3} = \nabla \times \left(\frac{\nabla V(\mathbf{r}')}{\|\mathbf{r}-\mathbf{r}'\|} \right) - \frac{\nabla \times (\nabla V(\mathbf{r}'))}{\|\mathbf{r}-\mathbf{r}'\|}$$

and the fact that the curl of a gradient is null, the integral in the right hand side of (3.10) becomes

$$\int_{\mathbb{R}^3} \nabla \times \left(\frac{\nabla V(\mathbf{r}')}{\|\mathbf{r}-\mathbf{r}'\|} \right) dr' \ .$$

Because V vanishes at infinity, it is easy to show with Stokes' theorem that this integral is null. So finally, in an infinite homogeneous medium, the magnetic field reduces to the primary field :

$$\boxed{\mathbf{B}(\mathbf{r}) = \mathbf{B}_0(\mathbf{r}) = \frac{\mu_0}{4\pi} \int_{\mathbb{R}^3} \mathbf{J}^{\mathrm{p}}(\mathbf{r}') \times \frac{(\mathbf{r}-\mathbf{r}')}{\|\mathbf{r}-\mathbf{r}'\|^3} dr' \ .} \tag{3.11}$$

In this special case, the passive current $\sigma\mathbf{E} = -\sigma\nabla V$ does not contribute to the magnetic field.

2.1 Dipolar sources

If the primary current $\mathbf{J}^{\mathrm{p}}$ is reduced to a single dipole at position $\mathbf{r}_0$ with moment $\mathbf{q}$, then $\mathbf{J}^{\mathrm{p}}(\mathbf{r}) = \delta_{\mathbf{r}_0}\mathbf{q}$, where δ is the Dirac distribution and $\delta_{\mathbf{r}_0} = \delta(\mathbf{r}-\mathbf{r}_0)$. For such a primary current, the potential and magnetic field in an homogeneous space have very simple formulations :

$$V(\mathbf{r}) = \frac{1}{4\pi\sigma}\mathbf{q} \cdot \frac{(\mathbf{r}-\mathbf{r}_0)}{\|\mathbf{r}-\mathbf{r}_0\|^3} \tag{3.12}$$

$$\mathbf{B}(\mathbf{r}) = \frac{\mu_0}{4\pi}\mathbf{q} \times \frac{(\mathbf{r}-\mathbf{r}_0)}{\|\mathbf{r}-\mathbf{r}_0\|^3} \tag{3.13}$$

It is therefore very convenient to use the dipole model for the primary current. Actually, if $\mathbf{J}^{\mathrm{p}}$ is contained in a small volume compared to the distance to the observation point $\mathbf{r}$, then the dipole is a good approximation. For instance, for such a small volume vol, the potential at $\mathbf{r}$ is

$$V(\mathbf{r}) = \frac{1}{4\pi\sigma} \int_{vol} \mathbf{J}^{\mathrm{p}}(\mathbf{r}') \cdot \frac{(\mathbf{r}-\mathbf{r}')}{\|\mathbf{r}-\mathbf{r}'\|^3} dr' \approx \frac{1}{4\pi\sigma}\mathbf{q} \cdot \frac{(\mathbf{r}-\mathbf{r}_0)}{\|\mathbf{r}-\mathbf{r}_0\|^3} \ ,$$

where $\mathbf{r}_0$ is the centroid of the volume vol containing $\mathbf{J}^{\mathrm{p}}$ and $\mathbf{q} = \int_{vol} \mathbf{J}^{\mathrm{p}}(\mathbf{r}')dr'$. The same approximation can be used for the magnetic field.

3 THE SPHERICAL HEAD MODEL

Obviously, the human head is not an infinite homogeneous conductor. First of all, it is a bounded conductor and no electric current can flow outside the head (except at the neck). Secondly, the electrical conductivity σ of the head is not constant : for instance, it is commonly accepted that the skull is between twenty and one hundred

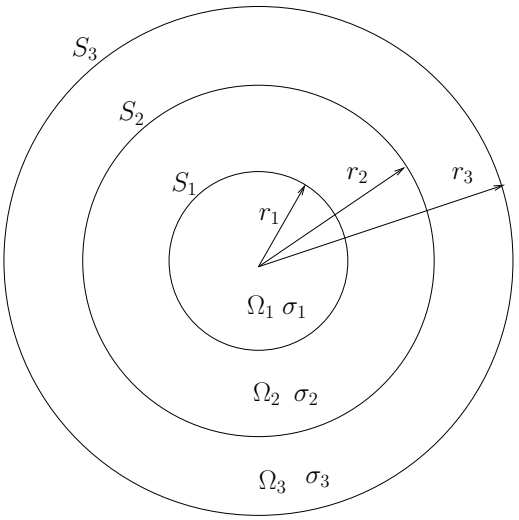

Figure 3.1: A spherical model with three layers.

times less conductive than other head tissues. This must be taken into account to get more accurate formulations of the potential and magnetic field generated by the brain electrical activity. A first step towards head modeling is to consider the head as a set of nested spheres. Each volume enclosed between two spheres is supposed to represent a different tissue of the head, with a constant conductivity. Figure 3.1 shows a spherical model with three spheres. Without respect to proportions, it could represent the brain, the skull and the scalp of a human head. This type of model is a very coarse description of the head, but the simple geometry allows to find an analytic solution for the electric potential generated by a dipole, like for the infinite homogeneous medium (3.12).

3.1 Electric potential generated by a dipole

The key point is to take advantage of the spherical symmetry of the geometry. First, we use spherical coordinates (r, θ, ϕ) instead of Cartesian coordinates, and second, we decompose the electric potential on the spherical harmonics basis $Y_l^m(\theta, \phi)$. The spherical harmonics have the following form :

$$Y_l^m(\theta, \phi) = N_l^m P_l^m(cos\theta) e^{im\phi}, \;\; l \in \mathbb{N}, m \in \mathbb{Z}, \;\; |m| < l \;\; ,$$

where N_l^m is a normalization coefficient and P_l^m is an associated Legendre function. This basis is interesting in our case because the general solution of Laplace's equation $\Delta f = 0$ in spherical coordinates can be written as a linear combination of spherical harmonics

$$f(r, \theta, \phi) = \sum_{l=0}^{\infty} \sum_{m=-l}^{l} (A_{lm} r^{-1-l} + B_{lm} r^l) Y_l^m(\theta, \phi) \;\; .$$

If f is a real function, it simplifies to

$$f(r,\theta,\phi) = \sum_{l=0}^{\infty}\sum_{m=0}^{l}(A_{lm}r^{-1-l} + B_{lm}r^{l})P_l^m(cos\theta)cos(m\phi) \ .$$

A function f such that $\Delta f = 0$ is called a harmonic function.

Now let us consider a current dipole inside the spherical model. We denote $\mathbf{r}_0$ its position and $\mathbf{q}$ its moment. We use the notations presented in figure 3.1, with the indices increasing from the innermost sphere to the outermost one. In all the subregions Ω_k where the dipole is not located, the potential equation states that $\nabla \cdot (\sigma_k \nabla V) = \sigma_k \Delta V = 0$ because σ_k is constant. As a consequence,the restriction V_k of V in each domain Ω_k is harmonic and can be decomposed on the spherical harmonic basis :

$$\boxed{V_k(r,\phi,\theta) = \textstyle\sum_{l=0}^{\infty}\sum_{m=0}^{l}(A_{lm}^k r^{-1-l} + B_{lm}^k r^{l})P_l^m(cos\theta)cos(m\phi) \ .} \tag{3.14}$$

In the domain Ω_{k^*} where the dipole is located, the potential V verifies $\sigma_{k^*}\Delta V = \nabla \cdot \mathbf{J}^{\mathrm{p}}$, with $\mathbf{J}^{\mathrm{p}} = \delta(\mathbf{r} - \mathbf{r}_0)\mathbf{q}$. So we can decompose the potential in $V = v + u$, where v is the potential generated by the dipole in an infinite homogeneous domain of conductivity σ_{k^*}, and u is an harmonic function. The function v is defined as

$$v(\mathbf{r}) = \frac{1}{4\pi\sigma_{k^*}}\mathbf{q} \cdot \frac{(\mathbf{r} - \mathbf{r}_0)}{\|\mathbf{r} - \mathbf{r}_0\|^3} \ .$$

This function can be decomposed in the spherical harmonic basis

$$v(r,\phi,\theta) = \begin{cases} \sum_{l=0}^{\infty}\sum_{m=0}^{l} q_{lm}^{inf} r^l P_l^m(cos\theta)cos(m\phi) \ , & r < r_0 \\ \sum_{l=0}^{\infty}\sum_{m=0}^{l} q_{lm}^{sup} r^{-1-l} P_l^m(cos\theta)cos(m\phi) \ , & r > r_0 \end{cases}$$

So if we note $A_{lm}^{k^*}$ and $B_{lm}^{k^*}$ the coefficients of the decomposition of u, we have a decomposition of V_{k^*} in the spherical harmonic basis

$$\boxed{V_{k^*}(r,\phi,\theta) = \begin{cases} \sum_{l=0}^{\infty}\sum_{m=0}^{l}(A_{lm}^{k^*} r^{-1-l} + (q_{lm}^{inf} + B_{lm}^{k^*})r^l)P_l^m(cos\theta)cos(m\phi) \ , & r < r_0 \\ \sum_{l=0}^{\infty}\sum_{m=0}^{l}((A_{lm}^{k^*} + q_{lm}^{sup})r^{-1-l} + B_{lm}^{k^*} r^l)P_l^m(cos\theta)cos(m\phi) \ , & r > r_0 \end{cases}} \tag{3.15}$$

Finally, to fully determine the potential in the whole domain Ω, one only needs to fix the value of the coefficients A_{lm}^k and B_{lm}^k. This is done by considering the boundary conditions at each surface S_k. The electric potential and the current density must be continuous through the interfaces :

$$\begin{cases} V_k(r_k,\phi,\theta) = V_{k+1}(r_k,\phi,\theta) \\ \sigma_k \frac{\partial V_k}{\partial r}(r_k,\phi,\theta) = \sigma_{k+1}\frac{\partial V_{k+1}}{\partial r}(r_k,\phi,\theta) \end{cases} \tag{3.16}$$

From (3.14), (3.15) and (3.16), a linear system can be built for the A_{lm}^k and B_{lm}^k, hence determining the values of these coefficients. Because of the infinite series, in practical situations one has to choose at which order this series has to be truncated. For high orders, the solution is more accurate but the computation is more expensive. Several formulations have been proposed for efficient computation of the electric potential in multilayer spheres [24, 8, 118].

3.2 The magnetic field

In the case of the magnetic field, there is no need to use an infinite series based on a decomposition in spherical harmonics. In a spherical geometry, the magnetic field has a simple closed form.

3.2.1 The radial component of the magnetic field

We consider again a spherical geometry as described by figure 3.1. With the spherical coordinates, the radial component of the magnetic field is

$$\mathbf{B}_r(\mathbf{r}) = \mathbf{B}(\mathbf{r}) \cdot \mathbf{e}_r = \mathbf{B}(\mathbf{r}) \cdot \frac{\mathbf{r}}{r} \ ,$$

and the outward normal at each surface S_k is

$$\mathbf{n}(\mathbf{r}') = \frac{\mathbf{r}'}{r'} \ .$$

The spherical geometry 3.1 is a special case of geometry with a piecewise constant conductivity, and so the magnetic field can be expressed using the formula (3.19) described in section 4.1. If we compute the radial component of the magnetic field, the following scalar triple product appears in the surface integrals :

$$\frac{(\mathbf{r}-\mathbf{r}')}{\|\mathbf{r}-\mathbf{r}'\|^3} \times \frac{\mathbf{r}'}{r'} \cdot \frac{\mathbf{r}}{r} \ .$$

This quantity is zero because $\mathbf{r}$,$\mathbf{r}'$ and $(\mathbf{r}-\mathbf{r}')$ are in the same plane. As a consequence, in a spherical geometry, the radial component of the magnetic field is equal to the radial component of the primary field :

$$\mathbf{B}_r(\mathbf{r}) = \mathbf{B}_{0_r}(\mathbf{r}) = \frac{\mu_0}{4\pi} \int_\Omega \mathbf{J}^{\mathrm{p}} \times \frac{(\mathbf{r}-\mathbf{r}')}{\|\mathbf{r}-\mathbf{r}'\|^3} \cdot \mathbf{e}_r dr' \ .$$

3.2.2 Total magnetic field generated by a dipole

We assume that $\mathbf{J}^{\mathrm{p}}$ is a dipole at position $\mathbf{r}_0$ and with moment $\mathbf{q}$. Outside the domain Ω, there is no current, the Maxwell's equations in the quasistatic approximation state that $\nabla \times \mathbf{B} = 0$. As a consequence, outside Ω, $\mathbf{B}$ derives from a scalar potential U :

$$\mathbf{B} = -\nabla U \ ,$$

with U vanishing at infinity. For $\mathbf{r}$ outside Ω, we can then write the following line integral :

$$\begin{aligned} U(\mathbf{r}) &= -\int_0^\infty \nabla U(\mathbf{r}+t\mathbf{e}_r) \cdot \mathbf{e}_r dt \\ &= \int_0^\infty \mathbf{B}_r(\mathbf{r}+t\mathbf{e}_r) \cdot \mathbf{e}_r dt \\ &= \int_0^\infty \mathbf{B}_{0_r}(\mathbf{r}+t\mathbf{e}_r) \cdot \mathbf{e}_r dt \\ &= \frac{\mu_0}{4\pi} \mathbf{q} \times (\mathbf{r}-\mathbf{r}_0) \cdot \mathbf{e}_r \int_0^\infty \frac{1}{\|\mathbf{r}+t\mathbf{e}_r-\mathbf{r}_0\|^3} dt \end{aligned}$$

The computation of the integral in the right hand side leads to

$$U(\mathbf{r}) = -\frac{\mu_0}{4\pi} \frac{\mathbf{q} \times \mathbf{r}_0 \cdot \mathbf{r}}{F} \ ,$$

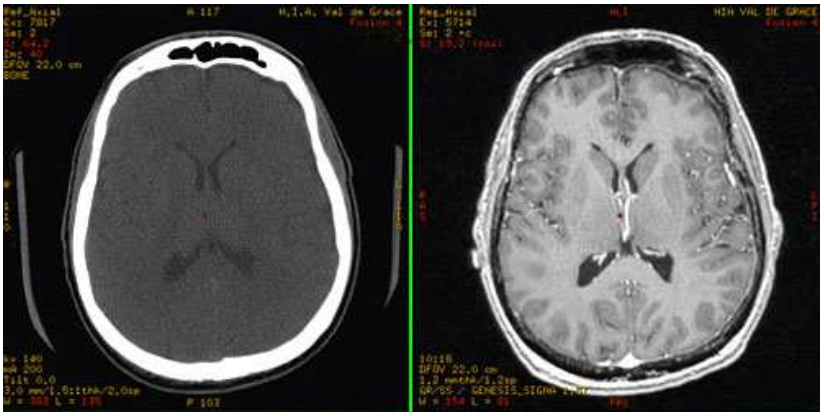

Figure 3.2: On the left, a slice of a CT image. On the right, the same slice obtained with T1 MRI. (Source gehealthcare.com).

where $F = a(ra + r^2 - \mathbf{r}_0 \cdot \mathbf{r})$ with $\mathbf{a} = \mathbf{r} - \mathbf{r}_0$ and $a = \|\mathbf{a}\|$. Taking the gradient, we have a formulation of the total magnetic field :

$$\boxed{\mathbf{B}(\mathbf{r}) = \frac{\mu_0}{4\pi F^2}(F\mathbf{q} \times \mathbf{r}_0 - \mathbf{q} \times \mathbf{r}_0 \cdot \mathbf{r}\nabla F) \ .} \tag{3.17}$$

This formula for the total magnetic field generated by a dipole in a spherical geometry is due to Sarvas [88]. It is interesting to note that although it is different from the formula in an infinite homogeneous medium, it is also independent of the conductivity σ of the domain Ω.

3.3 Limits of spherical models

These analytical or semi-analytical formulas of the electromagnetic field can be extended to eccentric spheres [66], or to ellipsoidal geometries [21]. Nevertheless, several studies have shown that these kind of models are not sufficient to take into account the effects due to the head geometry, and that realistic models are necessary to correctly describe the electromagnetic propagation in the human head [17, 49, 12].

4 REALISTIC HEAD MODELS

To improve the head model, it is necessary to take into account the real geometry of the head, which of course is not spherical. This can be achieved thanks to 3d imaging modalities that can produce images of the head anatomy. The oldest one is the X-ray computed tomography (CT), which reconstructs a 3d image from a large series of two-dimensional X-ray images. Its main advantage is that the bones produce a very high signal compared to other tissues, so the skull can be accurately modeled from a CT image. But the CT technique exposes the subject to a high quantity of ionizing radiation and as a consequence it is dedicated to diagnostic purposes and it is almost never used on subjects chosen for an EEG or MEG experiment. The other imaging modality is the magnetic resonance imaging (MRI), which uses a magnetic field to measure the relaxation time of protons. Since protons in differ-

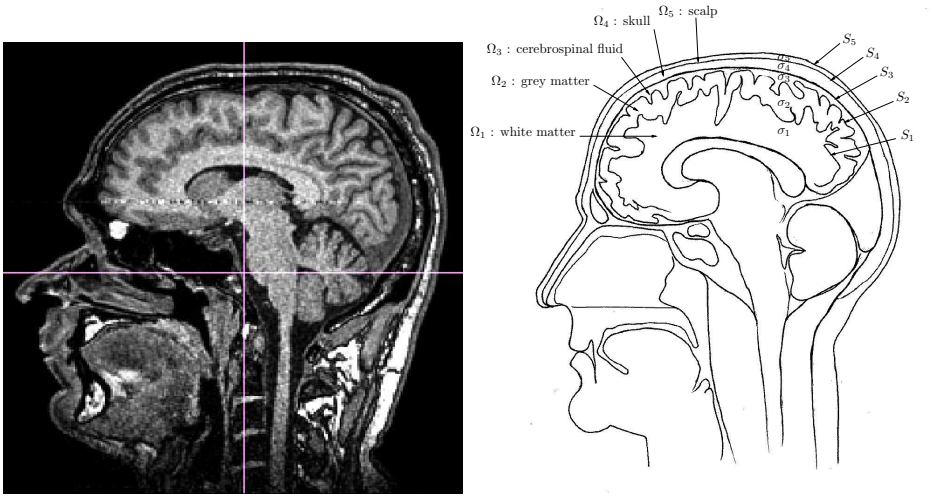

(a) Sagittal cross section of an anatomical MR volume image.

(b) The domains extracted from an MRI.

Figure 3.3: An example of piecewise constant head model.

ent tissues of the body have different relaxation times, the different structures of the body can be revealed. The advantage of MRI compared to CT is that it does not expose the patient to the hazards of ionizing radiation. It is thus much more used as an imaging technique for subjects of an EEG-MEG experiment. The signal obtained with MRI gives a good contrast between soft tissues (white matter, gray matter, fat, muscle) compared to CT, but not for hard tissues (bones, skull) or liquids (cerebro-spinal fluid). Hence, precise models of the brain tissues can be built from MR images, but the skull is most of the time not clearly visible and the skull models obtained from MRI are less accurate. CT and MRI images of the same subject are shown in figure 3.2.

4.1 The piecewise constant approximation

From an MRI of the subject, it is possible to extract surfaces describing the anatomy of the head. Such surfaces are the head contour, the outer and inner skull surfaces, or the gray matter contours. The figure 3.3 shows the kind of geometry that can be extracted from the MRI of a subject's head. From these surfaces, the simplest model consists in assigning a constant conductivity to each region located between two surfaces, like for the spherical model. Practically, each subregion corresponds to a certain type of head tissue which is supposed to be sufficiently homogeneous to have a constant conductivity. The conductivity of the head is hence approximated by a piecewise constant function, which is constant in each tissue and discontinuous at the interfaces between tissues. So we can consider the head as a domain Ω composed of several subregions Ω_k separated by surfaces S_k, each with a constant conductivity σ_k, and with $\sigma = 0$ outside Ω.

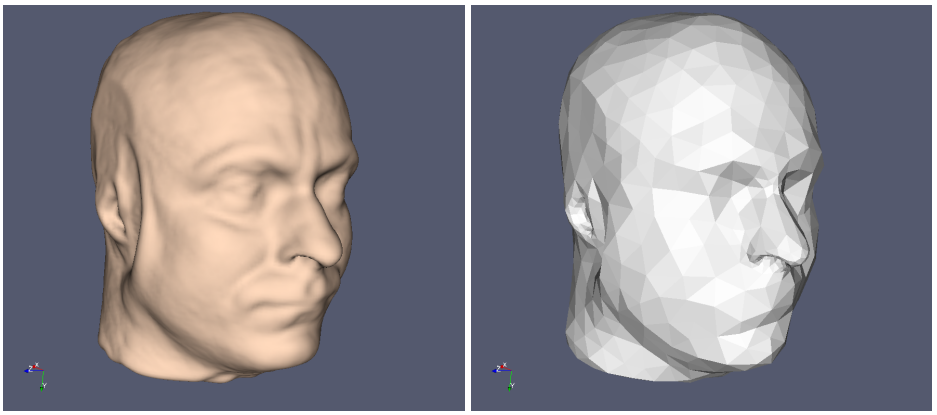

(a) The scalp surface extracted from an MRI. (b) An approximation with triangles.

Figure 3.4: A triangulated surface.

In this case, the equations (3.7) and (3.8) can be rewritten as integral equations :

$$\text{on } S_k, \quad \frac{\sigma_k + \sigma_{k+1}}{2} V(\mathbf{r}) = V_0(\mathbf{r}) - \frac{1}{4\pi} \sum_l (\sigma_l - \sigma_{l+1}) \int_{S_l} V(\mathbf{r}') \nabla \left(\frac{1}{R} \right) \cdot \mathbf{n}_l(\mathbf{r}') ds' \quad (3.18)$$

$$\mathbf{B}(\mathbf{r}) = \mathbf{B}_0(\mathbf{r}) - \frac{\mu_0}{4\pi} \sum_l (\sigma_l - \sigma_{l+1}) \int_{S_l} V(\mathbf{r}') \frac{(\mathbf{r} - \mathbf{r}')}{\|\mathbf{r} - \mathbf{r}'\|^3} \times \mathbf{n}_l(\mathbf{r}') ds' \quad (3.19)$$

where V_0 and $\mathbf{B}_0$ are the electric potential and magnetic field generated by the primary current distribution $\mathbf{J}^{\mathrm{p}}$ in a homogeneous domain. These formulas are due to Geselowitz [32, 33]. The details on how to derive these equations are given in appendix C. For general geometries, there is no analytic solutions to these equations, and only an approximate solution can be obtained, often called numerical solution.

4.2 The Boundary Element Method

The boundary element method is a numerical computational method of solving linear partial differential equations which have been formulated as integral equations, such as (3.18). Hence, for EEG and MEG, this method is valid only for a piecewise constant conductivity model. We describe here how to solve the equation (3.18) for the potential.

The key point of the method is to look for a solution in a very simple space. Normally, the electric potential is a square integrable function. So if we note $S = \cup_k S_k$ the union of the surfaces S_k, and E the space of functions square integrable on S, then the problem of solving the potential equation can be written :

Find $V \in E$ such that

$$\forall k, \ \forall \mathbf{r} \in S_k, \ \frac{\sigma_k + \sigma_{k+1}}{2} V(\mathbf{r}) = V_0(\mathbf{r}) - \frac{1}{4\pi} \sum_l (\sigma_l - \sigma_{l+1}) \int_{S_l} V(\mathbf{r}') \frac{(\mathbf{r} - \mathbf{r}')}{\|\mathbf{r} - \mathbf{r}'\|^3} \cdot \mathbf{n}_l(\mathbf{r}') ds' \quad (3.20)$$

Let us simplify this problem with several approximations. First, we assume that the surfaces S_k are approximated with a set of n triangles $\{T_i \mid i \in [1 \dots n]\}$. The

figure 3.4 shows an example of a triangulated surface. Then, using this triangulation, we can define a subspace of E of finite dimension. For instance, we take the subspace of the piecewise constant functions, which are constant on each triangle. We denote this subspace E_h, where h is an index which stands for the size of the largest triangle. A basis $\{\phi_i\}$ for E_h is :

$$\begin{cases} \phi_i(\mathbf{r}) = 1, & \mathbf{r} \in T_i \\ \phi_i(\mathbf{r}) = 0, & \mathbf{r} \notin T_i \end{cases}$$

Any function $f \in E_h$ can then be written $f = \sum_i f_i \phi_i$, where f_i is the constant value of f on T_i. So if we consider the subspace E_h, we can transform (3.20) in :

Find $V \in E_h$ such that

$$\forall i, \;\; T_i \in S_k, \;\; \frac{\sigma_k + \sigma_{k+1}}{2} V_i = V_0(\mathbf{r}_i) - \frac{1}{4\pi} \sum_l (\sigma_l - \sigma_{l+1}) \sum_{T_j \in S_l} V_j \int_{T_j} \phi_j(\mathbf{r}') \frac{(\mathbf{r}_i - \mathbf{r}')}{\|\mathbf{r}_i - \mathbf{r}'\|^3} \cdot \mathbf{n}_j ds'$$

where $\mathbf{r}_i$ is the center of triangle T_i and $\mathbf{n}_j$ is the constant normal to triangle T_j. This last equation is of the form

$$V_i = b_i + \sum_j a_{ij} V_j \;\; ,$$

where the b_i and a_{ij} are constant coefficients that can be computed. So we just defined a linear system

$$\mathbf{A}\,[V_i] = \mathbf{b} \;\; . \tag{3.21}$$

One just needs to solve this system to get the values V_i of V on each triangle. We are thus able to compute an approximate solution of the electric potential. From this electric potential, an approximate solution of the magnetic field generated by the same source can be computed with equation (3.19) [26].

To ensure the quality of the approximate solution, one has to show that when $h \to 0$ (the triangles get smaller), then the solution in E_h converges to the solution in E. This property is not trivial and depends on the chosen sequence of subspaces E_h. The rate of convergence towards the real solution also depends on the subspaces E_h. For our example, we took the simplest space (piecewise constant functions), but it is usually the space of piecewise linear functions which is chosen [23], which gives a better approximated solution. The quality can be even more increased by using piecewise quadratic or cubic functions, but the increased complexity of the functions also increases the complexity of the coefficients to be computed for building the linear system.

The BEM is prone to certain numerical errors. First, if there are large differences between the conductivities of the different compartments of the head model, it can lead to an amplification of the numerical errors [67]. The Isolated Problem Approach can be used to reduce this effect [40]. Second, for sources which are located close to an interface, typically at a distance smaller than the size of the triangles used to describe the surfaces, the accuracy of the BEM drops severely. A new BEM formulation has been introduced to reduce this effect [55], which also allows to consider piecewise constant conductivity models that are not necessarily nested volumes [56].

Computationally, one advantage of the BEM is that the matrix $\mathbf{A}$ of the linear

system (3.21) is generally sufficiently small to use direct methods for the resolution of the linear system. Such methods use factorizations of the matrix $\mathbf{A}$ (e.g. $\mathbf{A} = \mathbf{LU}$) which transform the linear system (3.21) in a new linear system which can be solved very rapidly. Because the contribution of the source $\mathbf{J}^{\mathrm{p}}$ only appears in the right hand side $\mathbf{b}$ of the system (3.21), the factorization of the matrix (which corresponds to the most computationally expensive part) just has to be performed once for a given head model, and then the solution to the forward problem can be computed rapidly for many different source distributions.

4.3 Beyond piecewise constant models

Even if there is no technique to get a precise 3d image of the conductivity of the head, it is known that some of the head tissues do not have a constant conductivity. For instance, the skull has a variable thickness, and in the areas of large thickness it is composed of soft bone enclosed between two layers of compact bone, and soft and compact bone have different conductivities. Also, the white matter is composed of large bundles of parallel axon fibers which tend to increase the conductivity in the direction parallel to the fibers, so the conductivity is anisotropic with a principal direction which is not constant over space. As a consequence, the BEM can not be used with head models where the conductivity is anisotropic or varies inside the same tissue. For such models, it is necessary to discretize the whole head volume for computing a numerical solution (as opposed to BEM where only the interfaces between tissues are discretized). There are several volume-discretization methods for the numerical solution of PDE : the Finite Element Method (FEM), the Finite Difference Method (FDM), the Finite Volume Method (FVM).

4.4 The Finite Difference Method (FDM)

Finite difference methods approximate the solutions to differential equations by replacing derivative expressions with approximately equivalent difference quotients. For instance, for a function f in 1D, the first order derivative is given by the limit :

$$f'(x) = \lim_{h \to 0} \frac{f(x+h) - f(x)}{h} \ ,$$

and so the derivative can be approximated by :

$$f'(x) \simeq \frac{f(x+h) - f(x)}{h} \ ,$$

for some small value of h. For equation (3.7), we need to approximate the differential operator $\nabla \cdot \sigma \nabla V$, which gives a formula such as :

$$\left(\nabla \cdot \sigma \nabla V\right)(\mathbf{r}_0) \simeq \alpha_0 V(\mathbf{r}_0) - \sum_{i=1}^{6} \alpha_i V(\mathbf{r}_i) \ , \tag{3.22}$$

where

$$\alpha_i = 2h\frac{\sigma_0\sigma_i}{\sigma_0+\sigma_i} \ ,$$
$$\alpha_0 = \sum_{i=1}^{6}\alpha_i \ .$$

The positions $\mathbf{r}_i$ are the points located at a distance of $+h$ and $-h$ of $\mathbf{r}_0$ along each Cartesian coordinate, and σ_i is the conductivity at the point $\mathbf{r}_i$. Actually, this scheme corresponds exactly to Kirchhoff's law for the balance of currents, assuming that the points form a network of resistors. Generally, the head volume is discretized using a cubic grid with a regular spacing h, hence the same scheme (3.22) can be used at every point of the grid with its closest neighbors.

For the source, we need to approximate the divergence operator $\nabla \cdot \mathbf{J}^{\mathrm{p}}$. For a dipole, it is convenient to represent it as a small current between two points $\mathbf{r}^+$ and $\mathbf{r}^-$, so that the divergence is reduced to the source and sink of current, i.e. $\nabla \cdot \mathbf{J}^{\mathrm{p}} = I\delta_{\mathbf{r}^+} - I\delta_{\mathbf{r}^-}$, where I is the strength of the current. This sources and sinks of current can then be plugged directly in Kirchhoff's law, by associating each of them to the closest point of the grid.

Finally we obtain a linear equation for each point $\mathbf{r}_0$ of the grid :

$$\alpha_0 V(\mathbf{r}_0) - \sum_{i=1}^{6}\alpha_i V(\mathbf{r}_i) = \begin{cases} 0 \\ I \\ -I \end{cases} \ .$$

Denoting $\mathbf{V}$ the values of the potential at the points of the grid, we can build a linear system $\mathbf{AV} = \mathbf{b}$, similar to the BEM. The size of the matrix $\mathbf{A}$ is typically bigger than the BEM matrix, because the whole head domain has to be discretized, but it is sparse because it has at most six off-diagonal elements. It is not possible in general to use direct methods for solving this linear system, but iterative methods can perform well because of the sparsity of the matrix $\mathbf{A}$.

Anisotropic conductivities can be handled by the FDM, but in this case the scheme (3.22) has to be modified and typically involves more neighbors [85, 39]. The fact that the FDM uses a regular cubic grid is at the same time an advantage and a drawback. On one hand, the cubic grid and the conductivity values associated to each point of the grid can be directly obtained from the segmentations of the anatomical MRI, which is also represented using a cubic grid. On the other hand, the interfaces between tissues of different conductivities describe smooth and sometimes complex surfaces (e.g. gray-white matter interface) which cannot be accurately represented by the FDM cubic grid (staircase representation).

4.5 The Finite Element Method (FEM)

The FEM is very similar to the BEM in its principle. The difference is that the FEM takes directly the differential equation to solve as an input, whereas for the BEM the differential equation has to be reformulated as a surface integral equation, like (3.18). For instance, the FEM can be used to compute an approximate solution of the differential equation (3.7) for the potential. As a consequence, no assumptions need to be made on the conductivity σ of the domain, and so the FEM can be used

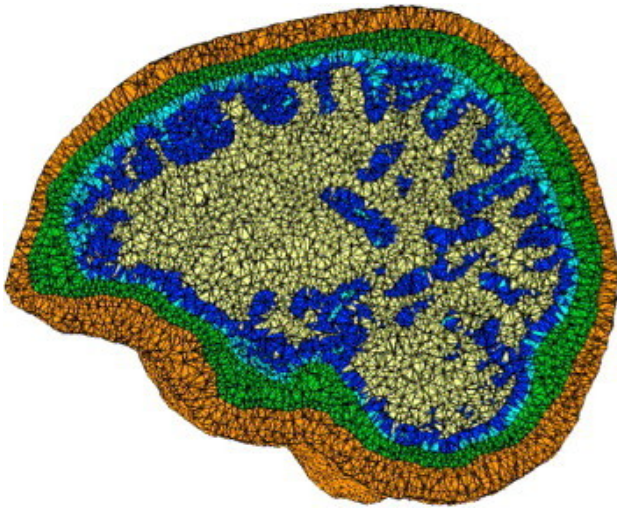

Figure 3.5: A tetrahedral mesh of the head. The different domains are shown with different colors, from inside to outside : white matter, gray matter, CSF, skull, scalp. This picture is taken from [109].

to solve the forward EEG-MEG problem for any conductivity model of the head. We give a sketch of the method here for the electric potential PDE, for further details we refer to the appendix A.

We consider the domain Ω describing the head and its boundary denoted $\partial\Omega$. On the boundary, there is no electric current flowing outside, so the differential equation with its boundary condition is

$$\begin{cases} \nabla \cdot (\sigma \nabla V) = \nabla \cdot \mathbf{J}^{\mathrm{p}} \text{ in } \Omega \\ \sigma \nabla V \cdot \mathbf{n} = 0 \text{ on } \partial\Omega \end{cases} \tag{3.23}$$

An important step of the FEM is to transform the differential equation (3.23) in its variational formulation. We assume that V lives in a certain space E. If V is solution of (3.23), then for any function ϕ of E sufficiently smooth :

$$\begin{aligned} \int_\Omega \nabla \cdot \mathbf{J}^{\mathrm{p}} \phi &= \int_\Omega \nabla \cdot (\sigma \nabla V)\, \phi \\ &= \int_{\partial\Omega} \phi \sigma \nabla V \cdot \mathbf{n} - \int_\Omega \sigma \nabla V \cdot \nabla \phi \\ &= -\int_\Omega \sigma \nabla V \cdot \nabla \phi \end{aligned}$$

The last identity is of the form $a(V, \phi) = f(\phi)$ where a is a bilinear functional and f is linear. The variational formulation of (3.23) is then :

$$\forall \phi \in E, \quad a(V, \phi) = f(\phi) \ . \tag{3.24}$$

It can be shown under certain assumptions on E and a that there is a unique solution V to (3.24) [112], which is hence the solution of (3.23).

Then, like for the BEM, the goal is to rewrite the variational formulation (3.24) in a subspace E_h of finite dimension. This subspace E_h is usually defined from a partition of the domain Ω in tetrahedrons, thus defining a mesh of the head domain and an approximation Ω_h of Ω (figure 3.5). For instance, we can choose E_h to be the space of piecewise linear functions, which are linear in each tetrahedron. The usual

basis for this space is composed of piecewise linear functions each associated to one vertex of the mesh, whose values are one at the corresponding vertex and zero at the others. These functions thus have a local support, which is the polyhedron defined by a mesh vertex and its neighbors. Let us assume that $\{\phi_i \mid i = 1 \dots n\}$ is a basis of E_h, where the index i stands for a mesh vertex. If we look for a solution V in E_h, it can be written $V = \sum_{i=1}^{n} V_i \phi_i$, where V_i is the value of V at the i^{th} vertex. The variational formulation in E_h becomes :

$$\forall j \in [1 \dots n], \quad \sum_{i=1}^{n} V_i a_h(\phi_i, \phi_j) = f_h(\phi_j) \ . \tag{3.25}$$

Once again we built a linear system $\mathbf{A}[V_i] = \mathbf{b}$ which completely determines the values V_i. An approximate solution for the potential can then be obtained by solving this linear system. Once again, because the whole head volume is discretized, the matrix $\mathbf{A}$ is too big to use direct methods for solving the linear system. But due to the local support of the basis functions, the coefficients of the matrix $\mathbf{A}$ given by :

$$a_h(\phi_i, \phi_j) = -\int_{\Omega_h} \sigma \nabla \phi_i \cdot \nabla \phi_j \ ,$$

are non-zero only for basis functions ϕ_i and ϕ_j corresponding to neighboring vertices, hence the matrix $\mathbf{A}$ is very sparse. Iterative methods can thus perform well for solving this linear system.

The right hand side $\mathbf{b}$ of the system is given by :

$$\begin{aligned} f_h(\phi_j) &= \int_{\Omega_h} \nabla \cdot \mathbf{J}^{\mathrm{p}} \phi_j \\ &= \int_{\partial\Omega_h} \phi_j \mathbf{J}^{\mathrm{p}} \cdot \mathbf{n} - \int_{\Omega_h} \mathbf{J}^{\mathrm{p}} \cdot \nabla \phi_j \\ &= -\int_{\Omega_h} \mathbf{J}^{\mathrm{p}} \cdot \nabla \phi_j \ , \end{aligned}$$

assuming that there are no sources on the boundary $\partial\Omega_h$ and that partial integration is possible. But this formulation can be generalized to $\mathbf{J}^{\mathrm{p}}$ being a distribution, in what case $\int_{\Omega_h} \nabla \cdot \mathbf{J}^{\mathrm{p}} \phi_j = -\int_{\Omega_h} \mathbf{J}^{\mathrm{p}} \cdot \nabla \phi_j$ by definition. For instance, for a dipole, $\mathbf{J}^{\mathrm{p}} = \mathbf{q}\delta_{\mathbf{r}_0}$, where $\delta_{\mathbf{r}_0}$ is the Dirac distribution at $\mathbf{r}_0$, we thus have :

$$f_h(\phi_j) = \mathbf{q} \cdot \nabla \phi_j(\mathbf{r}_0) \ .$$

As a consequence, the contribution of the dipole in the right hand side $\mathbf{b}$ is non-zero at all neighboring nodes of the dipole position $\mathbf{r}_0$. The dipole is hence represented by a linear combination of several basis functions, and so this specific finite element representation of the dipole is "blurred". Other representations of the dipole for the FEM are possible [91].

The incorporation of anisotropic conductivity in the FEM is straightforward. If the conductivity is described as a tensor Σ, then the coefficients of the matrix $\mathbf{A}$ are :

$$a_h(\phi_i, \phi_j) = -\int_{\Omega_h} \nabla \phi_i \cdot \Sigma \nabla \phi_j \ .$$

The advantage of the FEM compared to the FDM is that the head volume can be discretized using an unstructured grid, such as a tetrahedral mesh. As a consequence, the FEM mesh can better represent the complex surfaces that correspond to the interfaces between tissues. Nevertheless, the generation of such meshes is not

trivial and requires additional work. The meshing can be simplified by using hexahedral cells, but in this case the surfaces are described by staircase shapes which decrease the quality of the approximation. One solution to limit this effect is to use geometry-adapted hexahedral cells [111].

5 RECIPROCITY

In classical electromagnetism, reciprocity refers to a variety of related theorems involving the interchange of electric current densities (sources) and the resulting electromagnetic fields (measurements). The most general theorem is Lorentz reciprocity, which basically states that the relationship between a current and the resulting electric field is unchanged if one interchanges the points where the current is placed and where the field is measured. This result was obtained by Lorentz following analogous results regarding sound by Helmholtz, and the theorem is also often referred to as Helmholtz reciprocity. This concept of reciprocity can also be applied for the forward problem in EEG and MEG [84, 64].

Let us consider a bounded conductor : a current dipole is placed in the conductor at position $\mathbf{r}_0$ with moment $\mathbf{q}$, and the resulting electric potential V is measured at two positions $\mathbf{r}_1$ and $\mathbf{r}_2$ located on the boundary of the conductor. The reciprocal configuration is to consider that a current I is injected in the conductor between the two positions $\mathbf{r}_1$ and $\mathbf{r}_2$ and that the resulting electric potential U is measured at the position $\mathbf{r}_0$. In this case, the reciprocity theorem states that :

$$V(\mathbf{r}_1) - V(\mathbf{r}_2) = \frac{\nabla U(\mathbf{r}_0) \cdot \mathbf{q}}{I} \quad .$$

As a consequence, the knowledge of U in the whole conductor can give the value of the measurement $V(\mathbf{r}_1) - V(\mathbf{r}_2)$ for any dipole placed in the conductor.

Let us consider now that one needs to generate a gain matrix for an EEG with 64 sensors and for a distributed source model with 10000 dipoles. Such a matrix thus has 64 rows and 10000 columns. The direct method to generate the gain matrix is to compute the electric potential V generated by each dipole and to sample its values at the EEG sensors. This requires to solve the forward problem for 10000 different source configurations. If instead we consider a pair of EEG electrodes, we can compute the electric potential U generated by a current injection between these electrodes and sample ∇U at the dipole positions to get a complete row of the gain matrix. Using this approach, the gain matrix generation only requires to solve the forward problem for 64 different source configurations.

This reciprocal approach is particularly interesting when solving the forward problem for many different source configurations is computationally expensive. This is not very interesting with spherical models because the analytical formulas can be computed very rapidly. With numerical methods (BEM,FDM,FEM), one has to solve a linear system $\mathbf{AV} = \mathbf{b}$, where the contribution of the source appears in the right hand side $\mathbf{b}$. In the case of the BEM, direct methods can be used : the matrix $\mathbf{A}$ is factorized and then the linear system can be solved rapidly for different right hand sides, so the reciprocal approach is not necessary. For FDM and FEM, the matrix $\mathbf{A}$ is too big to be factorized, and the linear system is solved by iterative methods. On

the contrary of direct methods, the iterative methods can not take advantage of a linear system where only the right hand side changes. Any iterative solver has to be restarted for each new right hand side b. As a consequence, the computational time with FDM or FEM is directly proportional to the number of source configurations, and in this case the reciprocal approach is very useful.

6 CONDUCTIVITY

For all the forward models, from the simplest ones to the most complex, one has to choose what conductivity values are assigned to the model. In MEG, most people use a spherical model which does not depend on the conductivity, so in this case the problem is avoided. Even when using a realistic model, the choice of conductivities is not crucial for MEG [41]. For EEG, the conductivities of the head model have a non negligible effect on the propagation of the electric potential, and thus their values must be chosen in aim to reproduce as well as possible the real electric potential propagation.

The electrical conductivities of many human tissues have been measured *in vitro* and are available in the literature [29, 30]. Some tissues have also been measured invasively for animals [60, 113] and for humans [6, 57]. But these measured values are not necessarily the best values to put in the forward model. First, the skull is a very variable tissue depending on the person and the age, and so its electrical conductivity can not be tabulated once and for everybody. Second, the forward model gives an approximation of the real conductivity distribution of the head, and so the conductivity parameters for which the forward model best reproduces reality are not necessarily the physiological conductivity values. For instance, when using a classical three-layer model of the head (brain, skull, scalp), many types of tissues are omitted, but the approximation error of the model can be compensated for if one chooses ”efficient” conductivity values instead of physiological values. The efficient conductivities would be the values for which a given model best reproduces the real propagation of the electric potential.

These remarks show the need for methods for *in vivo* calibration of the forward model conductivities, which can be used non-invasively for each subject of an EEG experiment. The classical technique for the in vivo conductivity estimation of the head tissues is to inject a current at the scalp surface and to infer the conductivity values from the resulting potential measurements at the scalp surface. This is called Electrical Impedance Tomography (EIT). The applicability of this technique has been shown for three-layer models [78, 102, 37]. Another possible approach is to consider a focal brain activity recorded with a combination of EEG and MEG measurements [37, 7, 38]. In this case, the brain source is estimated with MEG, and then fixed in the forward model which allows to estimate the conductivities from the EEG measurements. Both these approaches suffer from the ill-conditioning of the inverse conductivity problem : one tries to estimate a conductivity distribution in the 3d space of the head with only boundary data given by the EEG measurements. Actually, these approaches are applicable only when the conductivity models are parametrized with few parameters, thus no regularization is needed. A recent technique called Magnetic Resonance Electrical Impedance Tomography (MREIT)

aims to bypass this limitation : it uses a MRI scanner to measure the magnetic field generated by a current injection on the scalp [76]. In this case, the data is measured not only at the boundary but in the whole head volume, and so a 3d image of the conductivity can be estimated.

Part I

Forward problem computation

CHAPTER 4

IMPLICIT MESHES FOR FEM

Finite Element methods (FEM) usually require a mesh to describe the geometric domain in which the computations occur. These meshes must have several properties: 1) they must approximate the geometrical domain accurately, 2) they must have good numerical properties, and 3) they must be small enough so that the computations take a reasonable amount of time. These goals are somewhat contradictory and in many cases such as biomedical images – and particularly in the case of the head –, even though the geometric domains can effectively be extracted, e.g. from Magnetic Resonance Images (MRI), the generation of such meshes can in certain cases be difficult.

This chapter describes a technique that bypasses this mesh generation step going directly from a description by levelsets of the interfaces separating the various domains to the matrix associated to the FEM method. Using the levelsets description is quite convenient as it is already used by many segmentation tools.

Contents

1 INTRODUCTION

MRI segmentation techniques have been developed for several years now, and many toolboxes are available for (more or less) automatic extraction of the different subdomains of the head [19, 16, 94]. The classical output of these segmentation methods is a set of surfaces describing the interfaces between different tissues. To use these surfaces with FEM methods, they must be meshed with certain quality criteria :

- The meshes obtained from various surfaces should not self-intersect.
- The meshes should have a controlled size while preserving their topological and geometrical quality.
- Volumes delimited by various meshes need to be meshed and fused in a single volumic mesh again with a controlled quality and size.

For these reasons, the problem of creating a volumic mesh from a set of surfaces is a difficult one, often involving the use of many different tools and some hand polishing to get a proper result. This can be very time consuming and an obstacle to a more widespread use of FEM methods, especially when new meshes need to be created often, such as in the medical field where each patient is different.

This is all the more disturbing that the meshes are used only to discretize a variational criterion and its solution, which then takes the form of a linear system: $\mathbf{AV} = \mathbf{B}$, where $\mathbf{A}$ is a sparse matrix called the *stiffness matrix*, $\mathbf{V}$ is the discretized approximation of the solution and $\mathbf{B}$ is the discretized approximation of the input data. Computing $\mathbf{A}$ and $\mathbf{B}$ just requires a discretization Ω_h of the space Ω on which the computation has to be made and a basis $\mathcal{B}$ for a discrete approximation of the space $\mathcal{F}$ of sufficiently regular functions defined on Ω. The most standard choice is to use tetrahedral meshes for Ω_h and piecewise linear functions over the mesh (P1 elements) to approximate $\mathcal{F}$. In this case, the basis $\mathcal{B}$ is defined as the set of piecewise linear functions that take the value 1 on one nodal point of the mesh and zero on the other nodes.

Here we use another family : Q1 elements. The reason is that the pixels (voxels) of a MRI image readily provide a Cartesian mesh and the standard Q1 function basis is exactly the one used with multi-linear interpolation in images. This is thus an attractive choice to avoid the generation of a complicated mesh. But in this case, the mesh does not give a description of the interfaces between tissues. We hence use the levelset representation to keep track of these surfaces in the FEM method. The remaining of this chapter studies how to build the matrices $\mathbf{A}$ and $\mathbf{B}$ directly from levelsets and using Q1 elements, in the 2D and 3D cases.

2 Q1 ELEMENTS

Consider a rectangular domain B of the embedding space in which the calculations have to be made. In order to solve the equations of interest over B, usually this

Coordinate system	$\mathbf{x} = [x\,y]^T$	$\mathbf{x} = [x\,y\,z]^T$
Cell shape	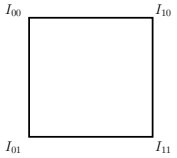	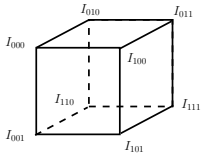
	$\rho_i(u) = \begin{cases} 1-u & \text{if} \quad i=0 \\ u & \text{if} \quad i=1 \end{cases}$	
Basis functions	$\phi_{ij}(\mathbf{x}) = \rho_i(x)\rho_j(y)$	$\phi_{ijk}(\mathbf{x}) = \rho_i(x)\rho_j(y)\rho_k(z)$
Shape of a function	$f(x,y) = \sum_{i=0}^{1}\sum_{j=0}^{1} I_{ij}\phi_{ij}(\mathbf{x})$	$f(x,y,z) = \sum_{i=0}^{1}\sum_{j=0}^{1}\sum_{k=0}^{1} I_{ijk}\phi_{ijk}(\mathbf{x})$

Figure 4.1: Summary of the Q1 elements and basis functions in the 2D and 3D cases. The values I_{ij} and I_{ijk} are the values of a function f at the nodes of a cell. The third line gives the basis functions ϕ_n attached to the node n where n is a multi-index.

domain has first to be tessellated in order to approximate the solution in the continuous domain by one in a finite dimensional space. In this work, a regular Cartesian grid G_h is used, where h is the "step" of the grid. For simplicity, it is assumed hereafter that the step is 1 in all dimensions. Obviously, the general case derives from this simple one by an appropriate rescaling of the domain. The N nodes of this grid are denoted by $\mathbf{P}_i$, where i is a multi-index (a vector of integer indices of the appropriate dimension). The elements of this grid are squares (in 2D) or cubes (in 3D) and are denoted by $S_j, j = 1..P$. In Q1 finite element methods, a continuous function f over B is approximated by a piecewise multilinear continuous function f_h by:

$$f_h(\mathbf{x}) = \sum_n f(\mathbf{P}_n)\phi_n(\mathbf{x}) \ .$$

The function ϕ_n is a piecewise multilinear function defined by:

$$\phi_n(\mathbf{P}_k) = \begin{cases} 1 & k = n \\ 0 & otherwise \end{cases} \tag{4.1}$$

When h tends to 0, f_h tends to f. Obviously, the set of values $f(\mathbf{P}_n)$ represents an image and f_h corresponds to the classical multilinear interpolation in images. From Eq. 4.1 and because the grid G_h is Cartesian, it can be seen that, except at the borders, all the functions ϕ_n can be obtained by translating at position $\mathbf{P}_n$ a standard function centered at the origin of the space $\phi_n(\mathbf{x}) = \phi(\mathbf{x} - \mathbf{P}_n)$. In particular, ϕ can be depicted by its restrictions over the various cells surrounding the origin or equivalently by the various non-null restrictions of ϕ_n to a given cell. Fig 4.1 summarizes

the properties of Q1 elements in the 2D and 3D cases.

3 LEVELSETS

Let us first recall briefly what levelsets are. The levelsets technique was first hinted to in [25] and then developed by Osher and Sethian [79]. Since then it has received a lot of attention for representing and evolving closed shapes in space. The basic idea of levelsets is to represent a surface $\mathcal{S}$ of codimension 1 (a curve in 2D or a surface in 3D) implicitly as the zero-level of a scalar function $f_{\mathcal{S}}$ in its embedding space (e.g. $\mathbb{R}^2$ for curves or $\mathbb{R}^3$ for surfaces). Typically, this function f represents the signed distance to the surface (negative inside, positive outside). In practice, the embedding space is tessellated with a square grid (squares in 2D, cubes in 3D) and $f_{\mathcal{S}}$ is discretized as a 2D or 3D image. One key of the success of the levelset method is that complex shapes can be easily and conveniently manipulated as images. In this work, we adopt a multilinear interpolation of the levelset images, i.e. a representation with Q1 elements. This allows for two things:

- The zero crossings within a pixel/voxel are well defined as the zero-crossings of the multi-linear function.
- Consequently, the topology of the levelset is always well defined.

Hence we can represent the head geometry with Q1 levelsets. We denote by $\mathcal{B}$ the bounding box of the head domain and assume that this domain can be depicted as a finite set of subdomains $\mathcal{D}_i, i = 1..N$ delimited by closed non-intersecting interfaces $\mathcal{S}_j, j = 1..M, \mathcal{S}_j \cap \mathcal{S}_k = \emptyset$ if $j \neq k$. Denoting by $\mathcal{I}$ a tessellation of $\mathcal{B}$, each interface $\mathcal{S}_j$ is represented by a levelset as an image.

For simplicity, it is assumed in the following that there is at most one interface crossing any pixel/voxel of $\mathcal{I}$. This is just a technical requirement that can easily be overcome. Many tools have been proposed to obtain such levelset descriptions of complex domains [115, 36, 35, 44, 43, 93].

4 COMPUTING THE FEM INTEGRALS

Usually, with FEM methods, the domain where the PDE is solved is modeled as a set of subdomains for which the PDE coefficients (e.g. the conductivity) are constants. As explained in appendix A, section 3 for the electric potential PDE, the assembly of the stiffness matrix $\mathbf{A}$ requires to compute integrals involving the elements and the conductivity. For instance, the classical tetrahedral mesh with P1 elements leads to the following coefficients for $\mathbf{A}$:

$$A_{ij} = \sum_{k:\mathbf{P}_i \in T_k, \mathbf{P}_j \in T_k} \int_{T_k} \sigma_k \nabla \phi_k^i(\mathbf{r}) \cdot \nabla \phi_k^j(\mathbf{r}) \, d\mathbf{r} \ ,$$

where T_k denotes a tetrahedron and σ_k is the constant value of the conductivity over this tetrahedron. As a consequence, the tetrahedral mesh must match the different

subdomains to allow the use of a constant σ_k in the tetrahedron T_k. Designing such a mesh can be a complicated task as explained in the introduction.

In this work, we use the FEM method with a Cartesian mesh and basis functions which are Q1 elements, so the A_{ij} are now integrals on voxels V_k.

$$A_{ij} = \sum_{k:\mathbf{P}_i \in V_k, \mathbf{P}_j \in V_k} \int_{V_k} \sigma(\mathbf{r}) \nabla \phi_k^i(\mathbf{r}) \cdot \nabla \phi_k^j(\mathbf{r}) \, d\mathbf{r} \ .$$

The Cartesian mesh does not match the geometry of the subdomains, and the conductivity σ is not necessarily constant on a voxel V_k. If a given voxel V_k crosses an interface, we can not use a constant σ in the whole voxel, but we can split V_k in its two subdomains V_k^1 and V_k^2 where σ is constant :

$$\int_{V_k} \sigma(\mathbf{r}) \nabla \phi_k^i(\mathbf{r}) \cdot \nabla \phi_k^j(\mathbf{r}) \, d\mathbf{r} = \int_{V_k^1} \sigma_k^1 \nabla \phi_k^i(\mathbf{r}) \cdot \nabla \phi_k^j(\mathbf{r}) \, d\mathbf{r} + \int_{V_k^2} \sigma_k^2 \nabla \phi_k^i(\mathbf{r}) \cdot \nabla \phi_k^j(\mathbf{r}) \, d\mathbf{r} \ .$$

The levelset of the interface between the two subdomains gives a parametrization of the surface which allows to properly define the integrals on the subdomains V_k^1 and V_k^2. This is detailed in section 5.

5 COMPUTING INTEGRALS ON THE DOMAINS DEFINED BY LEVELSETS

With the choice of Q1 elements, the integrals that have to be computed for our applications (MEEG) are of the form :

$$\int_{V_k^1} \nabla \phi_m(\mathbf{r}) \cdot \Sigma \nabla \phi_n(\mathbf{r}) \, d\mathbf{r} \ ,$$

where Σ is a constant conductivity tensor which can represent an anisotropic conductivity. To be able to take Σ out of the integral, we need to compute the integrals of all the possible products of the different components of the basis function gradients :

$$\int_{V_k^1} \partial_i \phi_m(\mathbf{r}) \partial_j \phi_n(\mathbf{r}) d\mathbf{r} \qquad (i,j) \in \{x,y,z\}^2.$$

Because the basis functions ϕ_n are trilinear on the voxel V_k, the polynomial corresponding to $\partial_i \phi_m \partial_j \phi_n$ can be composed of 23 different monomials, where the highest degree monomials are $x^2y^2, x^2z^2, y^2z^2, x^2yz, xy^2z, xyz^2$. Hence in the following we just describe, for these kind of monomials, how to compute the integral on a subdomain V_k^1 of V_k. The integral of the polynomial $\partial_i \phi_k \partial_j \phi_l$ is obtained by linear combination of the integrals of the different monomials. The next two sections describe the monomial integrations in the 2D and 3D cases.

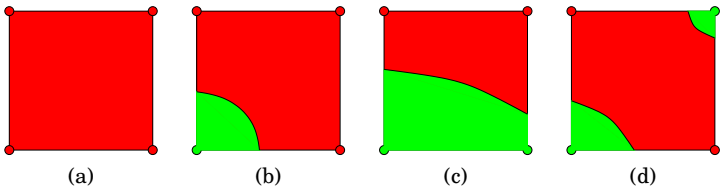

Figure 4.2: The basic four cases that can arise in the integral computation. The red and green colors correspond to levelset values of different signs (exactly which sign is not meaningful). The black curve corresponds to the zero-crossing, while the red and green areas correspond to the two separate domains on which the integrals must be computed. The horizontal and vertical axes corresponds to the variables x and y respectively.

5.1 Computing the monomial integrals in the 2D case.

In the 2D case, the restriction to each voxel of a Q1 levelset takes the form:

$$f(x,y) = c_{00}xy + c_{10}x + c_{01}y + c_{00} \ .$$

For a pixel that crosses the interface, it is easy to parameterize the curve corresponding to the zero crossing as $(x, -\frac{c_{10}x+c_{00}}{c_{11}x+c_{01}})$ for some range of values of x. After normalization by symmetry and rotation, there are basically four cases that can occur. Those correspond to different topological configurations and are shown in Fig. 4.2. Case (a) is trivial with integrals over the green domain being 0 and integral over the red domain being easily computed. Case (b) is the basic one : the green domain is defined by $Green = \left\{(x,y)/x \in [0,x_0], y \in [0, -\frac{c_{10}x+c_{00}}{c_{11}x+c_{01}}]\right\}$, where x_0 is the intersection of the zero-crossing of the curve with the x-axis. Cases (c)-(d) are just variants of case (b):

- Case (c) is the same as case (b) with a range over the horizontal axis of $[0,1]$ (i.e. $x_0 = 1$).
- Case (d) is just the sum of two cases of type (b), one in the configuration shown and one with the same configuration but rotated by $180°$.

Let us assume that the monomial integrand is $m(\mathbf{x}) = m(x,y)$ and that $M(x,y)$ is the primitive of $m(x,y)$ defined by:

$$M(x,y) = \int_0^y m(x,u)du \ .$$

Since m is a monomial, M is also a monomial in x and y. We also assume that integrals over the green domain need to be computed (the integrals over the red domain are simply the integrals over the full pixel minus the green integrals). The integrals can then be computed as:

$$\begin{aligned} \int\int_{Green} m(x,y)dydx &= \int_0^{x_0} \int_0^{-\frac{c_{10}x+c_{00}}{c_{11}x+c_{01}}} m(x,y)\ dydx \\ &= \int_0^{x_0} M\left(x, -\frac{c_{10}x+c_{00}}{c_{11}x+c_{01}}\right) dx \ . \end{aligned}$$

Since M is a monomial, this is just the integral of a rational function that can be calculated explicitly and implemented using simple rational functions and logarithms[1]. There are, however, two important points to take into account for the implementation :

- The argument of the logarithm that appears in the formulae (all monomial involve the same value) can be zero when $top = c_{11}c_{00} - c_{10}c_{01} = 0$. This is related to a topological change of the zero-crossing of the levelset and corresponds to the case where $f(x, y) = (ax + b)(cy + d)$ for some values of a, b, c, d. In such a case (and for all situations where top is small), the explicit expressions need to be replaced by their limit when top tends to 0 which are polynomials that can be obtained explicitly.

- If $c_{11} = 0$, the integrals are even simpler to compute as the rational function becomes a simple affine one. However, when c_{11} is close to zero the explicit formulae are poorly conditioned numerically (especially when the monomial degree increases). As an example, for the integral corresponding to the monomial x^2y^2 all the first six terms of the Taylor expansion cancel. For this reason, it is better to rely on the first non-zero terms of the Taylor expansion to estimate the integral values for small values of c_{11}. In practice, 20 terms of the Taylor expansion have been used.

The full algorithm is then the following:

1. Using rotations, symmetry and change of sign of the levelset, normalize the given element to be one of Fig 4.2.

2. Compute the value of x_0 according to the case: $x_0 = -\frac{c_{00}}{c_{10}}$ for cases (b) and (d) and $x_0 = 1$ for case (c).

3. Compute the various integrals using the explicit formulae.

4. For case (d), apply a 180° degree rotation over the element, compute the integral values as in step 2 and 3, apply the transforms needed to bring these values back into the original space (simple linear combinations of the various computed integrals in general) and add those values to the ones computed at step 3.

5. Compute the values corresponding to the integrals in the original configuration (i.e. before using rotations and symmetries of step 1). Again, these are normally simple linear combinations of the values computed at step 4.

6. Assemble the monomials into the polynomials of interest.

5.2 Computing the monomial integrals in the 3D case.

Because the 2D integrals already involve logarithms, there is little hope of obtaining explicit formulae for monomial integrals in the 3D case. This is all the more true as the number of topological situations is much bigger (see e.g. [14, 62] for an explicit study of these configurations in the Q1 case). The problem was thus solved using

[1]Explicitly giving all the formulae would be tedious, error prone and not very interesting. A maple function that computes the relevant elements was used.

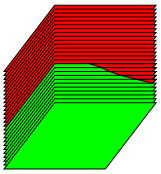

Figure 4.3: A voxel is sliced along the vertical axis. For each slice, 2D integrals can be computed explicitly. The 3D integrals are then obtained using numerical integration.

numerical integration. As depicted in Fig. 4.3, the 3D voxel is considered as a 1D family of 2D squares piled up along the z-axis. For each square, the monomial integrals can be computed using the method depicted in Sect. 5.1 and a Gauss-Kronod numerical integration method with 61 points is used to integrate those values along the z-axis. Care has to be taken to split the z-axis $[0, 1]$ into pieces for which the 2D slices share the same topology (otherwise some inaccuracies may occur). Since topology changes are related to changes of signs on the corners of the 2D slice, and since Q1 elements have been used (so that the levelset function varies linearly along the z-axis), there are at most four such changes along the z axis (one for each corner of the 2D slices).

6 RESULTS

The previous formalism is used here with a synthetic problem and an application to EEG forward computation. In the first section, it is simply used to estimate the simplest possible integral : a volume. Spheres are used in order to have a known ground truth. The second section applies the formalism to one of our target application : EEG forward problem computation. This is done first on a spherical model for which the ground truth is known and then for a realistic head model.

6.1 Volume of spheres

Volumes are naturally the simplest integral that can be estimated. Here spheres have been used so that the ground truth is known. Basically, we used a levelset describing a sphere, and we computed the integral of the constant monomial 1 on all the voxels (and subdomains of voxels) which are inside the levelset. The volume is then obtained by summing all the integrals. Figure 4.4a shows the accuracy of the proposed technique. Even with a coarse grid, the computed volume is very accurate.

We also did the same experiment but this time by computing the integrals of all the monomials described in section 5 that are needed for the FEM applied to the EEG forward problem. The figure 4.4b shows that the computational time needed to compute all the monomial integrals is proportional to the area of the interface (the sphere in this case). This is due to the fact that the integrals on voxels completely inside the levelset are all identical, and have to be computed just once. It also means that the memory storage of these integrals is proportional to the area. This is an advantage compared to tetrahedral meshes for which each tetrahedron has its own geometry, and thus the integrals are all different, so in this case the computational

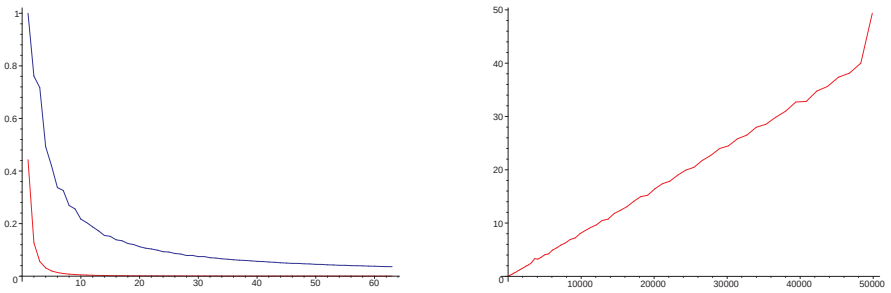

(a) (b)

Figure 4.4: The relative accuracy of the volume of the sphere (left). The horizontal axis gives the radius of the sphere (the unit is the voxel size). The vertical one gives the relative error of the computed volume. The red curve corresponds to the proposed technique whereas the blue one gives the value obtained by a simple counting of the inner voxels. The right plot gives the computational times of all the monomials with respect to the sphere area (horizontal axis).

time and the memory storage are proportional to the volume.

6.2 EEG Forward Problem

6.2.1 Spherical Model.

The accuracy is first evaluated by computing the electric potential on a 3-sphere model with a single dipolar source. In this configuration, there is an analytic expression of the potential which can be used as a ground truth to estimate the error of the method [118]. The dipolar source is approximated in the FEM using the formula (A.6) (appendix A, section sect:FEM discretized). The spherical model is composed of 3 spheres of radii 0.87, 0.92, 1. The conductivity values are 0.33, 0.0042, 0.33 from inside to outside for the isotropic case, and the conductivity of the middle layer (corresponding to the skull) is 0.008 in the tangential direction and 0.0008 in the radial direction for the anisotropic case. The accuracy of the numerical solution is given by the Relative Difference Measure (RDM) on the outermost sphere (uniformly sampled with 642 points) :

$$RDM = \left\| \frac{V_{num}}{\|V_{num}\|} - \frac{V_{anal}}{\|V_{anal}\|} \right\|$$

where V_{num} is the numerical solution, V_{anal} is the analytic solution and $\|\cdot\|$ is the discrete l^2-norm. Figure 4.5 shows the RDM with respect to the eccentricity of the dipole. The dipole eccentricity increases in z direction, and the dipole orientation is always $(1, 0, 1)$, which encompasses both radial and tangential orientations. As expected, the error increases when the dipole gets closer to the innermost sphere, but the RDM stays below 4% with a good resolution ($256 \times 256 \times 256$).

The computational cost of the method was also compared to the classical tetrahedral mesh FEM. Table 4.1 illustrates the computation time of both FEM approaches. For the same discretization (equivalent number of points), the computational cost of the proposed method is smaller, both in memory and time.

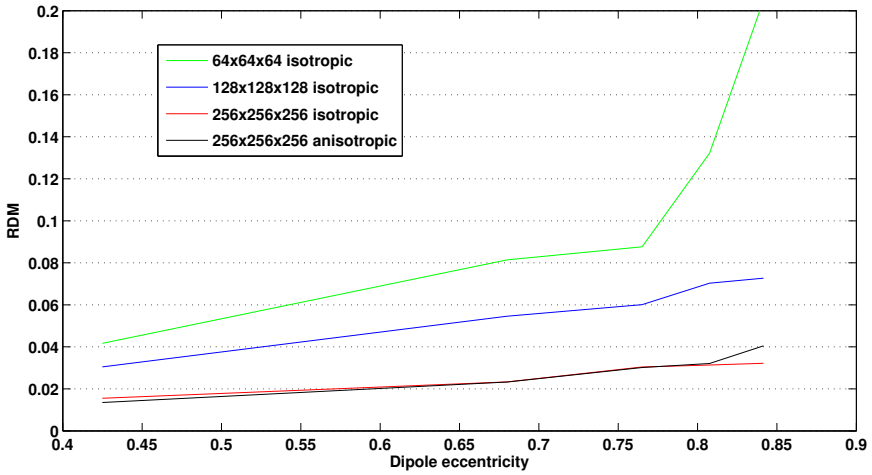

Figure 4.5: Accuracy of the forward EEG computations with respect to the eccentricity of the source (horizontal axis) and the size of the discretization. The vertical axis represents the relative error.

	Number of points	Edge size	Assembly time	Memory space	Solving time
Tetrahedral	1e6	0.018	2mn45s	1GB	1h07mn
Implicit 128x128x128	1e6	0.016	3mn17s	140MB	8mn
Implicit 256x256x256	8e6	0.008	13mn51s	1.2GB	1h38mn

Table 4.1: The computational performances of the method are compared to tetrahedral FEM. For similar discretizations, the memory cost is smaller, leading to a smaller computation time of the solution. As a consequence, the method can handle higher resolutions.

We also applied our approach to the computation of the magnetic field, the results are shown in chapter 5.

6.2.2 Real Head Model.

To model a real head, an MRI image of size $256 \times 256 \times 256$ has been taken and segmented using four levelsets (also within a $256 \times 256 \times 256$ discretized domain). Figure 4.6 (a) shows a cut through this model. Figure 4.6 (b) shows the computed potential over the skin. For this model constant conductivities have been used for each of the five sub-domains. Building such a model using standard meshing techniques would require a lot of work and would result in a huge mesh of several millions tetrahedra whereas the matrix computed by the proposed technique has been computed in about 12 minutes (on a 2GHz laptop). With the classical tetrahedral technique, a standard meshed model with a similar accuracy could not have been run on such a laptop.

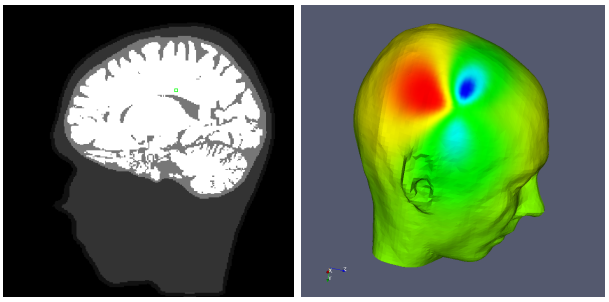

(a) (b)

Figure 4.6: EEG computation on a real head model. Left: the five layers model used to compute the solution. From the outside to the inside, this model contains the air (black), the skin, the skull, the cerebro-spinal fluid and the brain (white). Notice how complex is the brain. To model this using standard meshing techniques would require a huge number of tetrahedra and a lot of user interaction to build the model. Right: the potential value displayed on the skin for a given source in the brain.

7 CONCLUSION

It is possible to compute the FEM matrices directly from levelsets-based segmentations. For complicated domains that need to be generated on a regular basis (such as head models), this technique has many practical advantages. First, the technique needs no user interaction for mesh generation. Second, the time needed to produce and solve the FEM linear system is typically decreased by an order of magnitude for complex models such as the head. This time is directly proportional to the total area of the interfaces used in the model. It allows for production of very accurate models (at the resolution of the MR images that are the support for the levelsets) at moderate and known a priori costs. Further benefits can be obtained thanks to the regular discretization structure. Many parts of the FEM code were easily parallelized using OpenMP, what can be very effective with the democratization of multi-core CPUs. Using multiscale techniques is also possible. The main drawback of the technique compared to tetrahedral FEM is that less control of the solution at the interfaces is possible.

Because our FEM approach uses a cubic grid as a mesh, it is somehow similar to a FDM method. The main theoretical advantage of the FEM compared to FDM is the quality of the approximation between grid points. Nevertheless, the qualities of both approaches are problem dependent : in general, FEM is more used for structural mechanics whereas FDM is more used for fluid dynamics. In the case of EEG/MEG forward problem computation, numerical comparisons between both approaches would be necessary.

CHAPTER 5

THE ADJOINT METHOD FOR GENERAL EEG AND MEG SENSOR-BASED LEAD FIELD EQUATIONS

Most of the methods for the inverse source problem in electroencephalography (EEG) and magnetoencephalography (MEG) use a lead field as an input. The lead field is the function which relates any source in the brain to its contribution to the measurements at the sensors. For complex geometries, there is no analytical formula of the lead field. The common approach is to numerically compute the value of the lead field for a finite number of point sources (dipoles). There are several drawbacks : the model of the source space is fixed (a set of dipoles) and the computation can be expensive for as much as 10000 dipoles. The common idea to bypass these problems is to compute the lead field from a sensor point of view, by using reciprocal approaches. In this chapter, we use the adjoint method to derive general EEG and MEG sensor-based lead field equations. Within a simple framework, we provide a complete review of the explicit lead field equations, and we are able to extend these equations to non-pointlike sensors. The work presented in this chapter was submitted to the journal *Physics in Medicine and Biology*.

Contents

1 INTRODUCTION

Electroencephalography (EEG) and magnetoencephalography (MEG) can be used as functional brain imaging modalities : in this case, the goal is to localize the electrical activity in the cortex from the EEG or MEG measurements. This is referred to as the inverse source problem. Before solving the inverse source problem, one needs a forward model which gives the electric potential or magnetic field for a known source configuration. In EEG for instance, the forward problem is given by the following differential equation :

$$\begin{cases} \nabla \cdot (\sigma \nabla V) = \nabla \cdot \mathbf{J}^{\mathrm{p}} & in \quad \Omega \\ \sigma \nabla V \cdot \mathbf{n} = 0 & on \quad \partial\Omega \end{cases} \tag{5.1}$$

where V is the electric potential, σ is the conductivity, $\mathbf{J}^{\mathrm{p}}$ is the primary current vector (representing brain electrical activity) and Ω is the head domain. It is obvious that V is linear with respect to $\mathbf{J}^{\mathrm{p}}$, and so the mapping of $\mathbf{J}^{\mathrm{p}}$ on the EEG electrodes can be represented by a linear operator L which is called the lead field. Many methods for solving the inverse source problem use the lead field representation, and most of the time the lead field is discretized for a finite number of dipoles with unitary moments. The result is the so-called lead field matrix $\mathbf{L}$: one column of the matrix gives the values of the electric potential at the EEG electrodes for a given dipole. This matrix has a number of lines equal to the number of electrodes and a number of columns equal to the number of dipoles considered (around 10000 in distributed source models). Then the EEG measurements are simply given by the matrix-vector product $\mathbf{m} = \mathbf{L}\mathrm{s}$ where s is a vector containing the amplitudes of the dipoles, which becomes the unknown of the inverse problem.

To compute the matrix $\mathbf{L}$, the direct method is to solve (5.1) for each dipole. If the head is modeled as spherical shells, then there is an analytic formula for the solution of (5.1), and the computation of $\mathbf{L}$ is very fast. For realistic geometries, there are different approaches, such as the finite difference method (FDM), the boundary element method (BEM) or the finite element method (FEM). They are different ways of discretizing the differential equation (5.1), and they all lead to solving a linear system of finite dimension

$$\mathbf{A}\mathbf{x} = \mathbf{b} \ . \tag{5.2}$$

The matrix $\mathbf{A}$ is constant for given geometry and conductivities, and the right-hand side $\mathbf{b}$ is determined by the source, so it is different for each dipole. For the BEM, the matrix $\mathbf{A}$ is sufficiently small to be able to factorize it ($\mathbf{LU}$ for instance), and once factorized, it is fast to solve the linear system (5.2) for many different right-hand sides $\mathbf{b}$. But the BEM only allows to describe the conductivity of the head domain as piecewise constant and isotropic. On the contrary, FDM and FEM allow to describe general conductivity distributions, but the matrix $\mathbf{A}$ generated is generally too big to use direct factorizations. In this case, the system (5.2) is solved by iterative methods, and this can be extremely time consuming if it has to be done for as many as 10000 different right-hand sides.

A first approach to bypass this problem is to do matrix manipulations on (5.2) to get a new system

$$\mathbf{A}^T\mathbf{y} = \mathbf{c} \tag{5.3}$$

with the matrix $\mathbf{A}^T$, which is equal to $\mathbf{A}$ since $\mathbf{A}$ is generally symmetric. In this case the number of different right-hand sides $\mathbf{c}$ is equal to the number of sensors (around 60 for EEG electrodes), which considerably reduces the computation time. This so-called transfer matrix approach is described for the EEG in [105] and for the EEG and MEG in [105, 110]. In this approach, (5.3) was directly created from the discretized equation (5.2).

Another approach is to start directly from the definition of the lead field L. Because it is a linear operator, its restriction to one sensor is a linear functional, and it can be formulated with its Riesz representation : for instance, for a measurement of the electric potential V between positions $\mathbf{r}_1$ and $\mathbf{r}_2$, the lead field L_{12} is such that

$$V(\mathbf{r}_1) - V(\mathbf{r}_2) = \int_\Omega L_{12}(\mathbf{r}) \cdot \mathbf{J}^\mathrm{p}(\mathbf{r}) \ dr \ .$$

If L_{12} can be computed, then any source $\mathbf{J}^\mathrm{p}$ can be projected on the measurement $V(\mathbf{r}_1) - V(\mathbf{r}_2)$ with a simple scalar product. In this example, the equation of L_{12} is known from the Helmholtz reciprocity principle. It states that, if $\mathbf{J}^\mathrm{p} = \mathbf{q}\delta_{\mathbf{r}_0}$, with $\delta_{\mathbf{r}_0}$ being the Dirac distribution at $\mathbf{r}_0$, then $V(\mathbf{r}_1) - V(\mathbf{r}_2) = \mathbf{q} \cdot \nabla U(\mathbf{r}_0)$, where U is the potential generated by a current injection between $\mathbf{r}_1$ and $\mathbf{r}_2$. It follows that $L_{12} = \nabla U$. So in this case, L_{12} can be computed from U, for which the equation is :

$$\left\{ \begin{array}{ll} \nabla \cdot (\sigma \nabla U) = 0 & in \quad \Omega \\ \sigma \nabla U \cdot \mathbf{n} = \delta_{\mathbf{r}_1} - \delta_{\mathbf{r}_2} & on \quad \partial\Omega \end{array} \right. \tag{5.4}$$

This equation can be solved numerically for complex geometries, as described in [105]. For the magnetic field, the equation of the sensor-based lead field was first presented in [74], and different numeric implementations were described for piecewise constant conductivities [74, 90].

These two approaches that we described, using linear algebra or reciprocity, are very similar, as they both change the forward problem from a source point of view to a sensor point of view. The difference is that one does it in a discrete space, whereas the other keeps the original continuous space. We think that the continuous approach has the advantage of giving a general formulation of the lead field which is independent of the discretization used for numerical computation.

In this chapter, we propose to use the adjoint method [61, 34] as a simple and powerful tool to derive the differential equation of the lead field with respect to a given sensor. It can handle both EEG and MEG lead fields, and because it is a general framework, we are able to include in an easy way the geometry of the sensors in the lead field equation, which can be very important for MEG. The purpose of this chapter is thus to provide all the sensor-based lead field equations, especially for non-pointlike sensors because some of them have not been presented before.

2 THE ADJOINT METHOD

Let E be an Hilbert space, i.e. a Banach space equipped with an inner product. In our case, we will consider $E = L^2(\Omega)$, the space of real square-integrable functions

defined on an open bounded region Ω equipped with the inner product

$$< u, v >= \int_\Omega u(\mathbf{r})v(\mathbf{r})dr \ .$$

Let p represent a parameter which can be a real scalar or vector function defined in some functional space E'. For any p, we consider the (hopefully unique) function v of E which satisfies the state equation :

$$\mathbf{A}v = b(p) \ , \tag{5.5}$$

where $\mathbf{A}$ is a linear operator from E to another set $E_1 \subset E$ and b is a differentiable function from E' to E_1. This defines a mapping $p \rightarrow v(p)$ where the solution $v(p)$ of (5.5) is called the state function. To give some intuition, in the EEG case the state function v is the electric potential $V(\mathbf{r})$ and the parameter p is the primary source current vector $\mathbf{J}^{\mathrm{p}}(\mathbf{r})$. We assume that the mapping $p \rightarrow v(p)$ is differentiable.

We also make a measurement of the state function v which can be modeled as a linear functional $f(v)$ from E to $\mathbb{R}$. For $v(p)$ solution of the state equation, we can express the measurement as a functional g of p from E' to $\mathbb{R}$:

$$g(p) = f(v(p)) \ .$$

We want to compute the derivative of g with respect to p by using the adjoint method. Indeed, for our application to EEG and MEG, the derivative of g represents the lead field of the measurement g.

First, we build a Lagrangian L by adding the measurement to the product of the state equation with a Lagrange multiplier w :

$$L(p, v, w) = f(v) + < w, \mathbf{A}v - b(p) > \ .$$

This Lagrangian can be compared to the Lagrangian used in optimization problems, where it is built as the sum of the function to minimize and the product of the constraints with a Lagrange multiplier. In our continuous setting, the Lagrange multiplier w is a function living in the space of test functions $E_2 \subset E_1$. We assume that the Lagrangian L is differentiable with respect to all three variables p, v, w. As soon as $v = v(p)$ is solution of the state equation, we have

$$g(p) = L(p, v(p), w) \ .$$

From this equation, we now want to compute the derivative of g with respect to p. Using the differential notation, we consider the differential δg with respect to the differential δp :

$$\delta g = \frac{\partial L}{\partial v}(p, v(p), w)\delta v + \frac{\partial L}{\partial p}(p, v(p), w)\delta p \ , \tag{5.6}$$

which holds for all w in E_2. Note that the differential δw does not appear since w does not depend on p. We choose the Lagrange multiplier so that the first term vanishes, i.e. defined by the equation

$$\begin{array}{l} \frac{\partial L}{\partial v}(p, v(p), w)\delta v = 0 \quad \text{for all} \quad \delta v \\ \frac{\partial f}{\partial v}\delta v + < w, \mathbf{A}\delta v >= 0 \quad \text{for all} \quad \delta v \ . \end{array}$$

We now use the fact that in a Hilbert space, if $\mathbf{H}$ is a linear operator, the inner product $< x, \mathbf{H}y >$ is equal to $< \mathbf{H}^* x, y >$, where $\mathbf{H}^*$ is the linear operator adjoint to $\mathbf{H}$. We thus introduce the adjoint operator $\mathbf{A}^*$ and rewrite the previous equation as

$$\frac{\partial f}{\partial v}\delta v + < \mathbf{A}^* w, \delta v >= 0 \quad \text{for all} \quad \delta v \ ,$$

which is equivalent to

$$\mathbf{A}^* w = -\frac{\partial f}{\partial v} \ . \tag{5.7}$$

This equation is called the adjoint equation. Therefore, if v and w are respectively solutions of (5.5) and (5.7), the relation (5.6) reduces to

$$\delta g = \frac{\partial L}{\partial p}(p, v(p), w)\delta p \ ,$$

which is simply

$$\delta g =< w, \frac{\partial b}{\partial p}\delta p > \ .$$

Hence the derivative of g can be computed from the sole derivative of b. When the direct computation of the derivative of g is complex, the adjoint method is particularly interesting if the derivative of b is simple.

In EEG and MEG, the quasi-static approximation of Maxwell's equations is used. In this framework, the electric potential and the magnetic field depend on the primary current vector $\mathbf{J}^{\mathrm{p}}$, which represents brain activity, and in particular they are both linear with respect to $\mathbf{J}^{\mathrm{p}}$. As a consequence, any electric or magnetic measurement at a given sensor is linear with respect to $\mathbf{J}^{\mathrm{p}}$. Let $g(\mathbf{J}^{\mathrm{p}})$ be such a measurement. Because $g(\mathbf{J}^{\mathrm{p}})$ is linear, it can be formulated exactly using its derivative : for any primary current distribution $\mathbf{J}^{\mathrm{p}}$,

$$g(\mathbf{J}^{\mathrm{p}}) =< \frac{\partial g}{\partial \mathbf{J}^{\mathrm{p}}}, \mathbf{J}^{\mathrm{p}} >= \int_\Omega \frac{\partial g}{\partial \mathbf{J}^{\mathrm{p}}} \mathbf{J}^{\mathrm{p}} \ .$$

So $\frac{\partial g}{\partial \mathbf{J}^{\mathrm{p}}}$ is exactly the lead field for the given measurement. And this derivative can be easily computed with the adjoint method. The adjoint method is hence a powerful and general framework to compute the lead field for any type of measurement.

3 POINTLIKE LEAD FIELDS

3.1 EEG lead field

The function $g(\mathbf{J}^{\mathrm{p}})$ that we consider is a measurement of the electric potential V at a certain electrode location $\mathbf{r}_i$, with respect to a reference at the electrode location $\mathbf{r}_0$. We now make explicit the formalism introduced in section 2.

- We consider the functional space $E = L^2(\Omega)$ of real square-integrable functions

on Ω, an open bounded region of $\mathbb{R}^3$ representing the head domain. The scalar product is $< u, v >= \int_\Omega u(\mathbf{r})v(\mathbf{r})dr$.

- p is the primary source current vector field $\mathbf{J}^\mathrm{p}(\mathbf{r})$, defined in some functional space E' on Ω.

- v is the electric potential $V(\mathbf{r}) \in \mathcal{C}^0(\Omega) \cap E$.

- $g(\mathbf{J}^\mathrm{p}) = f(V(\mathbf{J}^\mathrm{p})) = V(\mathbf{r}_i) - V(\mathbf{r}_0) = \int_\Omega V(\delta_{\mathbf{r}_i} - \delta_{\mathbf{r}_0})dr$ where $\delta_{\mathbf{r}_i}$ is the Dirac distribution at $\mathbf{r}_i$.

- V is solution of the following differential equation (the state equation) :

$$\begin{cases} \nabla \cdot (\sigma \nabla V) = \nabla \cdot \mathbf{J}^\mathrm{p} \quad in \quad \Omega \\ \sigma \nabla V \cdot \mathbf{n} = 0 \quad on \quad S = \partial\Omega \end{cases}$$

  where S is the boundary of Ω, $\mathbf{n}$ is the unit normal vector to S and $\sigma(\mathbf{r})$ is the conductivity. In this case, $\mathbf{A}V = \nabla \cdot (\sigma \nabla V)$ and $b(\mathbf{J}^\mathrm{p}) = \nabla \cdot \mathbf{J}^\mathrm{p}$.

- The Lagrangian is the sum of the measurement and the state equation multiplied by a Lagrange multiplier w :

$$L(\mathbf{J}^\mathrm{p}, V, w) = \int_\Omega V(\delta_{\mathbf{r}_i} - \delta_{\mathbf{r}_0})dr + \int_\Omega (\nabla \cdot (\sigma \nabla V) - \nabla \cdot \mathbf{J}^\mathrm{p})w dr \quad .$$

Let us first formulate the adjoint equation. Physically, V and $\sigma \nabla V$ are continuous through the eventual discontinuity surfaces S_k of σ :

$$\begin{cases} [V]_{S_k} = 0 \\ [\sigma \nabla V \cdot \mathbf{n}]_{S_k} = 0 \end{cases}$$

where $[.]_{S_k}$ denotes the jump of a function on a given surface S_k. We take a Lagrange multiplier w which verifies the same properties. Then the divergence theorem gives :

$$\int_\Omega (\nabla \cdot (\sigma \nabla V))w dr = \int_S w \sigma \nabla V \cdot \mathbf{n} ds - \int_\Omega \sigma \nabla V \cdot \nabla w dr$$

$$\int_\Omega (\nabla \cdot (\sigma \nabla w))V dr = \int_S V \sigma \nabla w \cdot \mathbf{n} ds - \int_\Omega \sigma \nabla w \cdot \nabla V dr$$

Because of the boundary condition on V, and the fact that σ is symmetric (conductivity tensor), we get :

$$\int_\Omega (\nabla \cdot (\sigma \nabla V))w dr = \int_\Omega (\nabla \cdot (\sigma \nabla w))V dr - \int_S V \sigma \nabla w \cdot \mathbf{n} ds \quad .$$

Using this identity we can rewrite the Lagrangian :

$$L(\mathbf{J}^\mathrm{p}, V, w) = \int_\Omega V(\delta_{\mathbf{r}_i} - \delta_{\mathbf{r}_0})dr + \int_\Omega (\nabla \cdot (\sigma \nabla w))V dr - \int_S V \sigma \nabla w \cdot \mathbf{n} ds - \int_\Omega (\nabla \cdot \mathbf{J}^\mathrm{p})w dr \quad .$$

As a consequence, the condition $\frac{\partial L}{\partial V} = 0$ can be satisfied if w is solution of the following differential equation :

$$\boxed{\begin{cases} \nabla \cdot (\sigma \nabla w) = 0 \quad in \quad \Omega \\ \sigma \nabla w \cdot \mathbf{n} = \delta_{\mathbf{r}_i} - \delta_{\mathbf{r}_0} \quad on \quad S \end{cases}} \tag{5.8}$$

This corresponds exactly to the equation of the electric potential with a unit current injection on the boundary between positions $\mathbf{r}_i$ and $\mathbf{r}_0$.

The derivative of g is given by $\frac{\partial L}{\partial \mathbf{J}^\mathrm{p}}$. L only depends on $\mathbf{J}^\mathrm{p}$ via the term $-\int_\Omega (\nabla \cdot \mathbf{J}^\mathrm{p}) w dr$, which can be rewritten as $\int_\Omega \nabla w \cdot \mathbf{J}^\mathrm{p}$ using the divergence theorem and the fact that $\mathbf{J}^\mathrm{p}$ is zero on the boundary S. So

$$\boxed{\frac{\partial g}{\partial \mathbf{J}^\mathrm{p}} = \nabla w}$$

and for any primary source $\mathbf{J}^\mathrm{p}$, $g(\mathbf{J}^\mathrm{p}) = \int_\Omega \nabla w \cdot \mathbf{J}^\mathrm{p} dr$. In the particular case of a source being a dipole at location $\mathbf{p}$ and with moment $\mathbf{q}$, we have $\mathbf{J}^\mathrm{p} = \delta_\mathbf{p} \mathbf{q}$ and $g(\delta_\mathbf{p} \mathbf{q}) = \mathbf{q} \cdot \nabla w(p) = V(\mathbf{r}_i) - V(\mathbf{r}_0)$, which is exactly Helmholtz's reciprocity principle.

3.2 MEG lead field

For MEG, the difference with the previous section is that we consider the magnetic field, for which the state equation is different. The function g is now a measurement of the magnetic field at location $\mathbf{r}_i$ and in the direction $\mathbf{d}_i$ (a unitary vector), $g(\mathbf{J}^\mathrm{p}) = \mathbf{d}_i \cdot \mathbf{B}(\mathbf{r}_i)$. The magnetic field is given by the Biot-Savart law :

$$\mathbf{B}(\mathbf{r}_i) = \mathbf{B}_0(\mathbf{r}_i) - \frac{\mu_0}{4\pi} \int_\Omega \sigma \nabla V \times \nabla \left(\frac{1}{R} \right) dr$$

with $\mathbf{B}_0(\mathbf{r}_i) = \frac{\mu_0}{4\pi} \int_\Omega \mathbf{J}^\mathrm{p} \times \nabla \left(\frac{1}{R} \right) dr$ and $R = \|\mathbf{r}_i - \mathbf{r}\|$. Let us consider first the dependence of g on V (dropping the scale factor $\frac{\mu_0}{4\pi}$ for the sake of clarity) :

$$\begin{array}{rcl} \mathbf{d}_i \cdot \int_\Omega \sigma \nabla V \times \nabla \left(\frac{1}{R} \right) & = & \int_\Omega \mathbf{d}_i \cdot \sigma \nabla V \times \nabla \left(\frac{1}{R} \right) \\ & = & \int_\Omega \sigma \nabla V \cdot \nabla \left(\frac{1}{R} \right) \times \mathbf{d}_i \\ & = & \int_\Omega \nabla V \cdot \sigma \nabla \left(\frac{1}{R} \right) \times \mathbf{d}_i \\ & = & \int_\Omega \nabla \cdot \left(V \sigma \nabla \left(\frac{1}{R} \right) \times \mathbf{d}_i \right) - \int_\Omega V \nabla \cdot \left(\sigma \nabla \left(\frac{1}{R} \right) \times \mathbf{d}_i \right) \end{array}$$

Now we want to apply the divergence theorem to the first term of the right hand side. Unfortunately the expression inside the divergence is not necessarily continuous : V and $\nabla \left(\frac{1}{R} \right)$ are continuous but σ is often considered as piecewise continuous within nested domains modeling the different types of tissues inside the head. It is necessary to take into account the discontinuities of σ across the different interfaces S_k between tissues :

$$\mathbf{d}_i \cdot \int_\Omega \sigma \nabla V \times \nabla \left(\frac{1}{R} \right) \quad = \quad \sum_k \int_{S_k} V (\sigma_k^- - \sigma_k^+) \nabla \left(\frac{1}{R} \right) \times \mathbf{d}_i \cdot \mathbf{n} - \int_\Omega V \nabla \cdot \left(\sigma \nabla \left(\frac{1}{R} \right) \times \mathbf{d}_i \right)$$

where the subscripts $-$ and $+$ define the interior and exterior limits of a function with respect to a surface, on which the normal $\mathbf{n}$ is pointing outwards.

This time we take a Lagrange multiplier w which is continuous on Ω, but we

relax the continuity of $\sigma\nabla w \cdot \mathbf{n}$. In this case, the divergence theorem gives :

$$\int_\Omega (\nabla \cdot (\sigma \nabla w))V = \sum_k \int_{S_k} V(\sigma_k^- \nabla w^- \cdot \mathbf{n} - \sigma_k^+ \nabla w^+ \cdot \mathbf{n}) - \int_\Omega \sigma \nabla w \cdot \nabla V$$

In the MEG case, the Lagrangian can then be written as

$$\begin{array}{rcl} L(\mathbf{J^p}, V, w) & = & -\frac{\mu_0}{4\pi}\sum_k \int_{S_k} V(\sigma_k^- - \sigma_k^+)\nabla\left(\frac{1}{R}\right) \times \mathbf{d}_i \cdot \mathbf{n} - \sum_k \int_{S_k} V(\sigma_k^- \nabla w^- \cdot \mathbf{n} - \sigma_k^+ \nabla w^+ \cdot \mathbf{n}) \\ & & +\frac{\mu_0}{4\pi}\int_\Omega V \nabla \cdot \left(\sigma \nabla\left(\frac{1}{R}\right) \times \mathbf{d}_i\right) + \int_\Omega (\nabla \cdot (\sigma \nabla w))V \\ & & +\mathbf{d}_i \cdot \frac{\mu_0}{4\pi}\int_\Omega \mathbf{J^p} \times \nabla\left(\frac{1}{R}\right) - \int_\Omega (\nabla \cdot \mathbf{J^p})w \end{array}$$

Now, considering the condition $\frac{\partial L}{\partial V} = 0$, the adjoint equation becomes a set of differential equations coupled by boundary conditions :

$$\boxed{\left\{ \begin{array}{l} \nabla \cdot (\sigma \nabla w) = -\frac{\mu_0}{4\pi}\nabla \cdot \left(\sigma \nabla\left(\frac{1}{R}\right) \times \mathbf{d}_i\right) \;\; in \;\; \Omega_k, \;\; for \;\; k = 1..N \\ \sigma_k^- \nabla w^- \cdot \mathbf{n} - \sigma_k^+ \nabla w^+ \cdot \mathbf{n} = -\frac{\mu_0}{4\pi}(\sigma_k^- - \sigma_k^+)\nabla\left(\frac{1}{R}\right) \times \mathbf{d}_i \cdot \mathbf{n} \;\; on \;\; S_k, \;\; for \;\; k = 1..N \end{array} \right.} \tag{5.9}$$

It should be noted that if the conductivity σ is constant and isotropic in a domain Ω_k, then we can transform the right hand side of the differential equation :

$$\begin{array}{rcl} \nabla \cdot \left(\sigma \nabla\left(\frac{1}{R}\right) \times \mathbf{d}_i\right) & = & \sigma \nabla \cdot \left(\nabla\left(\frac{1}{R}\right) \times \mathbf{d}_i\right) \\ & = & \sigma(\mathbf{d}_i \cdot \nabla \times \left(\nabla\left(\frac{1}{R}\right)\right) + \nabla\left(\frac{1}{R}\right) \cdot \nabla \times \mathbf{d}_i) \\ & = & 0 \end{array}$$

because the curl of a gradient is zero and $\mathbf{d}_i$ is a constant. In this case, the equation reduces to $\Delta w = 0$, meaning that w is harmonic in the corresponding compartment. This result has been used previously for the numerical computation of the MEG lead field [74, 90].

The expression of $\frac{\partial L}{\partial \mathbf{J^p}}$ is slightly different from the EEG case, as there is a dependency on $\mathbf{J^p}$ in $\mathbf{B}_0(\mathbf{r}_i)$:

$$\begin{array}{rcl} \mathbf{d}_i \cdot \mathbf{B}_0(\mathbf{r}_i) & = & \mathbf{d}_i \cdot \frac{\mu_0}{4\pi}\int_\Omega \mathbf{J^p} \times \nabla\left(\frac{1}{R}\right) \\ & = & \frac{\mu_0}{4\pi}\int_\Omega \mathbf{d}_i \cdot \mathbf{J^p} \times \nabla\left(\frac{1}{R}\right) \\ & = & \frac{\mu_0}{4\pi}\int_\Omega \mathbf{J^p} \cdot \nabla\left(\frac{1}{R}\right) \times \mathbf{d}_i \end{array}$$

Finally

$$\boxed{\frac{\partial g}{\partial \mathbf{J^p}} = \nabla w + \frac{\mu_0}{4\pi}\nabla\left(\frac{1}{R}\right) \times \mathbf{d}_i \;\; .}$$

4 INCORPORATING SENSOR GEOMETRY

In section 3, we simplified the sensor measurements. For instance, we assumed that an EEG electrode measures the potential at a mathematical point $\mathbf{r}_i$, i.e. we used point electrodes. In reality, an electrode has a certain area of contact with the scalp. In the same way, a SQUID sensor does not measure the magnetic field at a single point but the flux of the magnetic field through one or several small loops. The geometries of the different sensors can be easily incorporated in our framework

simply by reformulating the function g.

4.1 MEG sensors

A magnetometer measures the flux of the magnetic field through a small loop. For a magnetometer i, let M_i be the surface enclosed by the loop, and $\mathbf{d}_i$ the unitary vector normal to M_i. The function g can then be written as $g(\mathbf{J}^{\mathrm{p}}) = \int_{M_i} \mathbf{d}_i \cdot \mathbf{B}(\mathbf{r}')dr'$. In the Biot-Savart law, the only dependence of $\mathbf{B}(\mathbf{r}')$ on $\mathbf{r}'$ is in $R = \|\mathbf{r}' - \mathbf{r}\|$, see section 3.2. Then the only change in the adjoint equation is in the term $\nabla\left(\frac{1}{R}\right) \times \mathbf{d}_i$, which becomes

$$\int_{M_i} \nabla\left(\frac{1}{R}\right) \times \mathbf{d}_i \ dr' \ .$$

Using Stokes theorem, this can also be rewritten as the following line integral

$$\left(\int_{\partial M_i} \frac{1}{R}\mathbf{t}(\mathbf{r}')dr'\right) \ , \tag{5.10}$$

where $\mathbf{t}$ is the tangent vector to the boundary ∂M_i of the loop. This formulation is the same as the one given in [110]. For a gradiometer, the measurement is the linear combination of flux of the magnetic field through two or more close parallel loops. For instance, for a first-order gradiometer, let G_i^+ and G_i^- be the two surfaces enclosed by the two loops, then the term $\nabla\left(\frac{1}{R}\right) \times \mathbf{d}_i$ is transformed in

$$\int_{\partial G_i^+} \frac{1}{R}\mathbf{t}(\mathbf{r}')dr' - \int_{\partial G_i^-} \frac{1}{R}\mathbf{t}(\mathbf{r}')dr' \ .$$

Generally, the MEG manufacturers give a set of positions and weights for each sensor, and the linear combination of the magnetic field at these positions using these weights is meant to recreate the measurement. For a set $(\mathbf{r}_k, \lambda_k)$ of positions and weights, the term $\nabla\left(\frac{1}{R}\right) \times \mathbf{d}_i$ becomes

$$\left(\sum_k \lambda_k \nabla\left(\frac{1}{R_k}\right)\right) \times \mathbf{d}_i \ ,$$

where $R_k = \|\mathbf{r}_k - \mathbf{r}\|$.

4.2 EEG surface electrodes

To incorporate the surface electrodes, we need to take into account the fact that the electric potential is constant at the surface of the electrodes due to the high conducting metal. This is called the *shunt effect*. This effect has first been modeled for electrical impedance tomography (EIT) [13, 97] and then for EEG [77]. The shunt effect simply modifies the boundary conditions of the electric potential PDE. The simple homogeneous Neumann condition is transformed to :

$$\begin{cases} V + z_k \sigma \nabla V \cdot \mathbf{n} = v_k \quad on \quad e_k \\ \int_{e_k} \sigma \nabla V \cdot \mathbf{n} = 0 \\ \sigma \nabla V \cdot \mathbf{n} = 0 \quad on \quad S \backslash \cup e_k \end{cases} \tag{5.11}$$

where e_k is the kth electrode, v_k is the constant value of the potential on the kth electrode and z_k is the effective contact impedance which models the electrochemical

effect at the skin-electrode interface.

It is straightforward from (5.11) that $v_k = \frac{1}{|e_k|}\int_{e_k} V$, where $|e_k|$ denotes the area of the electrode e_k. Then a potential measurement between electrode i and reference 0 can be defined as :

$$g(\mathbf{J}^{\mathrm{p}}) = \frac{1}{|e_i|}\int_{e_i} V - \frac{1}{|e_0|}\int_{e_0} V = \int_\Omega V\left(\frac{\delta_{e_i}}{|e_i|} - \frac{\delta_{e_0}}{|e_0|}\right)$$

where δ_{e_k} is the distribution such that $\int_\Omega V\delta_{e_k} = \int_{e_k} V$.

We now proceed as in section 3.1 and we add the boundary conditions (5.11). The first difference compared to point electrodes is that the following boundary integral does not vanish anymore :

$$\begin{array}{ll}\int_S w\sigma\nabla V\cdot\mathbf{n}ds & = \sum_k \int_{e_k}\frac{1}{z_k}(-V+v_k)w\ \ ds \\ & = \sum_k \int_{e_k}\frac{1}{z_k}(-V+\frac{1}{|e_k|}\int_{e_k} V)w\ \ ds \\ & = \sum_k \int_\Omega \frac{1}{z_k}(-V+\frac{1}{|e_k|}\int_\Omega V\delta_k dr)w\delta_k\ \ dr\end{array}$$

Deriving this last expression with respect to V gives :

$$\sum_k \frac{1}{z_k}(-w+\frac{1}{|e_k|}\int_{e_k} w)\delta_k\ \ .$$

The second difference is that the measurement $g(\mathbf{J}^{\mathrm{p}})$ is now :

$$g(\mathbf{J}^{\mathrm{p}}) = \int_\Omega V\left(\frac{\delta_{e_i}}{|e_i|} - \frac{\delta_{e_0}}{|e_0|}\right)\ \ ,$$

for which the derivative with respect to V is :

$$\frac{\delta_{e_i}}{|e_i|} - \frac{\delta_{e_0}}{|e_0|}\ \ .$$

By incorporating these two changes in the adjoint equation for point electrodes (5.8), we get the new adjoint equation for surface electrodes :

$$\left\{\begin{array}{l}\nabla\cdot(\sigma\nabla w) = 0 \quad in \quad \Omega \\ \sigma\nabla w\cdot\mathbf{n} = \frac{\delta_{e_i}}{|e_i|} - \frac{\delta_{e_0}}{|e_0|} + \sum_k \frac{1}{z_k}\left(-w+\frac{1}{|e_k|}\int_{e_k} w\right)\delta_k \quad on \quad S\end{array}\right. \tag{5.12}$$

Integrating the boundary condition of (5.12) on e_k gives :

$$\int_{e_k}\sigma\nabla w\cdot\mathbf{n} = \begin{cases}1 & k=i \\ -1 & k=0 \\ 0 & otherwise\end{cases}\ \ . \tag{5.13}$$

Also, on each electrode e_k,

$$w + z_k\sigma\nabla w\cdot\mathbf{n} = W_k \quad on \quad e_k, \tag{5.14}$$

where W_k is a constant, and outside the electrodes :

$$\sigma\nabla w\cdot\mathbf{n} = 0 \quad on \quad S\backslash\cup e_k\ \ . \tag{5.15}$$

The boundary conditions (5.13), (5.14) and (5.15) differ from (5.11) only by the fact that there is a non-zero current at the electrodes. Now the adjoint equation is exactly the equation of the electric potential with a unitary current injection between electrodes e_i and e_0.

5 NUMERICAL SIMULATIONS

To illustrate our approach, we computed the lead field for magnetometers using the finite element method presented in 4. We used a spherical geometry to be able to compare the numerical solution with the ground truth given by the analytical formulation. The geometry was composed of three nested spheres with radii of 0.87, 0.92, 1, meant to represent brain, skull and scalp tissues. We assigned constant isotropic conductivities of 1, 0.02, 1 to brain, skull, scalp respectively. It is known that in a spherical geometry the magnetic field outside the conductor does not depend on the conductivities, but we intentionally put different conductivities in our model to test that the numerical solution is actually similar to the case of a homogeneous sphere. This geometry was embedded in a Cartesian grid with a resolution of 128x128x128, defining a Cartesian mesh that is used to define a trilinear element basis (for more details, we refer to chapter 4). To give an idea, with a 128x128x128 resolution, the spherical geometry contains a little less than 10^6 mesh nodes. We placed 89 magnetometers equally distributed on the positive z hemisphere, oriented in the x direction, positioned at a distance of 0.03 of the outermost sphere, and with a radius of 0.015. For each magnetometer, we solved the differential equation (5.9), with the modification (5.10), using the implicit finite element method. The integral in (5.10) was computed with a Gauss-Kronod method using 61 points. For a solution w of (5.9), and a dipole with position $\mathbf{r}_0$ and moment $\mathbf{q}$, the quantity $\nabla w(\mathbf{r}_0) \cdot \mathbf{q}$ gives the part of the magnetometer measurement generated by Ohmic current (often called secondary field). Analytically, the secondary field generated by a dipole in a spherical geometry can be computed by subtracting the analytical formulation of the primary field to Sarvas' formula for the total magnetic field [88]. This analytic formulation was integrated on the magnetometers surfaces to get the magnetometer measurement (also using a Gauss method for numerical integration). So we compared at the sensors the numerical and analytical secondary fields measurements for many dipoles located at various depths on the z axis, with all Cartesian orientations. The error with respect to the analytical solution is summarized by two quantities, the RDM which gives the topographic error, and the MAG which gives the magnitude error :

$$\begin{cases} RDM(B_n, B_a) = \left\| \frac{B_n}{\|B_n\|} - \frac{B_a}{\|B_a\|} \right\| \\ MAG(B_n, B_a) = \frac{\|B_n\|}{\|B_a\|} \end{cases}$$

where $\|.\|$ is the discrete l_2-norm and B_n, B_a are the set of measurements of the secondary field at the sensors for the numerical solution and analytical solution respectively. The results are shown on figure 5.1. For dipoles in y and z directions, the error of the numerical solution is very small, as it is always under 1%. The accuracy slightly decreases when the dipole gets very close to the innermost sphere,

ie close to the interface between conductivities : this is a well known effect when using BEM or FEM methods. For the dipoles in x direction, we observe different results : the MAG varies between 0.985 and 1.03, and the RDM is below 3% for most dipole positions but fastly increases when the dipole gets close to the center of the sphere. These results are due to the fact that for dipoles in the x direction, the x component of the secondary field tends to zero when the dipole gets close to the center of the spherical geometry. In this case, the RDM and MAG measures have quantities in the denominator that also tends to zero, which is responsible for the effect observed only for dipoles in x direction. For these dipoles, RDM and MAG are not relevant measures, and it is better to simply consider the absolute error. The figure 5.2 shows that the absolute error is similar for the three dipole orientations, which validates the numerical solution for dipoles in x direction.

Nevertheless, our purpose here is not to show the quality of the numerical computations but to illustrate the correctness of the equations previously derived. In the case presented here, the interest is that we have to solve only one differential equation to compute the whole flux of the magnetic field through one magnetometer, instead of having to compute several pointlike lead fields at several points of the magnetometer surface and then approximate the magnetic flux using these points. For example, if a sensor is approximated using a linear combination of four points, then the computational time can be divided by four.

6 CONCLUSION

We proposed to use the adjoint method to derive the equations of the EEG and MEG sensor-based lead fields. By using this simple and general framework, we were thus able to rederive the lead field equations for pointlike sensors, both for EEG and MEG, and we also showed how to extend very easily these equations to incorporate the geometry of the sensors in the lead field. Our goal is to give a better insight on EEG-MEG lead field computation, and also to provide a complete list of the PDE for the sensor-based lead fields, for all type of sensors. All these equations are simple second-order elliptic PDE in divergence form, and therefore they can be directly plugged in any Finite Difference or Finite Element solver.

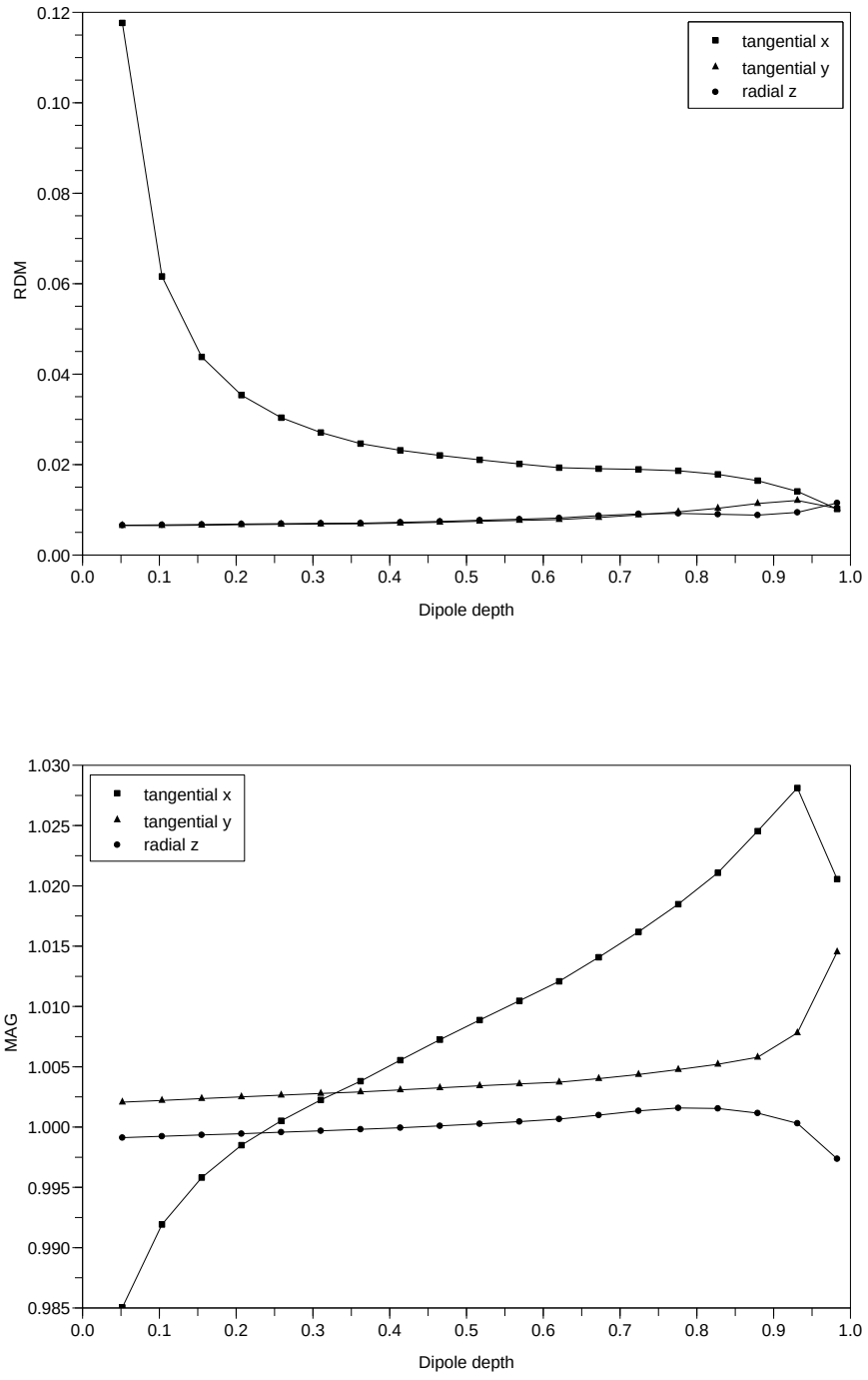

Figure 5.1: RDM and MAG between numerical and analytical solution with respect to dipole depth. The dipoles are located on the z axis, and the dipole positions are given relatively to the radius of the innermost sphere (a value of 1 means that the dipole is located on the sphere). The three Cartesian coordinates have been considered for the dipole orientations.

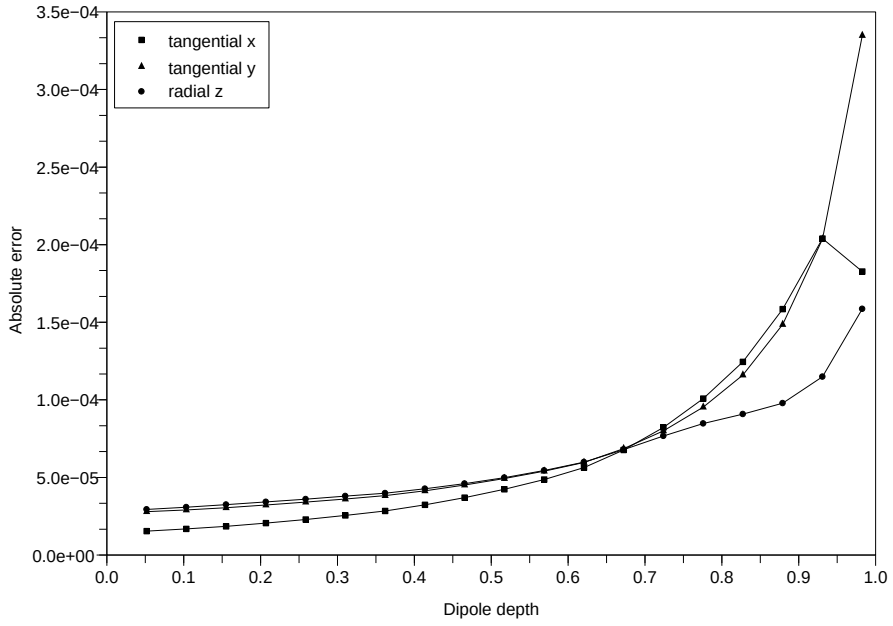

Figure 5.2: Absolute error between numerical and analytical solution with respect to dipole depth.

Part II

Conductivity calibration

CHAPTER 6

GLOBAL SENSITIVITY ANALYSIS OF THREE AND FOUR-LAYER EEG CONDUCTIVITY MODELS

The accuracy of forward models for electroencephalography (EEG) partly depends on the conductivity values of the head tissues. Yet the influence of the conductivities on the model output is still not well understood. In this chapter, we apply a variance-based sensitivity analysis method to the most common EEG forward models (three or four layers). This method is global because it quantifies the influence of each parameter with all the parameters varying at the same time. With non-linear models, it helps to understand the interaction between parameters, which is not possible with simple sensitivity analyses (one-at-a-time variations, derivatives, perturbations). By analyzing the potential topographies at the electrodes, we obtained several results. For a shallow dipole, the brain conductivity effect is negligible and the influence of skull and scalp conductivities appears mainly via their interaction. It means that the variability of the scalp topographies is driven mostly by a function of skull and scalp conductivities. Similar results are presented for skull anisotropy and for a current injection as performed in electrical impedance tomography (EIT). This global sensitivity analysis gives new information about EEG forward models : it identifies the main input factors which need model refinement, and gives directions on how to calibrate these models.

Contents

1 INTRODUCTION

Electroencephalography (EEG) is becoming a more and more common functional brain imaging modality. Thus, it is of interest to improve the resolution of the inverse EEG problem, which is spatially lower than magnetoencephalography (MEG) and functional magnetic resonance imaging (fMRI). The main problem in EEG is its sensitivity to electrical properties of head tissues, which can affect the EEG source localization [49]. Unfortunately, the tissue conductivities can vary among subjects (especially the skull conductivity) and there is no available technique to measure precisely the conductivity of the head tissues *in vivo* (although MREIT seems promising). As a consequence, for the time being, the conductivity models used for EEG are built from the segmentation of a subject's MRI in three or more nested tissues (scalp, skull, CSF, gray matter, white matter). Then scalar values are assigned to each tissue, describing a uniform conductivity (isotropic, or anisotropic with constant ratio).

The electrical conductivities of many human tissues have been measured *in vitro* and are available in the literature [29, 30]. Some tissues have also been measured invasively for animals [60, 113] and for humans [6, 48, 57, 117]. But these measured values are not necessarily the best values to put in a forward EEG model. First, the skull is a very variable tissue depending on the person and the age, and so its electrical conductivity can not be tabulated once and for everybody. Second, the forward model gives an approximation of the real conductivity distribution of the head, and so the conductivity parameters for which the forward model best reproduces reality are not necessarily the physiological conductivity values. For instance, when using a classical three-layer model of the head (brain, skull, scalp), many types of tissues are omitted, but the approximation error of the model can be compensated for if one chooses "efficient" conductivity values instead of physiological values. The efficient conductivities would be the values for which a given model best reproduces the real propagation of the electric potential. This is why it is important to understand the sensitivity of these models to the parameters (the scalar conductivity values), in aim of producing more accurate models. Several sensitivity analyses of conductivity models have been carried out [46, 65, 31, 109, 104, 83], but none of them was a global sensitivity analysis, meaning that the effect of a parameter is evaluated while all others are also varying. They are either one-at-a-time designs [46, 65, 109, 83], where one factor is varied while the others are fixed to nominal values, or local sensitivity analyses [31, 104], for which small perturbations are considered. These approaches are limited when dealing with non-linear models because they are unable to appreciate the interaction effect between parameters, which can be very important to understand the behavior of the model.

This chapter presents a global sensitivity analysis of the EEG forward problem with respect to conductivities. The analysis is performed on the EEG scalp topographies, by considering the effect of conductivity parameters on the RDM, a quantity which summarizes the topographic error. This is of main interest because most of the source localization methods depends almost entirely on the topography of the electric potential at the EEG electrodes. In section 2, we briefly describe the variance-based methods for sensitivity analysis. Then in the following sections, we give the results of our global sensitivity analysis on the EEG and EIT forward models, for different source configurations and conductivity models. Finally, we show the

interest of this sensitivity analysis for the calibration of the EEG forward model.

2 VARIANCE BASED METHODS FOR SENSITIVITY ANALYSIS

Let us assume a model $y = f(\mathbf{x})$ with k input parameters $\mathbf{x} = (x_1, x_2, ..., x_k)$ and a single output y. The imperfect knowledge of the parameters is described by a probability density function $p(\mathbf{x}) = p(x_1, x_2, ..., x_k)$. Let us consider x and y as realizations of the random variables X and Y. In this stochastic framework, to completely characterize the uncertainty of Y, the knowledge of the distribution of Y would be necessary. Still, one simple and good indicator for the uncertainty of the model output Y is its variance $V(Y)$. Following this idea, we can say that a parameter X_i is important if the variance decreases when X_i is known and fixed in the model. In other words, X_i is important if the conditional variance $V(Y|X_i = x_i^*)$ is small compared to the total variance $V(Y)$, where x_i^* is the true value of X_i. Unfortunately we do not know x_i^*, yet we can still look at the average over all possible values of X_i, $E(V(Y|X_i))$. The more important X_i, the smaller this quantity. Since the theorem of the total variance states that $V(Y) = V(E(Y|X_i)) + E(V(Y|X_i))$, we can rather look at the quantity $V(E(Y|X_i))$. The more important X_i, the bigger this quantity. So finally, the following coefficient S_i measures the importance of a parameter X_i :

$$S_i = \frac{V(E(Y|X_i))}{V(Y)}.$$

The indices S_i are more reliable measures than what can be obtained with one-at-a-time variations or local analyses because they include multidimensional averaging over the whole range of uncertainty of all the parameters. These indices are commonly referred to as first-order effect indices. Yet they are not sufficient to describe all the variability of the model, because the identity $\sum_i S_i = 1$ only holds if the model is additive (a linear model is a particular case). For non-linear models, most of the time $\sum_i S_i < 1$, and the residual variance is then explained by the concept of interaction. Two parameters are interacting if their joint effect is greater than the sum of their first-order effects, hence the interaction between two factors X_i and X_j can be quantified using the variance :

$$S_{ij} = \frac{V(E(Y|X_i, X_j)) - V(E(Y|X_i) - V(E(Y|X_j)}{V(Y)}.$$

The indices S_{ij} are called second-order indices. Similarly, one can define third-order (S_{ijk}), fourth-order (S_{ijkl}) or higher order indices, which quantify the interaction between three, four or more parameters. All the first-order and higher order indices are easy to interpret as they all sum to 1, and thus give the apportionment of the uncertainty of the output with respect to the input parameters.

When analyzing a model, if the number k of parameters is too important, there are too many sensitivity measures to consider, so a good way to summarize the

interactions is to use the following measures :

$$S_{T_i} = \sum_{I \in \#i} S_I \ ,$$

where I is a (multi-)index and $\#i$ is meant to represent all the set of (multi-)indices which contain the index i ($i, ij, ik, ijk, \dots$). S_{T_i} is called the total effect index of factor X_i, and measures the first-order effect of X_i plus all its interactions with the other parameters.

These sensitivity indices raise the problem of how to compute the conditional variances. If the model is very simple, an analytical expression for the conditional variances $V(E(Y|X_i))$ can be found, but this is rarely the case. The common strategy is to sample the space of input parameters with respect to their prior probability distribution, to compute the output for these different sample values, and then to evaluate estimators of the sensitivity indices. The two most known methods to estimate variance-based sensitivity indices are Sobol's [96] and the Fourier Amplitude Sensitivity Test (FAST) [18]. An extensive review of these methods can be found in [86]. For the work presented here, we used the FAST method, which has the advantage of giving accurate estimations of the sensitivity indices with a rather small sampling of the input space. The drawback of the method is that only the first order and total effect indices can be computed. The FAST method is based on selecting N points over a particular space-filling curve in the kth dimensional parameter space, built so as to explore each parameter with a different integer frequency $(w_1, w_2, \dots, w_k)$. These frequencies must be such as they do not interfere up to a certain harmonic order M (usually $M = 4$ or $M = 6$ is sufficient). The model is run for each of the N points of the curve and the Fourier spectrum is calculated on the model output at specific frequencies $(w_i, 2w_i, \dots, Mw_i)$ to estimate the first-order sensitivity index of parameter X_i. The total effect indices are obtained by selecting other frequencies of the spectrum.

3 SENSITIVITY ANALYSIS OF EEG FORWARD MODELS

3.1 Design of the analysis

The first step of the analysis is to choose a meaningful output of the model. The common output of an EEG forward model is a vector $\mathbf{u}$ containing the values of the electric potential at the electrode positions. A direct method would be to perform a sensitivity analysis for each electrode, but the results would be hard to interpret. Because the primary goal of EEG forward models is to be the first step for brain source localization, we think that the best output to analyze is the topographic variation of the electric potential at the electrodes. This is motivated by the fact that source localization almost only depends on the topography of the electric potential at the electrodes. Indeed, the differential equation of the forward EEG problem in a

	Range	Mean
Brain	[0.5,1.5]	1.0
Skull	[0.01,0.03]	0.02
Scalp	[0.5,1.5]	1.0

Table 6.1: Conductivity ranges for a three-layer isotropic model

head domain Ω

$$\begin{cases} \nabla \cdot (\sigma \nabla u) = f \quad in \quad \Omega \\ \sigma \nabla u \cdot \mathbf{n} = 0 \quad on \quad \partial\Omega \end{cases}$$

states that there is a linear dependency of the potential u on the source f. As a consequence, a source λf would generate a potential λu. So the amplitude of u does not hold any useful information for the localization of f, and we will consider only the topography of the potential. Hence we build the following output for our model, based on the Relative Difference Measure (RDM) :

$$y = f(\mathbf{x}) = RDM(\mathbf{u}, \mathbf{u}_{ref}) = \left\| \frac{\mathbf{u}}{\|\mathbf{u}\|} - \frac{\mathbf{u}_{ref}}{\|\mathbf{u}_{ref}\|} \right\|,$$

where $\|.\|$ is the discrete l^2-norm, and $\mathbf{u}$ is a sample set of the electric potential at the electrode positions, obtained for a given set of conductivity realization $\mathbf{x} = (x_1, x_2, ..., x_k)$. The topographic variation is computed with respect to a reference potential $\mathbf{u}_{ref}$ which is fixed in the whole analysis. For the reference, our choice is to take the potential obtained with the conductivity values corresponding to the expectation of the parameters $E(X_1), ..., E(X_n)$.

We then have to define the prior distribution of the conductivity parameters $p(x_1, x_2, ..., x_k)$. In vitro [29, 30] and in vivo [78, 1, 48, 57, 117] measurements of the conductivities which can be found in the literature are not sufficient to define a precise distribution. One certain fact is that the skull has a lower conductivity than other tissues : in the literature, the ratio between scalp and skull conductivity ranges approximatively from 15 to 120. Tissues other than the skull are mostly watery, and their conductivity can all be assumed to be in the same range (relatively to the skull). For the sake of simplicity, we mainly focus in this chapter on a three-layer model of the head (brain, skull, scalp), describing only the main tissue differences of the head. Because we do not have real priors, we just assume uniform distributions over the ranges described by table 6.1. Although the uncertainty about the skull conductivity is supposed to be greater than others, we chose the same relative uncertainty for each conductivity. The goal is to have equal uncertainty on the input parameters of the model, so that the results of the sensitivity analysis depend only on the model itself. So for our sensitivity analysis, the reference potential is computed with the mean values of the conductivities : 1, 0.02, 1 for brain, skull, scalp.

3.2 Sampling size and computational cost

For our applications to EEG forward models, the computational cost in realistic geometries is a crucial point, and the sampling of the parameter space has to be rather low. To determine a good trade-off between accuracy and sampling size, we used spherical models for which the forward problem can be computed at a very cheap

cost. We computed the sensitivity indices for many sampling sizes until convergence of the FAST estimators was observed. For a three-layer spherical model with three parameters (isotropic conductivities), we observed the convergence for 600 samples. For the same model with four parameters (skull anisotropy), 800 samples were sufficient to give very good estimates of the sensitivity indices. As a consequence, we used these sampling sizes for the realistic models. The computational cost was further reduced by using a grid of computers where more than 100 calculations could be run in parallel.

3.3 A first simple enlightening case : spherical model with superficial dipolar source

We start with a simple case to show the value of variance-based methods. We use a 3-shell spherical model with radii of 0.87, 0.92, 1 and we use nominal conductivity values of 1.0, 0.02, 1.0 (from brain to scalp). A radial dipole is positioned at 0.83 on the z-axis and the simulated potential is sampled at 64 positions on the positive z hemisphere of the outermost sphere. These positions were uniformly distributed with a 15^o spherical angle. If we perform a one-at-a-time sensitivity analysis, and look at the variation of the RDM with respect to each conductivity separately, we get the result presented in figure 6.1. It appears that the brain conductivity has little importance in the topographic error, whereas skull and scalp conductivities can really affect the potential topography. Now let us consider the variance-based sensitivity indices : we denote x_1, x_2 and x_3 the parameters corresponding to the brain, skull and scalp conductivities respectively. The sensitivity indices are presented in table 6.2. We learn more from these indices : we see that skull and scalp conductivities are not important parameters by themselves (S_2 and S_3 are relatively small), but mostly via their interaction with other parameters (S_{T_2} and S_{T_3} are big). And because S_{T_1} is almost zero, it means that skull and scalp only interact together. Actually, $S_{T_1} = 0.03 = S_1 + S_{12} + S_{13} + S_{123}$ (first-order index plus all interactions of x_1), so $S_{12} + S_{13} + S_{123} < 0.03$, and we can have an estimate of the second-order index S_{23}, which is given by $S_{T_2} - S_2$ or $S_{T_3} - S_3$. We see that $S_{23} \simeq 0.7$, which means that the interaction between scalp and skull conductivities is responsible for about 70% of the total variance of the scalp topographies. Unfortunately, the variance-based analysis does not provide any information about the structure of this interaction. Still we can make a guess : figure 6.2 shows the variations of the output $y = RDM(\mathbf{u}, \mathbf{u}_{ref})$ when skull and scalp are varied at the same time, with the brain fixed at its nominal value. We see that the ratio between scalp and skull conductivities is constant along the isolines. So in this plane where only skull and scalp conductivities vary, the RDM behaves like a function of the scalp/skull conductivity ratio. It means that the skull and scalp conductivities interact through their quotient. This is not surprising, because in the analytical formulation of the electric potential in a spherical conductor [22], the quantities containing the conductivities are quotients of the conductivities of successive layers. Also, because the quotient is a non-linear function, it explains why the first order indices are not sufficient to explain all the variance of the scalp topographies ($\sum_i S_i = 0.26 < 1$). Finally, the most important result of this analysis is that the quantity corresponding to the scalp/skull conductivity ratio drives just by itself 70% of the variability of the EEG scalp topographies (for a 3-shell spherical model).

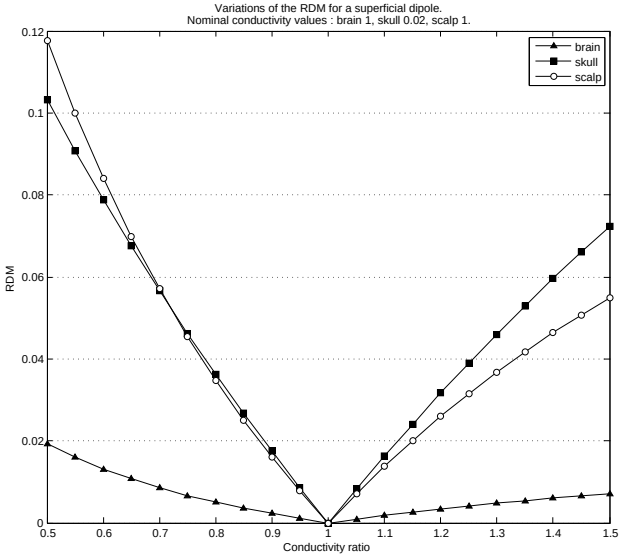

Figure 6.1: Variations of the RDM with respect to each conductivity, in a spherical model, when the source is a superficial dipole.

S_1	S_2	S_3	S_{T_1}	S_{T_2}	S_{T_3}	S_{23}	$\sum S_{ij(k)}, ij \neq 23$
0.00	0.12	0.14	0.03	0.86	0.84	$\simeq 0.7$	< 0.03

Table 6.2: Sensitivity indices for a superficial dipole in a spherical model. The parameters x_1, x_2, x_3 are the brain, skull and scalp conductivities.

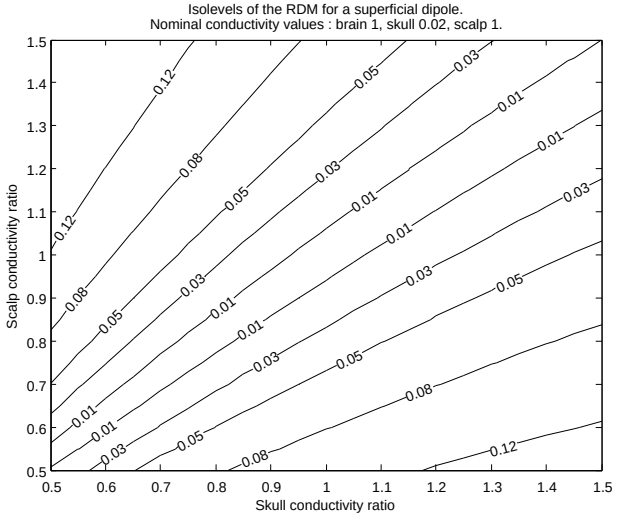

Figure 6.2: Variations of the RDM in the skull-scalp conductivity plane for a spherical model. Isolevels of the RDM are plotted.

3.4 General results on a realistic model

We now consider a three-layer realistic model obtained after segmentation of a T1-MRI of a subject with Brainvisa [16]. The EEG forward problem is solved using the implicit FEM (chapter 4). We use electrode positions registered from a real EEG experiment on the same subject with a 64 10-10 standard system. In this system, 4

electrodes do not record brain signals (HEOG, VEOG, F9, F10), and were removed from the electrode system, resulting in a 60 electrode configuration.

We first show in table 6.3 the maximum achievable RDM among the conductivity ranges defined in table 6.1 for one dipolar source in the brain at various depths. We see that the maximum achievable RDM gets smaller as the depth of the dipole increases. For a dipole located 5 cm under the skull, the biggest RDM is 4%. So it appears that for a three-layer model, the sensitivity to the conductivity values only matters for shallow sources. Also most of the time, the purpose of source localization with EEG is to locate activity in the neo-cortex, which corresponds to shallow sources. For both reasons, we will only consider shallow sources (dipoles) in the following.

Let us consider the case where the model consists of three isotropic layers, like in the previous section. We thus have three parameters x_1, x_2 and x_3 corresponding to conductivity values of brain, skull and scalp respectively. For the source, we chose to position a dipole in the posterior wall of the central sulcus, which corresponds to an activation in the somato-sensory cortex. For this model configuration, the sensitivity indices with respect to the conductivities are given in table 6.4. Although we only computed the first-order and total effect indices, we can still estimate the second order effects like in the previous section. We find that $S_{23} \simeq 0.7$, which means that about 70% of the topographic variability comes from the interaction between skull and scalp conductivities. We see also that the influence of brain conductivity is negligible.

Now considering that skull and scalp conductivities are the main input parameters of the EEG forward model, a logical way to improve the model is to first refine the model for these two tissues. As it was previously proposed [65, 109], we can improve the model of the skull conductivity by considering it as anisotropic with two main directions : radial and tangential with respect to the two closed surfaces defining the skull geometry. The conductivity of the skull is then defined by two scalar values : its radial and tangential conductivity. For a three-layer model with skull anisotropy, we then have four scalar parameters. We denote them x_1, x_2, x_3 and x_4 for brain, radial skull, tangential skull and scalp conductivities respectively. For the conductivity ranges, we kept the interval $[0.01\ \ 0.03]$ for the radial skull conductivity and we assigned the interval $[0.05\ \ 0.15]$ to the tangential skull conductivity. With these ranges, the anisotropy ratio of the skull conductivity can vary between 1.5 and 15. The sensitivity indices for such a model are presented in table 6.5, where the dipolar source is the same as in the isotropic case. The total effect indices S_{T_1} and S_{T_3} are very small, so we can neglect all the high order effects except S_{24}. As a consequence, we can have an estimate of $S_{24} \simeq 0.65$. This shows that a major part of the topographic variability (about 65%) is driven by the interaction between the radial skull conductivity and the scalp, while the effects of brain and tangential skull conductivities are negligible.

Another common extension of the three-layer model is to include the cerebrospinal fluid (CSF), which gives a four-layer model. The importance of the CSF for forward EEG models has been underlined previously [83, 106]. We incorporated this tissue to our three-layer model by adding the surface of the gray matter as a new interface between tissues. It is important to note that in order to carry the numerous computations of the forward model required to compute the sensitivity indices, we used a FEM mesh resolution which is not sufficient to handle the small distance

Dipole depth	1 cm	2 cm	3 cm	4 cm	5 cm
$\max(RDM)$	0.17	0.14	0.11	0.07	0.04

Table 6.3: Maximum of the RDM with respect to the depth of the dipole. The depth of the dipole is given as the distance to the skull in centimeters.

S_1	S_2	S_3	S_{T_1}	S_{T_2}	S_{T_3}	S_{23}	$\sum S_{ij(k)}, ij \neq 23$
0.00	0.10	0.18	0.01	0.82	0.89	$\simeq 0.7$	< 0.01

Table 6.4: Sensitivity indices for a shallow dipole in a three-layer isotropic realistic EEG model. The parameters x_1, x_2, x_3 are the brain, skull and scalp conductivities.

S_1	S_2	S_3	S_4	S_{T_1}	S_{T_2}	S_{T_3}	S_{T_4}	S_{24}	$\sum S_{ij(k)(l)}, ij \neq 24$
0.00	0.07	0.00	0.24	0.02	0.73	0.01	0.92	$\simeq 0.65$	< 0.03

Table 6.5: Sensitivity indices for a shallow dipole in a three-layer realistic EEG model with skull anisotropy. The parameters x_1, x_2, x_3, x_4 are the brain, radial skull, tangential skull and scalp conductivities.

S_1	S_2	S_3	S_4	S_{T_1}	S_{T_2}	S_{T_3}	S_{T_4}
0.05	0.03	0.06	0.16	0.25	0.19	0.56	0.65

Table 6.6: Sensitivity indices for a shallow dipole in a four-layer realistic EEG model. The parameters x_1, x_2, x_3, x_4 are the brain, CSF, skull and scalp conductivities.

separating the inner skull surface and the gray matter surface. As a consequence, we had to scale down the gray matter surface so that the distance to the inner skull surface was numerically reasonable. As a consequence, the four-layer model that we used has quite a big CSF compartment compared to reality and the sensitivity indices that have been computed on this model should be considered accordingly. For the source, we positioned a dipole inside the post-central gyrus, and the parameters are denoted x_1, x_2, x_3 and x_4 for the brain, CSF, skull and scalp conductivities. The conductivity ranges were kept the same as before, and for the CSF we chose a uniform distribution on the interval $[2.5, 7.5]$. For the mean values, we thus have a CSF/brain conductivity ratio of 5, and this ratio can vary between 1.5 and 15 over the distributions of the two conductivities. The sensitivity indices for this model configuration are given in table 6.6. We see first that the first-order indices are all rather small, whereas the total effect indices have all non-negligible values. It underlies again the non-linear dependency of the EEG topographies on the conductivities. It also shows that the interaction structure is much more complicated in this case, because it involves all the parameters. The brain and CSF conductivities now have non negligible effects, with total effect indices of 0.25 and 0.19. The skull and scalp are still the most influent parameters, with total indices of 0.56 and 0.65. It is not possible to estimate the second-order effects directly from the first-order and total indices, because in this case the interaction involves all the parameters.

3.5 Electrical impedance tomography (EIT)

It is also of interest to consider the case when the source is a current injection on the scalp between two electrodes : this type of source configuration is encountered in electrical impedance tomography (EIT), a method which can be used to calibrate

S_1	S_2	S_3	S_{T_1}	S_{T_2}	S_{T_3}	S_{13}	$\sum S_{ij(k)}, ij \neq 13$
0.02	0.01	0.29	0.52	0.14	0.98	$\simeq 0.5$	< 0.13

Table 6.7: Sensitivity indices for a scalp current injection in a three-layer realistic EIT model. The parameters x_1, x_2, x_3 are the brain, skull and scalp conductivities.

S_1	S_2	S_3	S_4	S_{T_1}	S_{T_2}	S_{T_3}	S_{T_4}	S_{14}	$\sum S_{ij(k)(l)}, ij \neq 14$
0.04	0.00	0.00	0.28	0.64	0.07	0.01	0.95	$\simeq 0.5$	< 0.08

Table 6.8: Sensitivity indices for a scalp current injection in a three-layer realistic EIT model with skull anisotropy. The parameters x_1, x_2, x_3, x_4 are the brain, radial skull, tangential skull and scalp conductivities.

the conductivities of EEG forward models [27, 78, 37], since EEG and EIT share the same forward model and only the source term is different. Let us recall briefly the principle of EIT. A current is injected through a pair of electrodes, and the goal is to find the set of conductivity parameters which gives the best match between the forward model simulation and the measurements. For a unitary current injection between positions $\mathbf{r}_1$ and $\mathbf{r}_2$, the differential equation has the following form :

$$\begin{cases} \nabla \cdot (\sigma \nabla u) = 0 \quad in \quad \Omega \\ \sigma \nabla u \cdot \mathbf{n} = \delta_{\mathbf{r}_1} - \delta_{\mathbf{r}_2} \quad on \quad \partial\Omega \end{cases}$$

where $\delta_{\mathbf{r}_1} = \delta(\mathbf{r} - \mathbf{r}_1)$ is the Dirac distribution at $\mathbf{r}_1$. It is easy to see that if the conductivity is multiplied by a scalar factor $\lambda > 0$, then the solution u is divided by λ. As a consequence, if we fix a scale for the conductivity, the EIT problem can be reduced to finding the set of conductivity values which gives the best topography match between the forward model simulation and the measurements. The factor λ to apply to conductivities is then easily given by the amplitude of the measurements. So the EIT problem has been reduced to a topography consideration, and we can use the same sensitivity analysis design as above. With our realistic model, we computed the sensitivity indices when the source is a current injection. Tables 6.7 and 6.8 show these sensitivity indices, with and without skull anisotropy. In both cases, the total indices of the skull conductivity are small and we can estimate the sensitivity index of the interaction between the brain and the scalp only : its value is about equal to 0.5. So we see that the most important factor is the interaction between brain and scalp conductivities, which drives around 50% of the topographic variability. Surprisingly, the skull conductivity has a small effect in this source configuration, but we found that it can be slightly modified depending either on skull thickness or skull conductivity range. If the skull is thicker, or if the range of variation of skull conductivity is shifted towards lower values, then the total effect of skull conductivity increases and the total effect of brain conductivity decreases. For the results presented in tables 6.7 and 6.8, we chose a frontal-occipital electrode pair for the current injection. It should be underlined that the configuration of this electrode pair (short or long distance, frontal-occipital or temporal left-temporal right) had almost no influence on the sensitivity indices.

4 DISCUSSION

The first lesson from this sensitivity analysis is that the skull and scalp tissues are very important for the EEG forward models with three layers. This corresponds to the intuitive idea that the important part of the model is the region between the sources and the sensors. In the EEG case, the sources are believed to be in the gray matter (the outermost part of the cortex) and the sensors are at the scalp surface, and most of the area between these two is covered by skull and scalp tissues. For a shallow source in a simple isotropic three-layer model of the head (brain, skull, scalp), the sensitivity indices confirm this intuition, showing that the influence of the conductivity model on the potential topography at the electrodes is due almost entirely to the skull and scalp conductivities. At the same time, it reveals that the brain conductivity has a very little effect. We think that this is due to the homogeneous model of the brain compartment used in the three-layer model. Indeed, when the brain compartment is more complex (CSF, gray matter, white matter), some studies showed that the conductivities of the brain tissues have non-negligible effects [46, 109]. Still, although this study was done for a coarse model with three layers, we think that it gives directions for further modeling of the head tissues. We believe that it is more important to refine the modeling of the tissues that are located between the sources and the sensors, e.g. the skull and scalp tissues, than the tissues within the brain compartment. Still, in most of the conductivity models, the refinement of the head tissue description focuses on the brain (gray matter, white matter, anisotropy), in particular using DT-MRI modality [100].

One possible improvement for the skull tissue is to add anisotropy. For such a model, our sensitivity analysis reveals that the tangential skull conductivity has almost no role to play in the topographic variability of the potential. It appears that the effect of the skull conductivity comes from its radial component. In [65], it was also observed that the radial conductivity has much more effect than the tangential conductivity. Thus a model which incorporates the skull anisotropy would not bring more variability in the scalp topographies than a model with an isotropic skull conductivity. The relevance of such a model is hence arguable. In [109], the effect of skull anisotropy is found to be important, but the radial and tangential conductivities are varied simultaneously, so the effect of the two skull conductivity components can not be distinguished. Other possible refinements for the skull modeling would be to segment it in several tissues (compact and spongy bone) or to divide it in areas of different conductivities, because its thickness is variable. However such modeling imply an increased accuracy in the skull segmentation, which does not seem easily achievable without user interaction. For the moment, the automatic segmentation of skull from T1-MRI consists most of the time in the computation of a smooth wrapping of the gray matter surface, which defines the inner skull, and this surface is then inflated to get the outer skull.

Another improvement of the model is to include the cerebro-spinal fluid (CSF), which is actually located between the sources and the sensors. Our analysis of such a four-layer model reveals that when incorporating the brain-CSF interface, the brain and CSF conductivities have non-negligible effects. This result is consistent with previous studies [46, 109] which show a non-negligible effect of the brain compartment when it is modeled as composed of different tissues (CSF, gray matter, white matter). Our intuition is that this is due to the complex folding of the surface

corresponding to the brain-CSF interface, which can be responsible for deformations of the EEG topographies. Nevertheless, the skull and scalp conductivities still have the greater sensitivity indices, and hence remain the most important tissues in a four-layer model. It is important to note that we only considered a shallow source, so these conclusions are no more valid for deep sources. It was shown in [109] that for a source in the thalamus, the brain tissues have more influence than the skull.

For all the models we analyzed, the interaction between parameters is always very important, underlying the non-linearity of the potential with respect to the conductivities. For a simple three-layer spherical model, we showed in section 3.3 that there is a high interaction between skull and scalp conductivities, and that this interaction seems to correspond to the scalp/skull conductivity ratio. We assumed this is due to the fact that in the analytical formulation of the electric potential in a spherical conductor [22], the quantities containing the conductivities are quotients of the conductivities of successive layers. Following this idea, we can reparametrize the conductivity models using ratios of conductivities, and recompute the sensitivity indices with this new parametrization. We show in tables 6.9 and 6.10 the sensitivity indices of the conductivity ratios, for the realistic three and four-layer isotropic models. With this new parametrization, we removed a lot of interaction : $\sum_i S_i = 0.94$ for the three-layer model, and $\sum_i S_i = 0.86$ for the four-layer model. It thus shows that even in realistic models, the conductivity ratios of successive layers are very important quantities. For the three-layer model, the first order index of the scalp/skull conductivity ratio is almost equal to 1 ($S_2 = 0.94$), which shows that this quantity drives almost all the variability of the EEG topographies, like for the spherical model. For the four-layer model, the first order index of the scalp/skull conductivity ratio is also very high ($S_3 = 0.69$) and proves again the importance of this quantity, even when modeling the CSF. As a consequence, the primary goal of an EEG forward model calibration should be to estimate the scalp/skull conductivity ratio.

The classical method for conductivity calibration is the electrical impedance tomography (EIT), that we introduced in section 6.7. In this configuration, the sensitivity indices are different. The total effect indices of brain and scalp conductivities are important, whereas the total effect of skull conductivity is lower, see tables 6.7 and 6.8. It means that there is more interaction between scalp and brain conductivities than between scalp and skull conductivities. Furthermore, the interaction is more complicated as it involves the three conductivities, and we were not able to find the structure of this interaction. Still, considering the importance of the interaction between scalp and brain conductivities, we believe that the scalp/skull ratio is not the quantity of choice to be estimated with EIT, although it was done in several previous studies [78, 37].

More recent methods for conductivity calibration use focal evoked activity in the cortex [37, 7, 38, 101, 59]. A simple somatosensory stimulus such as a median nerve stimulation is presented to the subject, producing a focal activity in the somatosensory cortex at short latency (20 ms). This focal activity can be well modeled by a single dipole. Then, assuming more or less priors on the dipole location, the conductivities can be calibrated by matching the simulated potential given by the EEG forward model with the evoked potential computed from the real EEG data. With this source configuration, the topography of the simulated potential is indeed sensitive to the scalp/skull conductivity ratio, and so this method is more appropriate than

S_1	S_2	S_3	S_{T_1}	S_{T_2}	S_{T_3}
0.00	0.94	0.00	0.04	0.99	0.01

Table 6.9: Sensitivity indices for a shallow dipole in a three-layer realistic EEG model. The parameters x_1, x_2, x_3 are the skull/brain ratio, scalp/skull ratio and scalp conductivity. All the parameters are varied of $\pm$50% with the following nominal values : $\frac{1}{50}$ for skull/brain ratio, 50 for scalp/skull ratio and 1 for scalp conductivity.

S_1	S_2	S_3	S_4	S_{T_1}	S_{T_2}	S_{T_3}	S_{T_4}
0.17	0.00	0.69	0.00	0.28	0.03	0.82	0.01

Table 6.10: Sensitivity indices for a shallow dipole in a four-layer realistic EEG model. The parameters x_1, x_2, x_3, x_4 are the CSF/brain ratio, skull/CSF ratio, scalp/skull ratio and scalp conductivity. All the parameters are varied of $\pm$50% with the following nominal values : 5 for CSF/brain ratio, $\frac{1}{250}$ for skull/CSF ratio, 50 for scalp/skull ratio and 1 for scalp conductivity.

EIT if the final goal is to calibrate the EEG forward model for source localization. To illustrate this, we refer to chapter 7, section 3.3 where are shown some results of conductivity calibration based on real data from an experiment with median nerve stimulation.

5 CONCLUSION

The aim of this chapter was to present a global sensitivity analysis of the three-layer EEG forward models, with respect to the conductivity parameters. We analyzed the impact of the conductivities on the topographic distribution of the electric potential at the sensors. By using a variance-based method for the sensitivity analysis, we were able to quantify precisely the effect of each conductivity parameter, and also the effect of parameters together, which is referred to as interaction. For a shallow dipole and a three-layer head model, it appears that almost all the effect of conductivity parameters on the potential topography is driven by the skull and scalp conductivities. As a consequence, it is crucial to develop accurate models of these two tissues. Also, skull and scalp conductivities have a high interaction, meaning they have a joint effect on the potential topography. The quantity responsible for this interaction appears to be the ratio between scalp and skull conductivities. This means that the value of this ratio is very important in determining the potential shape. That is why the calibration of EEG forward models should focus on estimating this quantity. Our sensitivity analysis also reveals that the electrical impedance tomography (EIT) is not adapted for such an estimation, and that calibration methods based on evoked potentials are better suited for this purpose.

CHAPTER 7

CONDUCTIVITY CALIBRATION WITH SOMATOSENSORY EVOKED POTENTIALS

A new method for *in vivo* conductivity estimation of head tissues is proposed. Unlike classical electrical impedance tomography methods, for which the conductivity is inferred from a current injection on the scalp, we use an evoked source inside the brain that comes from a somatosensory experiment. The resulting uncertainty with respect to the source is then balanced by strong constraints : we assume the source to be a single dipole located in the somatosensory cortex, with orientation normal to the cortical surface. Using only EEG data, we are then able to estimate conductivity values, using the MUSIC method to recover the position of the source. The applicability of the method is demonstrated on simulations and on real data.

Contents

1 INTRODUCTION

As explained in chapter 3, section 6, a problem with EEG is its sensitivity to electrical properties of head tissues. In particular, the bad knowledge of skull conductivity can greatly affect the EEG source localization [49]. Further, it is known that the skull conductivity can vary highly, depending on the subjects, but also for the same subject depending on his age. For the purpose of better source estimation, it is hence essential to be able to calibrate *in vivo* the conductivities of the EEG forward models.

The main approach taken to achieve conductivity estimation is electrical impedance tomography (EIT), in which a low-intensity current is imposed on the scalp through selected EEG electrodes, and conductivity values are then inferred from potential measurements at the remaining electrodes [27, 78, 37]. The results of the sensitivity analysis presented in chapter 6 show that with this modality, the EEG topographies have a different sensitivity to the conductivities than when considering an electric source in the brain. As a consequence, if the EEG forward model is used for source localization, it can be better calibrated with a source inside the brain.

Nevertheless, several problems arise when considering the calibration of the conductivities with a brain source instead of a scalp current injection :

- With EIT, the source is artificial : a current is injected on the scalp. Putting an artificial source in the subject's brain would be of course very invasive, so we need to consider a natural brain source, generated by a stimulus presented to the subject.

- With EIT, the source is completely known : its position is given by the injection electrodes, and its intensity is controlled by an amplifier. For a brain source generated by a stimulus, we have less knowledge. We can still have a strong a priori on certain parameters of the source by using well-understood stimuli. For instance, a classical somato-sensory experiment is to use an electric stimulation of the median nerve, localized at the wrist, which is known to produce a very focal brain response in the posterior wall of the central sulcus at 20 ms. For such a stimulus, we can put constraints on the source position by using a segmentation of the cortical surface from an MRI of the subject.

Most of the previous approaches for conductivity calibration with a brain source used a combination of EEG and MEG measurements [37, 7, 38]. In this case, the brain source is first localized using the MEG measurements, then the source location is fixed in the EEG forward model and the conductivities are calibrated using the EEG measurements. The method principle is correct, but it is very likely that if an MEG is available at the same time then the use of EEG is not necessary (unless for combined EEG-MEG source localization). Most of the time, EEG is used alone, or in combination with fMRI, and in this case it would be worthwhile to calibrate the conductivities of the EEG forward model without MEG.

In this chapter, we thus propose a method to calibrate the conductivities with a brain source, with only EEG. Such an approach has been briefly considered before in [38], but without constraint on the source, which we demonstrate to have poor robustness to noise. In our method, we use median nerve stimulation and a cortical surface obtained from MRI segementation to constrain both the localization and

orientation of the source. It allows us to define a very restrictive source space, and we perform the source localization in this source space. Such constraints on the source lead to a source localization almost independent on the conductivities, and so we can perform the conductivity calibration as if the source was fixed. We present results of the method applied to both simulated and real data.

2 METHOD

2.1 EEG forward model

We consider the electric potential V which satisfies, inside the head volume Ω with conductivity σ, the following PDE :

$$\begin{cases} \nabla \cdot (\sigma \nabla V) = \nabla \cdot \mathbf{J}^{\mathrm{p}} & in \quad \Omega \\ \sigma \nabla V \cdot \mathbf{n} = 0 & on \quad \partial\Omega \end{cases},$$

where $\mathbf{J}^{\mathrm{p}}$ represents the sources inside the brain. For the moment we do not assume any conductivity model and we suppose that we are able to compute the potential V for any given σ and $\mathbf{J}^{\mathrm{p}}$.

2.2 Source model

We suppose that we presented the subject with a median nerve stimulation, and that we want to localize the brain source corresponding to the evoked potential at 20 ms. This evoked source is supposed to be localized in the somato-sensory cortex, on the posterior wall of the central sulcus [45], and more important it is considered to be a very focal source. As a consequence, we will model the source as a single dipole. It corresponds well to a focal activity, and has the advantage of being defined by a few parameters, which in our case is important because we want as few source parameters as possible to remain unknown.

2.3 Source space

Usually, when doing single dipole localization, the dipole is allowed to move in the whole head domain. Here we want to use the a priori information about the source location, i.e. constrain the dipole position to the somato-sensory cortex. This can be done by using a cortical surface segmented from an anatomical MRI of the subject. Many toolboxes are available (Brainvisa, Brainsuite, Freesurfer) and can provide a mesh describing the cortical surface. Usually, this cortical surface corresponds to the grey/white matter interface, but sometimes it is also possible to get an estimate of layer IV of the cortical sheet. We rather use this surface as most of the pyramidal neurons are in layers III and V of the cortex. So we chose to use Freesurfer [19] which can provide an estimate of the layer IV of the cortical sheet, thus giving a good approximation of the real positions of the sources. It is then possible to extract the part of this mesh corresponding to the somato-sensory cortex using automatic labeling (see figure 7.1). Once we have a mesh of the somato-sensory cortex, it is

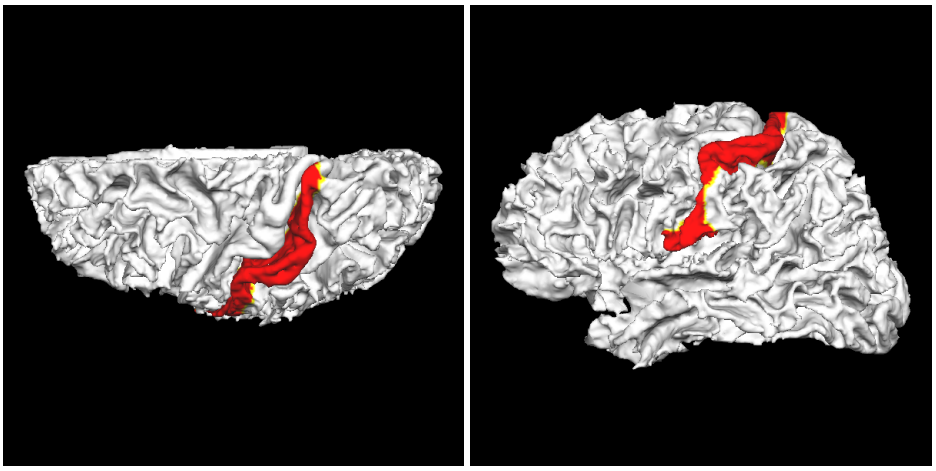

Figure 7.1: The cortical surface can be clustered in different areas. For our application, we keep the area corresponding to the post-central gyrus.

easy to constrain the dipole position : we use the mesh vertices as the only possible locations for the dipole. We are then given a finite set of positions that define a discretized source space. The dipole can be even more constrained by assuming that its moment is normal to the cortical surface. In this case we are left with only two unknowns for the source : its amplitude and at what mesh vertex it is located. It is possible to use interpolation between the mesh vertices so as to have a continuous description of the cortical surface, but this is not necessary since the meshes produced by the segmentation tools are very fine. To give an idea, a mesh describing precisely the somatosensory cortex contains about 10^5 vertices.

2.4 Single dipole localization on the cortical surface

Because we consider a discretized source space, it is very convenient to use a scanning method, like MUSIC or beamformers, to localize a single dipole. To give an example, we describe the source localization with the MUSIC method, but it can be directly transposed to any beamforming method.

We assume that we have built a gain matrix for our EEG forward model with a given conductivity σ, projecting all the dipoles previously defined on the electrodes. For a dipole at a cortical mesh vertex i, we denote g_i the column of the gain matrix corresponding to this dipole, also called gain field.

Now we consider the EEG measurement data M, which is an $n \times m$ matrix, where n is the number of electrodes and m is the number of time samples. Let $M = USV$ be the singular value decomposition of M. For the MUSIC method, we define a signal subspace and a noise subspace. Here, in the case of a single source, the signal subspace is spanned by the first left singular vector in U, call it u_1, and $P = I - u_1 u_1^T$ is the orthogonal projector on the noise subspace.

Next we can define a cost function with respect to the cortical mesh vertices :

$$J(i) = \frac{\|Pg_i\|^2}{\|g_i\|^2}. \tag{7.1}$$

When $J(i)$ is close to zero, this corresponds to most of the gain field g_i being in the signal subspace, in which case there is a high likelihood for there to be a source located at vertex i. In our case of a single dipole, the estimated source position is given by the vertex where J achieves its minimum.

2.5 Definition of a cost function for conductivities

For a given conductivity distribution σ, we are able to find the most probable location of the dipole source within the set of cortical mesh vertices, given by the minimum of J. Let us index the gain field of this "optimal" dipole by the conductivity σ, denoting g_σ. We can hence define a cost function for the conductivity by quantifying the error between this gain field and the measurements. One possible choice is to compute a global RDM between the gain field and the measurements :

$$E(\sigma) = \frac{1}{m}\sum_{i=1}^{m} RDM(M_i, g_\sigma) = \frac{1}{m}\sum_{i=1}^{m} \left\| \frac{M_i}{\|M_i\|} - \frac{g_\sigma}{\|g_\sigma\|} \right\| \ ,$$

where $\|\cdot\|$ is the discrete l^2-norm, M_i is the vector of measurements at time sample i and m is the number of time samples. In our case, we use the MUSIC method which extracts a signal subspace from the measurements so as to limit the effect of noise, hence it seems better to compare the gain field of the optimal dipole with the signal subspace. We rather use the following cost function :

$$E(\sigma) = RDM(u_1, g_\sigma) = \left\| \frac{u_1}{\|u_1\|} - \frac{g_\sigma}{\|g_\sigma\|} \right\| \ , \tag{7.2}$$

where u_1 is the first left singular vector of the measurements. This represents the topographic error between the data and the gain field of the best dipole location. The minimum of this cost function corresponds to the conductivity distribution which gives the best topographic match with the measured scalp potentials. It is important to note that each evaluation of $E(\sigma)$ requires to generate a new gain matrix with the corresponding conductivity σ. Depending on the method used to compute the gain matrix, this can be more or less expensive, and so this will impact the number of different conductivity distributions that can be considered.

An important point to note is that the absolute values of the conductivity cannot be determined by this way. To illustrate this point, let us consider two conductivity distributions σ_1 and σ_2 such that $\sigma_2 = \lambda\sigma_1$ where λ is a scalar. Then, for a given dipole, the corresponding gain fields are such that $g_{\sigma_2} = \frac{1}{\lambda} g_{\sigma_1}$. As a consequence, considering the formula of E (7.2), we have $E_{\sigma_1} = E_{\sigma_2}$, and so the two conductivity distributions cannot be distinguished. It means that the minimum of the cost function E is non unique, and one has to fix the global amplitude of the conductivity distibution for the problem to have a unique solution. In other words, it is only possible to determine the relative variations of the conductivity distribution.

3 EXPERIMENTAL RESULTS

3.1 Head model

All the following results are shown for a three-layer model with realistic geometry. This model was built from a T1 MRI of a subject who participated in a somatosensory experiment. The skull segmentation was first obtained automatically using Brainvisa, and then corrected manually so that it best matches with the MRI. The EEG electrode positions of the model were obtained from the registration of the 64 electrode positions recorded during the somatosensory experiment. A mesh of the grey-white matter interface was obtained using Freesurfer, and the somato-sensory cortex was automatically extracted using the labelling of the main brain areas.

3.2 Simulations and robustness to noise

To test the method, we considered the estimation of the scalp/skull conductivity ratio, as the sensitivity analysis of chapter 6 has shown that the EEG topographies are mainly sensitivite to this quantity. Hence, we fixed both brain and scalp conductivities to 1, and we sampled the skull conductivity from 0.01 to 0.03 with a step of 0.002. It gives eleven different conductivity distributions, with a scalp/skull ratio varying between 33 and 100. For each of these conductivity distributions, we computed the corresponding lead field using the FEM method described in chapter 4. The nominal scalp/skull ratio was chosen to be 50, and we evaluated the capacity of the method to estimate this ratio among the other sampled values.

We produced simulations of EEG data which resemble SEP. We chose a vertex of the cortex mesh located on the posterior wall of the central sulcus, thus giving a position $\mathbf{r}_0$ and an orientation $\mathbf{q}$ defining a dipole. To simulate the short latency response to a median nerve stimulation, we modulated the gain field of this dipole with 10 samples of a half sine wave period. This corresponds to what can be recorded during 2 ms at a sampling rate of 5 kHz. As explained, the nominal value for the scalp/skull ratio is chosen to be 50, so the EEG simulations were generated with the dipole gain field at this conductivity.

First, we tested the robustness of the method to the noise at the sensors. Because we consider evoked potentials which are generated from between 500 and 1000 single trials, we can first assume that the noise average is a Gaussian noise (due to the central limit theorem). We thus generated 100 realizations of a white Gaussian noise that we added to the EEG simulation described above. This was done for four different SNR : 50, 10, 5, 2. The method was then applied on these noisy SEP simulations, giving an estimate of the scalp/skull conductivity ratio as the minimum of E among the different conductivity samples. These estimates are shown as boxplots on figure 7.2. These are classical boxplots corresponding to the smallest observation, lower quartile ($Q1$), median, upper quartile ($Q3$), and largest observation. The box outlines the lower and upper quartiles, and the stars indicate possible outliers. Outliers are defined as any points larger than $Q3+1.5*IQR$ or lower than $Q1-1.5*IQR$, where IQR is the inter quartile range defined as $IQR = Q3-Q1$. Even for low SNR, the method can recover the scalp/skull ratio with good accuracy. This is mainly due to the fact that in this ideal situation with white Gaussian noise, the SVD performed by the MUSIC method is able to remove almost all the noise from the simulations. Actually, assuming a white Gaussian noise at the sensors is not very realistic : even if the average is Gaussian, it is known that close sensors are not completely uncorrelated. To test our method with real noise, we generated many average of real EEG

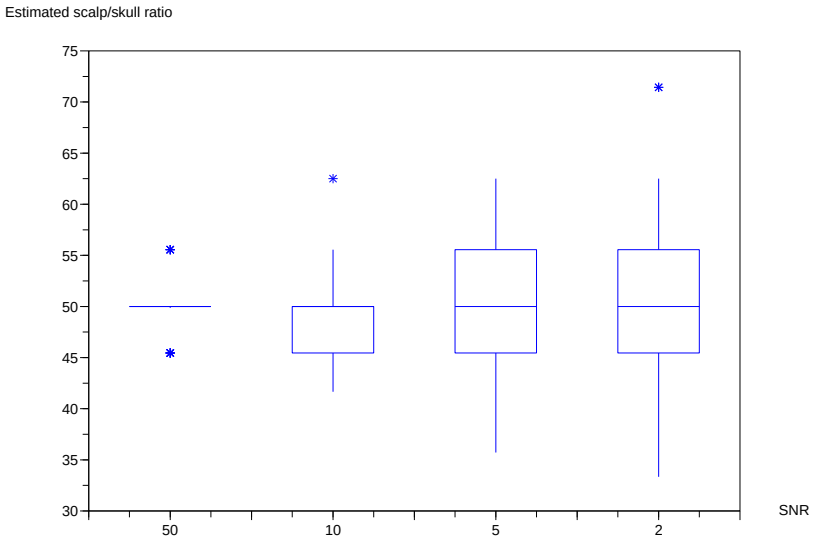

Figure 7.2: Boxplots of the estimated scalp/skull conductivity ratio, with respect to the different levels of SNR (white Gaussian noise).

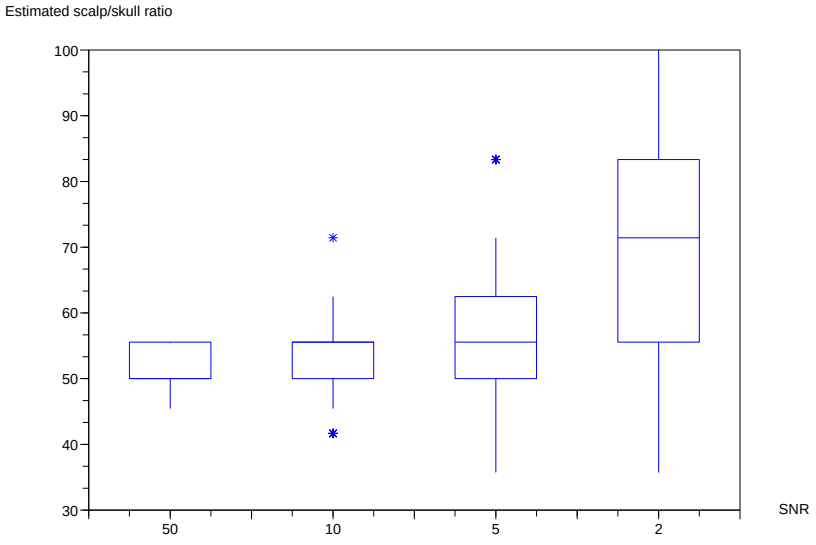

Figure 7.3: Boxplots of the estimated scalp/skull conductivity ratio, with respect to the different levels of SNR (realistic noise).

measurements during a prestimulus period that is usually considered as a baseline for evoked activity. We used a somatosensory experiment with more than 600 trials, and we generated 100 different average noises by bootstrapping the trials (random sampling with replacement). The results of the method in presence of realistic noise are presented in figure 7.3. The results are not as accurate as with white Gaussian noise, but the estimates are still good for a reasonable amount of noise (SNR=10)

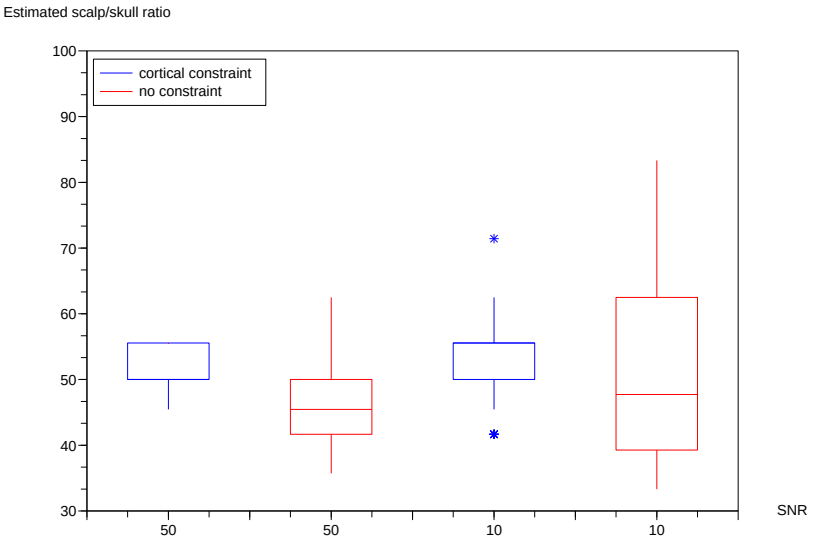

Figure 7.4: Boxplots of the estimated scalp/skull conductivity ratio, with and without cortical constraint (realistic noise).

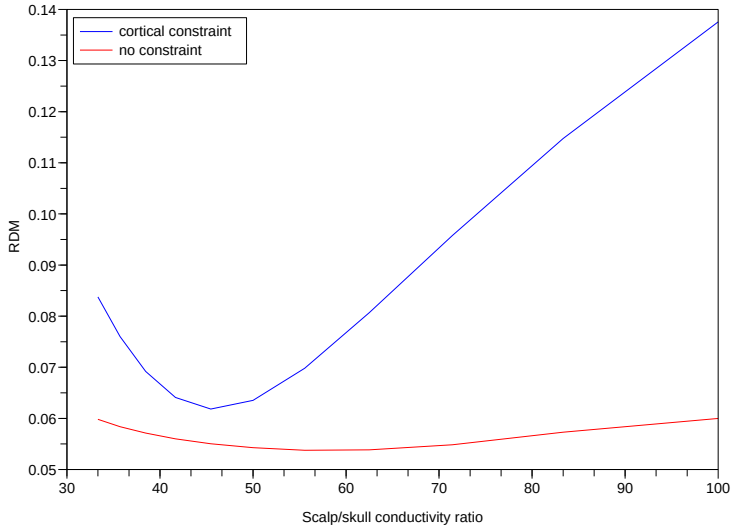

Figure 7.5: Plots of $E = RDM(u_1, g_\sigma)$ with respect to the scalp/skull conductivity ratio, with and without the cortical constraint. The minimas of the two curves does not match because they correspond to two different noise realizations (SNR=10).

which can be obtained with a sufficient number of trials. To illustrate the importance of the cortical constraint on the source, we did the same experiment without the constraint. It means that, for each conductivity sample, a MUSIC localization is performed in the whole head space. We show on figure 7.4 the boxplots at a SNR of 50 and 10, with and without the constraints. It clearly shows that the method fails

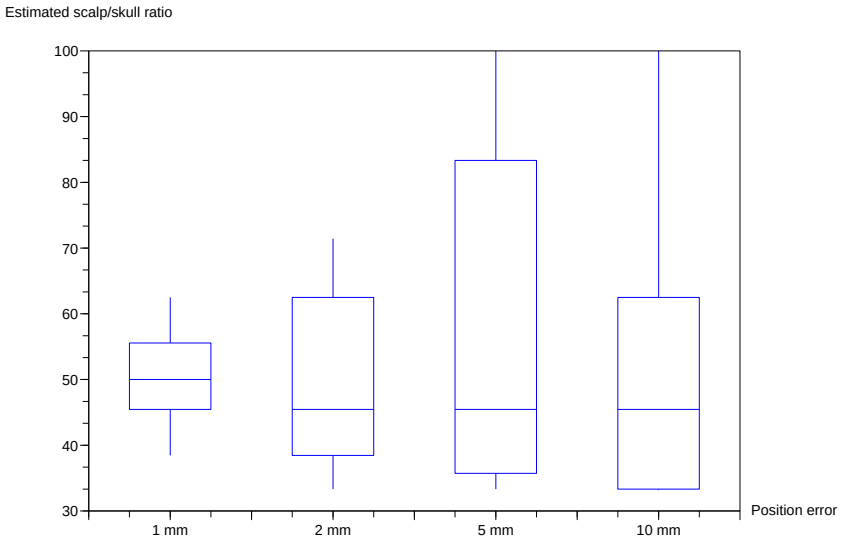

Figure 7.6: Boxplots of the estimated scalp/skull conductivity ratio, with respect to the source position error.

to recover a good estimate if the source position is not constrained. To give further insight, we plotted on figure 7.5 two curves of E with and without the constraint, for two different noise realizations at a SNR of 10. Without the cortical constraint, the curve of E is very flat, because for each conductivity sample the source localization finds a different dipole position that has a very good match with the measurements. On the contrary, when the source is constrained to the cortical surface, the discrepancy between the conductivity samples is far better. Because E has a flat profile without the source constraint, the position of its minimum is very sensitive to the noise, and in this case the method is not robust.

We also tested the robustness of the method to the errors in the cortical segmentation. Actually, the anatomical MRI that we used has a 1 mm resolution, so the location of the cortical surface is subject to errors of the mm order. Second, we constrain the source to a surface which is an estimate of the layer IV of the grey matter, which is not necessarily the real location of the sources. Most of the pyramidal neurons are located in layers III and V of the grey matter, and their apical dendrite can extend more or less towards upper layers. Also, the thickness of the grey matter varies between 3 mm and 6 mm, and the grey and white matter surfaces are not necessarily parallel, so the dendrites of the pyramidal neurons are not necessarily perfectly perpendicular to the cortical surface that we use. As a consequence, a real brain source does not necessarily have its centroid located exactly on the segmented cortical surface, and its global moment is not necessarily perpendicular to the cortical surface. We thus generated other EEG simulations where the dipole that we first chose on the cortical mesh was randomly modified. We first moved only its position : we generated 100 random vectors sampling the surface of a sphere with fixed radius, and add these vectors to the position of the dipole. This was done for four radii of 1 mm, 2 mm, 5 mm and 10 mm. The boxplots of the estimated conductivity are shown on figure 7.6. Similarly, we changed only the moment of the dipole : we

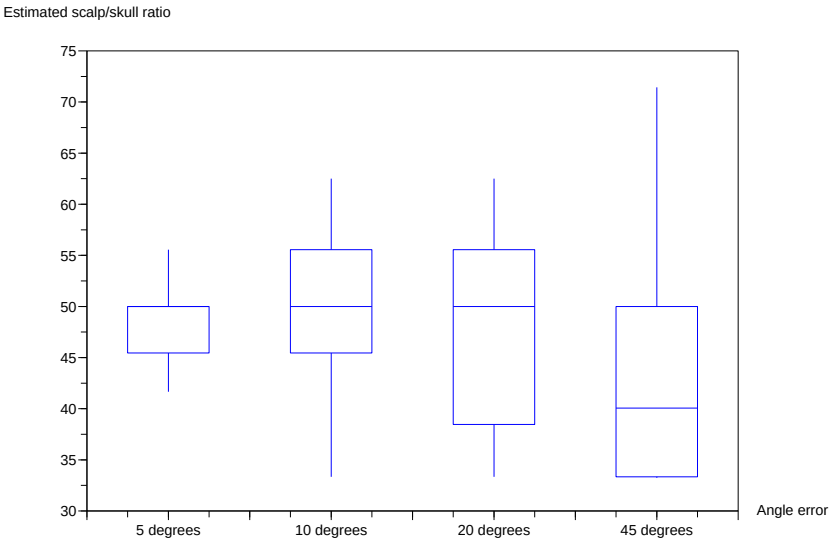

Figure 7.7: Boxplots of the estimated scalp/skull conductivity ratio, with respect to the source moment error.

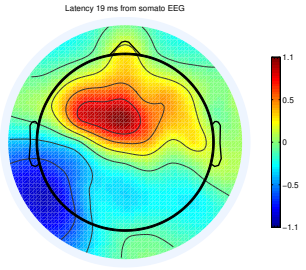

Figure 7.8: The evoked potential is shown 20 ms after the stimulus (top view of the sensors on the subject's head). The nice dipolar strucutre of the potential topography shows the validity of the single dipole model.

generated 100 different vectors on the surface of a cone with a certain angle, where the axis of the cone is the original dipole moment. This was done for four angles (in degrees) : 5, 10, 20 and 45. The results of the estimation are shown on figure 7.7. It appears that the estimation is very sensitivite to the error on the source position and moment. The results show that the method can reasonably be applied only if the real source is located less than 2 mm away of the segmented cortical surface and the angle error is less than 10 degrees.

3.3 Real data

The method was also applied on real data coming from a somatosensory experiment with median nerve stimulation. The data was recorded at Hopital la Timone (Marseille, France), with a 64-channel EEG helmet. An electrical stimulator was positioned on the subject's wrist, and the intensity of the current was chosen according

to the sensitivity threshold of the subject, i.e. when the stimulation produced movement of the thumb (around 10 mA). The stimulation was repeated at a frequency of 5 Hz while the potential was sampled at 5 kHz. We then averaged the data over about 500 artifact-free trials to obtain the N20 somatosensory evoked potentials (figure 7.8).

For this experiment, we computed several gain matrices for different conductivity distributions. These conductivity distributions were generated by sampling each conductivity of each layer independently, while the others were fixed to nominal values of 1, 0.02, 1 for brain, skull, scalp respectively. For each of these conductivity distributions, we computed the value of the cost function E. Because we sampled each conductivity independently, what we got is the variation of $E = RDM(u_1, g_\sigma)$ with respect to each conductivity. We thus show on figure 7.9 a plot of the RDM with respect to the variation of each conductivity. We can see that the curves which show the highest variability of the RDM (between 21% and 29%) are the ones corresponding to the variations of the skull and scalp conductivities. The variation of the brain conductivity only makes the RDM vary between 24% and 26%, despite a large range of variation (the brain conductivity was varied from 0.3 to 10). Also, for skull and scalp, the minima both correspond to a RDM of 21%, for values of 0.009 and 2.5 respectively, which gives a scalp/skull ratio of $\frac{1}{0.009} = 111$ and $\frac{2.5}{0.02} = 125$ (relatively to the nominal values). The fact that the two minima give the same RDM and a similar scalp/skull ratio confirms the relevance of the quantity $\frac{\sigma_{scalp}}{\sigma_{skull}}$. Actually, because the interaction of skull and scalp conductivity is so high, it would be impossible to estimate both, and only their ratio can be estimated. So with this method using a somatosensory evoked potential, and for a three-layer model, the calibration can be done either by estimating the skull conductivity or the scalp conductivity, because both can provide an estimate of the scalp/skull ratio.

4 CONCLUSION

We have presented a new approach for conductivity estimation, using an evoked source in the somatosensory cortex and only EEG measurements. The source is localized by scanning the vertices of a mesh describing the somatosensory cortex. With this constraint, the source localization is very robust to the choice of conductivity : it is as if the source was fixed, which in return makes the conductivity estimation possible. We showed the applicability of this method on both simulated and real data, for the estimation of the scalp/skull conductivity ratio in a three-layer model. The main weakness of the method seems to be its strong dependency on the quality of the mesh describing the cortex. Yet we can argue that the accuracy given by a T1 MRI (a few mm) is comparable to the accuracy of a source localization with MEG. Hence it is unlikely that the conductivity estimation with combined EEG-MEG measurements [37, 7, 38] would give better results than our approach using only EEG.

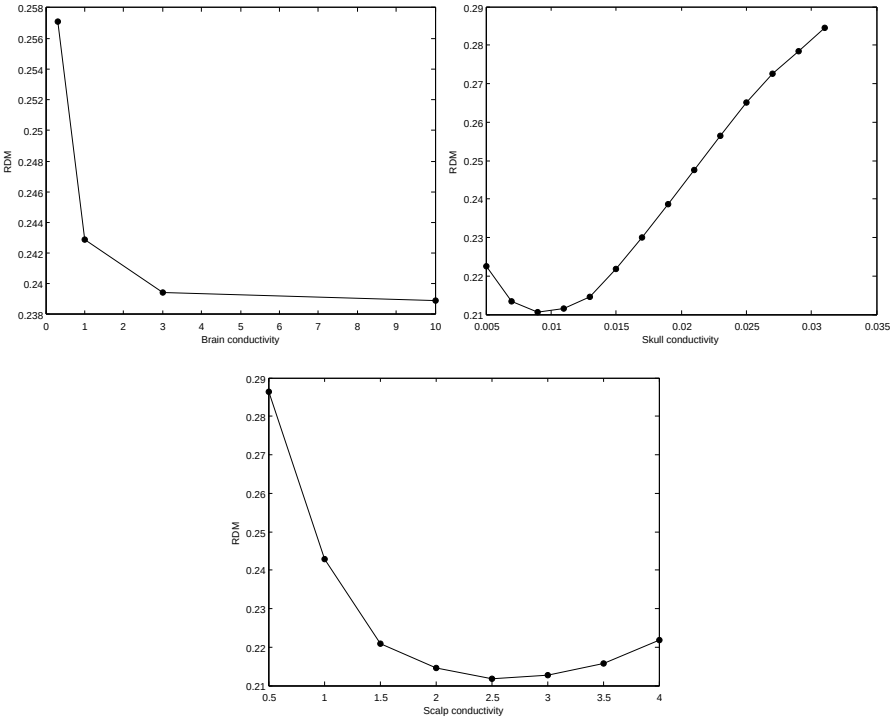

Figure 7.9: RDM between the N20 SEP and the simulated potential given by the forward model with respect to conductivity variations : brain conductivity, skull conductivity, scalp conductivity. For each conductivity variation, the other conductivities are fixed to their nominal values : 1, 0.02, 1 for brain, skull and scalp respectively.

Conclusion and perspectives

Summary and main contributions

The development of the forward EEG and MEG models towards more realism is linked to the development of the structural imaging techniques of the body. With the use of high-fields MRI scanners ($3T$) and new modalities (DT-MRI), it is possible to get very complex descriptions of the human head tissues. Solving the PDEs of the electromagnetic field in such geometries requires the use of volume-discretization methods, such as the FDM, FEM, or FVM. All these methods have in common a high computational cost, which is more or less important depending on the accuracy of the method. The work we presented in part I aims at lowering this cost while keeping a good accuracy. The FEM method introduced in chapter 4 just requires a cubic mesh and yet is able to handle complex domains by using levelsets representations. It requires very little user interaction, and its memory and computational costs are reasonable. It thus allows to run simulations in high resolution realistic geometries on an everyday desktop or laptop computer. In chapter 5, we extended the reciprocal PDEs from pointlike sensors to non-pointlike sensors, thus decreasing the number of computations needed to build a gain matrix in the case of complex sensors (e.g. first or second order gradiometers).

The accuracy of the forward EEG models also depends strongly on the choice of efficient conductivities. Although some methods exist for *in vivo* conductivity estimation (EIT, MREIT), it is not clear how well they can perform for the calibration of an EEG forward model which is used for brain source localization. The part II is a study of the problem of conductivity calibration. To better understand the forward EEG models and their sensitivity to the conductivities, we presented in chapter 6 a global sensitivity analysis of the EEG topographies in the most common models (three-four layers). The two main results are :

- For a source in the brain, the EEG topographies are mostly sensitive to skull and scalp conductivities, especially to the value of their ratio.
- The sensitivity of the EEG topographies to the conductivities is different whether the electric source is in the brain or at the scalp surface.

As a consequence, it seems important to focus on the calibration of the value of the scalp/skull conductivity ratio, and a configuration where the source is located in the brain appears to be the best for estimating this quantity. Following these results, we proposed in chapter 7 a method for the calibration of the conductivities with a brain source. We showed on simulations the capacity of the method to give a good estimate of the scalp/skull conductivity ratio, and its applicability to real data.

Perspectives

The methods presented in this thesis have possible applications or extensions. Some of them are projects for the future while others are concrete or already ongoing.

Improve and make available the implicit FEM. As explained in the conclusion of chapter 4, the implicit FEM has less control on the solution at the interfaces than the tetrahedral FEM. Actually, in the Implicit FEM, the solution is approximated by a piecewise trilinear function, which is trilinear in each voxel. For a voxel crossing an interface, the approximated solution and its derivative are hence continuous through the interface. For the real solution, there must be continuity of the

potential and the flux through the interface, which means that the normal derivative of the potential is discontinuous at an interface. As a consequence, the quality of the approximation can be improved if for the crossing voxels we consider local basis functions for which the normal derivative is also discontinuous at the interface. This kind of approach is called the Immersed Finite Element Method, and has been previously developed for Q1 elements in the 2d case [47], giving a convergence rate of $\mathcal{O}(\frac{1}{h^2})$. We are currently working on a possible extension to the 3d case.

The code of the Implicit FEM (chapter 4) is written in C++, and is developed under Linux. For the moment it is still in a development state, but it is planned to produce a stable release that can be distributed.

Sensitivity analyses of complex EEG forward models. The variance-based sensitivity analysis of the forward EEG models (chapter 6) has been done only for models with three or four scalar conductivity parameters. It would be interesting to carry the same sensitivity analysis on more refined models which describe many different tissues. It is now possible to build models with up to 11 different scalar parameters [83]. The interest of such an analysis would be to identify which parameters are non-influent so that they can be fixed to an average value without affecting the output of the model. If many parameters were (almost) non-influent, then only a few remaining parameters would need to be estimated, which would make the estimation possible. The drawback of the variance-based methods is their computational cost, as they require many calculations of the model to give reliable estimates. For a forward EEG model with 10 or more conductivity parameters, applying a variance-based method would require too many sample points of the parameter space to be possible. Nevertheless, another approach called the elementary effects method [68] could be applied in this case, as it requires a very small sampling size, but at the price that the sensitivity indices hold less information.

Statistical study of the conductivity calibration on real data. The method for conductivity calibration described in chapter 7 will be used as part of an INSERM experimental protocol starting in fall 2008 at the hospital La Timone (Marseille, France). This experiment will involve 30 subjects with a drug-resistant epilepsy who are waiting for a presurgical sEEG exploration (implantation of depth electrodes). For each subject, the conductivities of a realistic EEG model will be calibrated both with EIT and with SEP. Then some source localization methods will be performed on EEG recordings of interictal spikes, both with standard and calibrated conductivity values. The aim of the study is to compare the results of the source localizations with and without conductivity calibration, and also later with the finer localizations given by the depth electrodes. This study is particularly interesting as the subjects will be mostly children and teenagers for whom the skull tissue is not mature yet, and hence have a very variable conductivity.

Conclusion et perspectives

Résumé et principales contributions

Le réalisme toujours plus poussé des modèles directs EEG et MEG est fortement lié au développement des techniques d'imagerie structurelle du corps humain. Avec l'utilisation de scanners IRM à haut champ ($3T$) et l'apparition de nouvelles modalités (DT-MRI), il est possible de construire des descriptions très complexes des tissus composant la tête. Pour résoudre les EDP du champ électromagnétique dans de telles géométries, il est nécessaire d'utiliser des méthodes de discrétisation volumique telles que les différences finies, les éléments finis ou les volumes finis. Toutes ces méthodes ont le désavantage de présenter un coût computationnel élevé, plus ou moins important selon la précision de la méthode. Les travaux que nous avont présentés dans la première partie de cette thèse ont pour but de réduire ce coût computationnel tout en gardant une bonne précision. La méthode éléments finis exposée au chapitre 4 est basée sur un maillage Cartésien, simple à mettre en oeuvre, et cependant est capable de traiter avec précision des géométries complexes par l'emploi de fonctions implicites. Cette méthode requiert très peu d'intervention de la part de l'utilisateur, et ses coûts en temps et en mémoire restent limités. Cette méthode permet donc de produire des simulations EEG et MEG dans des géométries réalistes à haute résolution sur n'importe quel ordinateur personnel courant. Dans le chapitre 5, nous avons étendus les EDP réciproques utilisées en EEG et MEG afin de prendre en compte l'utilisation de capteurs non ponctuels. Typiquement, cela permet de réduire notablement le coût computationnel des simulations lorsque des capteurs complexes sont simulés (par exemple les gradiomètres de premier et second ordre).

La précision des modèles directs EEG dépend également fortement du choix des valeurs de conductivité qui sont affectées au modèle. Bien que certaines méthodes soient développées afin d'estimer *in vivo* les valeurs de conductivité, il n'est toujours pas clair qu'elles puissent véritablement être efficaces pour la calibration de modèles direct EEG utilisés pour la localisation de sources. Dans la seconde partie de cette thèse, nous avons étudié ce problème de calibration de conductivités. Dans un premier temps, afin de mieux comprendre la sensibilité de ces modèles aux paramètres de conductivité, nous avons effectué au chapitre 6 une analyse de sensibilité pour les modèles les plus couramment utilisés (trois ou quatre couches). Les deux résultats principaux sont les suivants :

- Pour une source située dans le cerveau, les topographies EEG sont principalement sensibles aux conductivités du crâne et du scalp, surtout à la valeur de leur ratio.

- La sensibilité des topographies EEG aux conductivités est différente selon que la source électrique est située dans le cerveau ou à la surface du scalp.

Par conséquent, il nous semble important de se concentrer sur la calibration du ratio de conductivité scalp/crâne, et une configuration dans laquelle la source est située dans le cerveau semble être la meilleure pour l'estimation de cette quantité. Prenant en compte ces résultats, nous avons proposé au chapitre 7 une méthode pour la calibration de conductivtés utilisant une source située dans le cerveau. Les résultats de cette méthode sur différents jeux de simulation ainsi que sur des données réelles ont montré sa capacité à estimer le ratio de conductivté scalp/crâne.

Perspectives

Les méthodes que nous avons présentées dans cette thèse ont de possibles applications et extensions. Certaines sont au stade de projet mais d'autres sont déjà des travaux en cours.

Améliorer et rendre disponible la FEM implicite Comme expliqué en conclusion du chapitre 4, la FEM implicite a moins de contrôle sur la solution au niveau des interfaces que la FEM tétrahedrique. En effet, avec la FEM implicite, la solution est approchée par une fonction trilinéaire par morceaux, qui est trilinéaire dans chaque voxel. Ainsi, pour un voxel coupé par une interface, l'approximation de la solution est continue à travers l'interface, et il en est de même pour sa dérivée. Pourtant, la solution réelle doit vérifier des conditions de saut qui imposent la continuité du potentiel et du flux à travers les interfaces. Cela signifie en particulier que la dérivée normale du potentiel est discontinue au niveau d'une interface. Par conséquent, il est possible d'améliorer la qualité de l'approximation de la solution en modifiant les fonctions de base au niveau des voxels coupés, et en utilisant des fonctions dont la dérivée normale est discontinue au niveau de l'interface. Ce type d'approche est connue sous le nom d'éléments finis immergés, et a été précédemment développée pour des éléments bilinéaires dans le cas 2d [47], avec un taux de convergence en $\mathcal{O}(\frac{1}{h^2})$. Nous travaillons actuellement sur une possible extension au cas 3d.

Le code de la FEM implicite est écrit en C++ et développé sous Linux. Pour le moment il est toujours dans un stade de développement mais le but à terme est de produire une version stable qui puisse être distribuée.

Analyse de sensibilité de modèles directs EEG complexes L'analyse de sensibilité basée sur la variance que nous avons effectuée pour les modèles directs EEG (chapitre 6) s'est restreinte aux modèles avec au plus quatre paramètres de conductivité. Il serait intéressant de mener le même genre d'analyses sur des modèles plus raffinés qui décrivent beaucoup plus de tissus différents. Il est actuellement possible de construire des modèles qui peuvent comporter jusqu'à 11 paramètres de conductivité [83]. L'intérêt d'une telle analyse est d'identifier quels sont les paramètres qui sont très peu influents, afin de pouvoir en connaissance de cause leur affecter une valeur moyenne tout en sachant que le modèle n'en sera pas affecté. Si beaucoup de paramètres étaient non influents, il serait même possible d'envisager l'estimation du peu de paramètres restants. Le problème des méthodes basées sur la variance est leur coût computationnel, puisqu'un grand nombre de simulations du modèle sont nécessaires pour obtenir des estimations raisonnables. Pour un modèle direct EEG comportant 10 paramètres de conductivité ou plus, l'utilisation d'une méthode basée sur la variance nécessiterait de considérer un bien trop grand nombre de simulations pour être applicable. Néanmoins, d'autres méthodes d'analyse de sensibilité sont possibles, comme celle des effets élémentaires [68], et peuvent être utilisées dans ce cas car elles recquièrent un nombre de simulations beaucoup plus faible, au prix cependant d'une analyse de sensibilité moins performante.

Etude statistique des calibrations de conductivité sur données réelles La méthode pour la calibration de conductivité présentée au chapitre 7 va être utilisée au sein d'un protocole expérimental de l'INSERM qui commencera à l'automne 2008 à l'hopitâl de La Timone à Marseille. Cette expérience sera menée sur trente sujets

au total, qui présentent une épilepsie partielle pharmaco-résistante et qui sont en attente d'une exploration SEEG préchirurgicale (implantation d'électrodes dans le cerveau). Pour chaque sujet, les conductivités d'un modèle EEG à géométrie réaliste seront calibrées, à la fois par EIT et par la méthode utilisant les PES. Ensuite des méthodes de localisation de sources seront appliquées sur des enregistrements de pointes intercritiques, à la fois avec des valeurs de conductivité standard et calibrées. Le but de l'étude est de comparer les résultats de localisation avec et sans calibration des conductivités, et aussi plus tard avec les localisations fines obtenues par SEEG. Cette étude est particulièrement intéressante puisque les sujets seront principalement des enfants et des adolescents pour lesquels l'os du crâne n'est pas encore arrivé à maturité, et donc sa conductivité peut être très variable.

Appendix

APPENDIX **A**

THE FINITE ELEMENT METHOD (FEM)

The FEM [119] is a broadly used method to approximate the solution of Partial Differential Equations (PDEs) or integral equations over a finite domain. Its ability to handle complex geometries and boundaries with relative ease and with a sound mathematical basis has made it the method of choice for solving problems such as structural mechanics, electromagnetic propagation and in some cases fluid dynamics. At the heart of the method are three main ingredients:

- A variational formulation of the PDE, obtained by multiplying the PDE by a test function w and integrating the resulting equation by parts over the domain of interest Ω. This results in a global criterion over Ω that encompasses both the PDE and the boundary conditions that are required to select a particular solution. This variational formulation usually decreases the amount of regularity required for the solution and is sometimes called the weak formulation of the problem.
- The variational problem is then discretized. An approximation of the solution of the variational criterion is sought in a discrete space, in such a way that when the discretization step tends to zero, the approximation tends to the original continuous solution of the variational problem. The discretization is usually defined by meshing the domain Ω and by approximating the original solution of the variational problem using interpolation over the mesh. Even though any type of mesh can be used for the domain, triangular or tetrahedral meshes are most often used because they are easier to adapt to the geometry of Ω. Quadrangular meshes are also often encountered.
- Once discretized the problem is solved as a linear matricial problem, with matrices that are guaranteed to be sparse.

In this appendix, we present in detail the Finite Element Method as applied to the electric potential PDE (3.7). It is meant as an introduction to chapter 4.

Contents

1 THE ELECTRIC POTENTIAL PDE

We recall the Poisson equation

$$\nabla \cdot (\sigma \nabla V) = f = \nabla \cdot \mathbf{J}^{\mathrm{p}} \ .$$

To obtain a unique solution, one needs to supplement this equation with a boundary condition. To do so, we hypothesize that no current flows outside of the head (which is mostly true except at the spinal column which is "far" from most EEG/MEG measurements). We thus have to solve the following problem:

$$\left\{ \begin{array}{rcll} \nabla \cdot (\sigma \nabla V) & = & \nabla \cdot \mathbf{J}^{\mathrm{p}} & \text{in} \quad \Omega \\ \\ \sigma \dfrac{\partial V}{\partial \mathbf{n}} = \sigma \nabla V \cdot \mathbf{n} & = & 0 & \text{on} \quad S = \partial\Omega. \end{array} \right. \tag{A.1}$$

This problem will be solved using a Finite Element Approach. We will first show that the PDE A.1 can be formulated as a variational problem (section 2), which is then discretized to obtain a linear system (section 3), and then solved (section 4).

2 A VARIATIONAL FORMULATION OF THE PDE

Let us first define some functional spaces that will be needed hereafter.

$$H^1(\Omega) = \left\{ w \in L^2(\Omega), \nabla w \in L^2(\Omega)^3 \right\} \ .$$

$$H^2(\Omega) = \left\{ w \in L^2(\Omega), \nabla w \in H^1(\Omega)^3 \right\} \ .$$

These spaces simply provide functions that can be plugged within the equations that will be used (with all integrals and differentiations well defined).

We first show that the following two problems are equivalent:

① $V \in H^2(\Omega)$ is solution of:

$$\left\{ \begin{array}{rcll} \nabla \cdot (\sigma \nabla V) & = & f & \text{in} \quad \Omega \\ \\ \sigma \dfrac{\partial V}{\partial \mathbf{n}} = \sigma \nabla V \cdot \mathbf{n} & = & g & \text{on} \quad S = \partial\Omega. \end{array} \right.$$

② $V \in H^1(\Omega)$ is such that

$$\forall w \in H^1(\Omega) \quad \int_\Omega \sigma(\mathbf{r}) \nabla V(\mathbf{r}) \cdot \nabla w(\mathbf{r}) \, d\mathbf{r} + \int_\Omega f(\mathbf{r}) w(\mathbf{r}) \, d\mathbf{r} - \int_S g(\mathbf{r}) w(\mathbf{r}) \, ds = 0 \ .$$

Notice that the PDE in ① is exactly the same as the one in A.1: we have just renamed $f = \nabla \cdot \mathbf{J}^{\mathrm{p}}$ and allowed for a more general Neumann boundary condition g. This makes the presentation slightly more general and shows that the basic method will remain the same even if there are currents injected on the boundary. The functions f and g are supposed to be square integrable, that is $f \in L^2(\Omega)$ and $g \in L^2(\partial\Omega)$.

Theorem A.1. *Problems ① and ② are equivalent.*

Proof.

① $\Longrightarrow$ ②
Using the formula: $\nabla \cdot (\sigma w \nabla V) = \sigma \nabla V \cdot \nabla w + w \nabla \cdot \sigma \nabla V$ and integrating it over the domain Ω, we have:

$$\int_\Omega w(\mathbf{r}) \nabla \cdot \sigma(\mathbf{r}) \nabla V(\mathbf{r})\, d\mathbf{r} = \int_\Omega \nabla \cdot (\sigma(\mathbf{r}) w(\mathbf{r}) \nabla V(\mathbf{r}))\, d\mathbf{r} - \int_\Omega \sigma(\mathbf{r}) \nabla V(\mathbf{r}) \cdot \nabla w(\mathbf{r})\, d\mathbf{r}$$

In the left hand side of this equation, $\nabla \cdot \sigma \nabla V$ can be replaced by f because of ①. The Green theorem can be used to transform the first term of the right hand side giving:

$$\int_\Omega \sigma(\mathbf{r}) \nabla V(\mathbf{r}) \cdot \nabla w(\mathbf{r})\, d\mathbf{r} + \int_\Omega f(\mathbf{r}) w(\mathbf{r})\, d\mathbf{r} - \int_S w(\mathbf{r}) \sigma(\mathbf{r}) \nabla V(\mathbf{r}) \cdot \mathbf{n}\, ds = 0\ .$$

Replacing $\sigma(\mathbf{r}) \nabla V(\mathbf{r}) \cdot \mathbf{n}$ by its value on S as given by the boundary condition of ① yields the result.

$$\int_\Omega \sigma(\mathbf{r}) \nabla V(\mathbf{r}) \cdot \nabla w(\mathbf{r})\, d\mathbf{r} + \int_\Omega f(\mathbf{r}) w(\mathbf{r})\, d\mathbf{r} - \int_S g(\mathbf{r}) w(\mathbf{r})\, ds = 0\ .$$

② $\Longrightarrow$ ①
If ② is true for any $w \in H^1(\Omega)$, it is also true for $w \in D(\Omega)$ the space of C^∞ functions with compact support in Ω. The dual of $D(\Omega)$ is the space of distributions over Ω, $D'(\Omega)$. If $\nabla \cdot (\sigma \nabla V) \in L^2(\Omega)$, then $\nabla \cdot (\sigma \nabla V) - f \in L^2(\Omega)$ since $f \in L^2(\Omega)$ by hypothesis. We denote by $< .,. >$ the duality bracket between the spaces $L^2(\Omega)$ and $D'(\Omega)$. Thus Eq. ② can be written as $< \nabla \cdot (\sigma \nabla V) - f, w >= 0$. From a standard result in functional analysis [Brezis 88], $\nabla \cdot (\sigma \nabla V) - f$ is zero almost everywhere.
□

3 DISCRETIZATION OF THE VARIATIONAL FORMULATION

3.1 General discrete framework

The 3D space Ω is tessellated with bounded cells (e.g. tetrahedra or hexahedra) (C_i), $i = 1 \ldots N_C$. This tessellation Ω_h also introduces a set of points $(\mathbf{P}_i)$, $i = 1 \ldots N_P$ (the vertices of the cells) and the space of the continuous functions over

Ω is approximated by a vector space using some basis functions (ϕ^i), $i = 1 \dots N_P$ defined at each vertex.

$$H_h^1(\Omega_h) = \left\{ w_h, \exists (w_1, \dots, w_{N_P}) \in \mathbb{R}^{N_P}, \quad w(\mathbf{r}) = \sum_{i=1}^{N_P} w_i \phi^i(\mathbf{r}) \right\} ,$$

The boundary of the tessellation S_h also defines a tessellation of S the boundary of Ω. Without loss of generality, we assume that the vertices of the tessellation that are on the boundary of the tessellation are $(\mathbf{P}_i)$, $i = 1 \dots N_S$ with $N_S < N_P$.

$$H_h^1(S_h) = \left\{ w_h, \exists (w_1, \dots, w_{N_S}) \in \mathbb{R}^{N_S}, \quad w_h(\mathbf{r}) = \sum_{i=1}^{N_S} w_i \phi_{S_h}^i(\mathbf{r}) \right\} ,$$

where $\phi_{S_h}^i$ is the restriction to S_h of the function ϕ^i.

The discretization of the variational formulation ② is obtained by using the discretized versions V_h, w_h, f_h and g_h of all the involved functions V, w, f and g :

$$\int_{\Omega_h} \sigma(\mathbf{r}) \nabla V_h(\mathbf{r}) \cdot \nabla w_h(\mathbf{r}) \, d\mathbf{r} + \int_{\Omega_h} f_h(\mathbf{r}) w_h(\mathbf{r}) \, d\mathbf{r} - \int_{S_h} g_h(\mathbf{r}) w_h(\mathbf{r}) \, ds = 0 . \qquad \text{(A.2)}$$

Furthermore, $H_h^1(\Omega_h)$ is a vector space of finite dimension equipped with the basis (ϕ^i), $i = 1 \dots N_P$. So if (A.2) is true for any $w_h \in H_h^1(\Omega_h)$, it is true for any ϕ^i, and reciprocally. So finally, the discretized version of the variational formulation ② is :

$V_h \in H_h^1(\Omega_h)$ is such that

$\forall \phi^i$, $i = 1 \dots N_P$
$\int_{\Omega_h} \sigma(\mathbf{r}) \nabla \left(\sum_{j=1}^{N_P} V_j \phi^j(\mathbf{r}) \right) \cdot \nabla \phi^i(\mathbf{r}) \, d\mathbf{r} + \int_{\Omega_h} f_h(\mathbf{r}) \phi^i(\mathbf{r}) \, d\mathbf{r} - \int_{S_h} g_h(\mathbf{r}) \phi_{S_h}^i(\mathbf{r}) \, ds = 0$

$\forall \phi^i$, $i = 1 \dots N_P$
$\sum_{j=1}^{N_P} V_j \int_{\Omega_h} \sigma(\mathbf{r}) \nabla \phi^j(\mathbf{r}) \cdot \nabla \phi^i(\mathbf{r}) \, d\mathbf{r} + \int_{\Omega_h} f_h(\mathbf{r}) \phi^i(\mathbf{r}) \, d\mathbf{r} - \int_{S_h} g_h(\mathbf{r}) \phi_{S_h}^i(\mathbf{r}) \, ds = 0 .$ (A.3)

We now introduce the matrix $\mathbf{A}$ of size $N_P \times N_P$ with the coefficients :

$$A_{ij} = \int_{\Omega_h} \sigma(\mathbf{r}) \nabla \phi^i(\mathbf{r}) \cdot \nabla \phi^j(\mathbf{r}) \, d\mathbf{r} .$$

Note that $\mathbf{A}$ is naturally symmetric. We also introduce the column vector $\mathbf{B}$ of size N_P :

$$B_i = \begin{cases} \int_{\Omega_h} f_h(\mathbf{r}) \phi^i(\mathbf{r}) \, d\mathbf{r} - \int_{S_h} g_h(\mathbf{r}) \phi_{S_h}^i(\mathbf{r}) \, ds & \text{for } i \leq N_S \\ \int_{\Omega_h} f_h(\mathbf{r}) \phi^i(\mathbf{r}) \, d\mathbf{r} & \text{otherwise .} \end{cases}$$

So by denoting $\mathbf{V} = [V_i]$ the column vector containing the coefficients of V_h in the basis (ϕ^i), (A.3) can be written as

$$\mathbf{AV} + \mathbf{B} = 0 .$$

$$\mathbf{V}^T\mathbf{A}\mathbf{V} = \sum_{i,j=1}^{N_P} V_i V_j A_{ij} = \sum_{i,j=1}^{N_P} \int_{\Omega_h} V_i V_j \sigma(\mathbf{r}) \nabla\phi^i(\mathbf{r}) \cdot \nabla\phi^j(\mathbf{r})\, d\mathbf{r} = \int_{\Omega_h} \sigma(\mathbf{r}) \left\|\nabla V_h(\mathbf{r})\right\|^2 d\mathbf{r} \tag{A.4}$$

This proves that the matrix $\mathbf{A}$ is positive because $\sigma > 0$ over Ω. Note, however that the matrix is not definite. Indeed, $\mathbf{V}^T\mathbf{A}\mathbf{V}$ is zero if $\nabla V_h(\mathbf{r}) = 0$ in Ω almost everywhere. This is natural as the original equation is insensitive to the addition to V of a constant function over Ω. On our discretized spaces, this happens for $V_h = Cst\mathbf{1}$ (this is the case whenever the constant function over Ω_h belongs to the space $H_h^1(\Omega_h)$ which is the case for the standard basis functions P1 or Q1 used for tetrahedric or hexahedric cells respectively). Similarly to Eq. A.4, we can prove that $\mathbf{V}_1^T\mathbf{A}\mathbf{V}_2 = \int_\Omega \sigma(\mathbf{r})\nabla V_{h1}(\mathbf{r}) \cdot \nabla V_{h2}(\mathbf{r})\, d\mathbf{r}$. Applying this result to $\mathbf{V}_2 = \mathbf{1}$, proves that the kernel of the matrix $\mathbf{A}$ is the constant vector $\mathbf{1}$. Rewriting this result for each line of the matrix gives:

$$\forall i = 1 \dots N_P \quad \sum_{j=1}^{N_P} A_{ij} = 0\ . \tag{A.5}$$

This result can be used to reduce the amount of memory used to store the matrix $\mathbf{A}$.

3.2 An implementation with P1 elements

In practice, the most common approach is to use P1 basis functions over a tetrahedral mesh. In dimension d, a tetrahedron T_j is defined by $d+1$ vertices $\mathbf{P}_{i_k}, k = 1 \dots d+1$. The restriction ϕ_j^i of ϕ^i to T_j is defined by (for notational simplicity, we assume without loss of generality that $\mathbf{P}_{i_1} = \mathbf{P}_1$):

$$\phi_j^i(\mathbf{r}) = \begin{cases} 0 & \text{if the vertex } \mathbf{P}_i \text{ does not belong to } T_j \\ \frac{|\mathbf{r}\ \mathbf{P}_2 \dots \mathbf{P}_{d+1}|}{|\mathbf{P}_1 \dots \mathbf{P}_{d+1}|} & \text{otherwise}\ , \end{cases}$$

where the vectors in the determinants are written with $d+1$ coordinates: the usual d coordinates are augmented with a final 1 (this is called projective or homogeneous coordinates). Because ϕ_j^i is a linear function of $\mathbf{r}$, its gradient is a constant vector. Given this value of the gradient $\nabla\phi_j^i$, the matrix $\mathbf{A}$ is computed as:

$$A_{ij} = \sum_{k:\mathbf{P}_i \in T_k, \mathbf{P}_j \in T_k} \int_{T_k} \sigma_k \nabla\phi_k^i(\mathbf{r}) \cdot \nabla\phi_k^j(\mathbf{r})\, d\mathbf{r}\ ,$$

Here, σ was discretized such that it has a constant value σ_k over the tetrahedron T_k, so all the terms in the integral are of the same order. It implies that the tetrahedral mesh must match with the subdomains where σ is constant. The formula for A_{ij} shows that the only non-diagonal non-zero coefficients of the matrix $\mathbf{A}$ correspond to the edges of the mesh. Consequently, the matrix $\mathbf{A}$ is very sparse.

Since we usually assume that $g = 0$ for the forward EEG problem, the computation of $\mathbf{B}$ includes only the term containing $f = \nabla \cdot \mathbf{J}^{\mathrm{p}}$.

$B_i = \int_{\Omega_h} \nabla \cdot \mathbf{J}^{\mathrm{p}}(\mathbf{r})\phi^i(\mathbf{r}) d\mathbf{r}$ becomes:

$$\begin{aligned} B_i &= \int_{\Omega_h} \nabla \cdot \left(\phi^i(\mathbf{r})\mathbf{J}^{\mathrm{p}}(\mathbf{r})\right)\, d\mathbf{r} - \int_{\Omega_h} \nabla\phi^i(\mathbf{r}) \cdot \mathbf{J}^{\mathrm{p}}(\mathbf{r})\, d\mathbf{r} \\ &= \int_{S_h} \phi^i(\mathbf{r})\mathbf{J}^{\mathrm{p}}(\mathbf{r}) \cdot \mathbf{n}(\mathbf{r})\, ds(\mathbf{r}) - \int_{\Omega_h} \nabla\phi^i(\mathbf{r}) \cdot \mathbf{J}^{\mathrm{p}}(\mathbf{r})\, d\mathbf{r} \end{aligned}$$

To go further, one needs to choose a specific model for $\mathbf{J}^{\mathrm{p}}$.

The continuous case In this first case, $\mathbf{J}^{\mathrm{p}}$ is represented as $\mathbf{J}^{\mathrm{p}}(\mathbf{r}) = \sum_{j=1}^{N_P} \phi^j(\mathbf{r})\mathbf{J}^{\mathrm{p}}_j$. Consequently:

$$B_i = \sum_{j=1}^{N_S} \mathbf{J}^{\mathrm{p}}_j \cdot \int_{S_h} \phi^i(\mathbf{r})\phi^j(\mathbf{r})\mathbf{n}(\mathbf{r})\, ds(\mathbf{r}) - \sum_{j=1}^{N_P} \mathbf{J}^{\mathrm{p}}_j \int_{\Omega_h} \nabla\phi^i(\mathbf{r}) \cdot \phi^j(\mathbf{r}) d\mathbf{r}$$

We can assume that there are no sources on S_h if we only consider sources in the brain, hence :

$$B_i = \sum_{j=1}^{N_P} \mathbf{J}^{\mathrm{p}}_j \int_{\Omega_h} \nabla\phi^i(\mathbf{r}) \cdot \phi^j(\mathbf{r}) d\mathbf{r} \ .$$

The Dirac case In this case, the current distribution is represented by one or several dipoles each localized at a single point in space. At one dipole position $\mathbf{r}_0$, the current orientation and strength are described by a vector $\mathbf{q}$. Thus, $\mathbf{J}^{\mathrm{p}}(\mathbf{r})$ can be written as: $\mathbf{J}^{\mathrm{p}}(\mathbf{r}) = \mathbf{q}\delta(\mathbf{r} - \mathbf{r}_0)$. Consequently,

$$B_i = \mathbf{q} \cdot \int_{S_h} \phi^i(\mathbf{r})\delta(\mathbf{r} - \mathbf{r}_0)\mathbf{n}(\mathbf{r})\, ds(\mathbf{r}) - \mathbf{q} \cdot \nabla\phi^i(\mathbf{r}_0)$$

Assuming again that the dipole is not on S_h gives:

$$B_i = -\mathbf{q} \cdot \nabla\phi^i(\mathbf{r}_0) \ . \tag{A.6}$$

4 SOLVING THE LINEAR SYSTEM

The solution of the discretized problem can be found by solving $\mathbf{AV} + \mathbf{B} = \mathbf{0}$. This is a fairly simple linear system, which could in theory be solved using a pseudo-inverse (the inverse of $\mathbf{A}$ does not exist since it is not definite). However, $\mathbf{A}$ is a very big matrix which can be stored only because it is sparse. Since the pseudo-inverse (or the inverse) of a sparse matrix is usually not a sparse matrix, it is unwise to try to compute it, as the amount of memory needed to store it will be huge. It is thus a much better idea to solve $\mathbf{AV} + \mathbf{B} = \mathbf{0}$ using an iterative method for each $\mathbf{B}$. Since the matrix $\mathbf{A}$ is symmetric and positive, the conjugate gradient method can be used. Strictly speaking, this method can only be used with definite matrices, but it actually works in this case provided that $\mathbf{B}$ is in the range of matrix $\mathbf{A}$. Because $\mathbf{A}$ is symmetric, the property (A.5) also holds for column vectors of $\mathbf{A}$, which means that these columns are all orthogonal to the constant vector $\mathbf{1}$. These vectors thus all have the property that their mean value is zero. It can be verified that this property is true for the various versions of $\mathbf{B}$ detailed above.

The conjugate gradient method only needs to evaluate the quantity $\mathbf{g} = \mathbf{AV} + \mathbf{B}$ for any given parameter vector $\mathbf{V}$ and the quantity $\mathbf{g}^T\mathbf{Ag}$ to compute the optimal step at each iteration. These two quantities can be easily evaluated using simple traversal of all the edges of the mesh.

In general, the conjugate gradient method only requires a few steps to converge (typically one or two magnitude order less iterations than N_P the size of the matrix). However, due to the very different values of the conductivities for the various parts of the head, this leads to badly conditioned matrices $\mathbf{A}$. To improve the speed of convergence, it is thus preferable to use a preconditioned conjugate gradient method. A simple Jacobi preconditioner is already very effective. Such a preconditioner is obtained by inverting a diagonal matrix whose entries are the diagonal elements of the matrix $\mathbf{A}$.

APPENDIX **B**

VARIANCE-BASED METHODS FOR GLOBAL SENSITIVITY ANALYSIS

This chapter is meant to introduce the global sensitivity analysis, and in particular the variance-based methods. We present the different sensitivity indices as well as the corresponding methods for their estimation.

Contents

1 GLOBAL SENSITIVITY ANALYSIS

We consider a mathematical model, made of a set of stochastic input variables, a deterministic function, and a set of stochastic output variables. We can write this model as :

$$\begin{array}{rcccl} f & : & \mathbb{R}^p & \rightarrow & \mathbb{R} \\ & & \mathbf{X} & \rightarrow & Y = f(\mathbf{X}) \end{array}$$

The function f can be very complex (a PDE system), and is usually evaluated with a computer code, more or less expensive. The set of input variables $\mathbf{X} = (X_1, \ldots, X_p)$ is made of all the model parameters which are considered as stochastic or uncertain. For the sake of simplicity, we will suppose here that the input variables are independent, and that the set of output variables is reduced to a single variable Y. The sensitivity analysis studies how perturbations on the input variables lead to perturbations on the output. The sensitivity analysis methods are usually clustered in three groups : *screening* methods, local sensitivity analyses and global sensitivity analyses. *Screening* methods give a qualitative analysis of the importance of the input variables with respect to the output variability. They allow to determine a hierarchy among the input variables, about how the inputs act upon the output variability. Local and global sensitivity analyses are quantitative methods : they give a hierachy of the inputs, and moreover they give an estimation of the intervals inside this hierarchy. Local sensitivity analyses study how small perturbations around a value $\mathbf{x}_0 = (x_1^0, \ldots, x_p^0)$ of the inputs affect the output value. The most common approach is to compute the sensitivity indices corresponding to the derivatives

$$S_i = \frac{\partial y}{\partial x_i}(x_1^0, \ldots, x_p^0) \ ,$$

which express the effect on the value of Y of perturbing the values of the variables X_i around a nominal value x_i^0. Global sensitivity analyses consider the variability of the output with respect to the input domain. It studies how the variability on the inputs projects on the output, by estimating how the output variability can be apportioned to certain inputs or set of inputs. The difference between local and global analyses can be sketched by saying that local analysis is interested in the output value whereas global analysis is interested in the output variability.

1.1 Goals of sensitivity analysis

When building or using a mathematical model, sensitivity analysis is a powerful tool. By studying how the model output reacts to the input variations, one can determine :

- If the model is correct. If the analysis reveals that an input is important whereas in reality it is known as non-influent, the model should be modified.
- Which inputs contribute most to the output variability. If the most important inputs are identified, the errors on the model output can be greatly reduced by focusing on reducing the error on these inputs.
- Which inputs have the least effect. They can be considered as deterministic, and fixed to an average value. The resulting model is simpler and has less

inputs.

- Which input variables interact with which others. The analysis can help to better understand the model, and how the inputs relate to each other.

1.2 Methods for global sensitivity analysis

The goal of the global sensitivity analysis is to apportion the uncertainty on the output to the different inputs, ie determine to what extent the uncertainty of each input variable contributes to the output uncertainty. A review of all existing methods is presented in [86]. In this chapter, we present only one method, based on the variance decomposition of the model, because it is the one we use in chapter 6. The idea of the method is to determine which part of the output variance is due to the variance of each input, by decomposing the total variance of the output in conditional variances with respect to the different inputs. It leads to the definition of sensitivity indices, which reflect the model sensitivity to each input variable. We then present how to estimate these indices.

2 VARIANCE-BASED METHOD

We consider the model

$$Y = f(X_1, \ldots, X_p) \tag{B.1}$$

where the input variables are independent. To quantify the importance of an input X_i on the variance of the output Y, we can look at how much the variance of Y decreases if we fix X_i to a value x_i^* :

$$V(Y|X_i = x_i^*) \ .$$

This quantity is the conditional variance of Y given the value $X_i = x_i^*$. The problem of this index is the choice of the value x_i^* of X_i, which can be solved by considering the expectation of this quantity for all possible values x_i^* :

$$E\left[V(Y|X_i)\right] \ .$$

The more important X_i with respect to the variance of Y, the smaller this quantity.

Theorem 1. *Total variance theorem*
Let X_i and Y be stochastic variables, where the values of Y are in $\mathbb{R}$ and the values of X_i are in a finite or enumerable set, or in $\mathbb{R}$ or $\mathbb{R}^p$. If the variance of Y is finite, then :

$$V(Y) = V(E\left[Y|X_i\right]) + E\left[V(Y|X_i)\right] \ .$$

From theorem 1, an index of the sensitivity of Y to X_i is the variance of the expectation of Y given X_i :

$$V(E\left[Y|X_i\right]) \ .$$

The more important X_i, the bigger this quantity. For normalization, we define the following sensitivity index.

Definition 1. *The sensitivity index quantifying the sensitivity of Y to X_i is defined as :*

$$S_i = \frac{V(E[Y|X_i])}{V(Y)} \tag{B.2}$$

This index is called first order sensitivity index by Sobol [96], and is sometimes called *importance measure*. It quantifies the part of variance of Y due to the input variable X_i.

Theorem 2. *Sobol decomposition of the variance*
The variance of the model (B.1) *with independent inputs can be decomposed as :*

$$V = \sum_{i=1}^{p} V_i + \sum_{1 \le i < j \le p} V_{ij} + \cdots + V_{1\ldots p} \ , \tag{B.3}$$

where

$$\begin{array}{lcl} V & = & V(Y), \\ V_i & = & V(E[Y|X_i]), \\ V_{ij} & = & V(E[Y|X_i, X_j]) - V_i - V_j, \\ V_{ijk} & = & V(E[Y|X_i, X_j, X_k]) - V_i - V_j - V_k - V_{ij} - V_{ik} - V_{jk}, \\ & \cdots & \\ V_{1\ldots p} & = & V - \sum_{i=1}^{p} V_i - \sum_{1 \le i < j \le p} V_{ij} - \cdots - \sum_{1 \le i_1 < \cdots < i_{p-1} \le p} V_{i_1 \ldots i_{p-1}} \end{array}$$

The proof can be found in [96].

Definition 2. *We can then define the first order sensitivity indices :*

$$S_i = \frac{V_i}{V}, \tag{B.4}$$

the second order sensitivity indices :

$$S_{ij} = \frac{V_{ij}}{V},$$

which quantify the sensitivity of Y to the interaction between X_i and X_j, ie the sensitivity of Y to X_i and X_j which is not taken into account in the effect of the variables alone. We can also define the third order sensitivity indices :

$$S_{ijk} = \frac{V_{ijk}}{V},$$

which quantify the sensitivity of Y to the variables X_i, X_j, X_k which is not taken into account in the effect of the variables alone and in the two-by-two interactions. One can thus pursue up to the order p.

Remark. *The definition of the first order sensitivity index given by Sobol decomposition* (B.4) *is the same as the previous one* (B.2)*.*

The interpretation of these indices is easy : thanks to (B.3), their sum is equal to 1, and they are all positive. As a consequence, the bigger (close to 1) the sensitivity index, the more important the variable.

The number of sensitivity indices, from order 1 to order p, is equal to $2^p - 1$. When the number p of input variables increases, the number of sensitivity indices becomes

too big, and the estimation and interpretation of all the indices is impossible. We can then consider the total sensitivity indices, which quantify the total sensitivity of Y to one variable, ie the sensitivity to this variable alone plus the sensitivity to the interactions of this variable with others.

Definition 3. *The total sensitivity index S_{T_i} of the variable X_i is defined as the sum of all the sensitivity indices relative to X_i :*

$$S_{T_i} = \sum_{k \# i} S_k \ , \tag{B.5}$$

where $\#i$ is meant to represent all the set of indices which contain the index i.

For instance, for a model with three input parameters :

$$S_{T_1} = S_1 + S_{12} + S_{13} + S_{123} \ .$$

Remark. *From theorem 1, we have :*

$$1 = \underbrace{\frac{V(E[Y|X_i])}{V(Y)}}_{S_i} + \frac{E[V(Y|X_i)]}{V(Y)},$$

so if we now consider all the parameters but X_i, denoted $X_{\sim i}$, we have :

$$1 = \frac{V(E[Y|X_{\sim i}])}{V(Y)} + \underbrace{\frac{E[V(Y|X_{\sim i})]}{V(Y)}}_{S_{T_i}} \ . \tag{B.6}$$

All the sensitivity indices that we presented do not require any hypothesis on the model itself (eg linear, non-linear), but it is necessary that the input parameters are independent. All these sensitivity indices, especially the first order and total indices, are used in chapter 6.

3 ESTIMATION OF THE SENSITIVITY INDICES

The sensitivity indices can sometimes be computed analytically when the function f of the model is known and simple. But when f is complex, without an analytical form (the result of a computer code for instance), the sensitivity indices can not be computed directly and it is necessary to estimate them.

3.1 Monte Carlo methods

We consider the following integral :

$$I = \int_D f(\mathbf{x}) d\mathbf{x} \ ,$$

where D can be a space of high dimension, and f is an integrable function. Let $\mathbf{x}_1, \ldots, \mathbf{x}_N$ be a random sampling of a uniformly random variable on D. In the Monte

Carlo method, I is approximated by

$$\hat{I}_N = \frac{1}{N} \sum_{i=1}^{N} f(\mathbf{x}_i) \ .$$

The law of large numbers states that the mean of a series of independent random variables with the same expectation and finite variance converges almost surely to the expectation. As a consequence :

$$\lim_{N \to +\infty} \hat{I}_N = I \ , \quad \text{with a probability equal to 1} \ .$$

More generally, for a random variable X with a probability density function μ, the expectation of $f(X)$

$$E\left[f(X)\right] = \int f(x)\mu(x)dx \ ,$$

can be estimated by

$$\hat{E}\left[f(X)\right] = \frac{1}{N} \sum_{i=1}^{N} f(\mathbf{x}_i) \ ,$$

where $(x_i)_{i=1..N}$ is a sampling of N realisations of the random variable X. If $f(X)$ has a finite variance σ^2, the convergence rate of a Monte Carlo method is given by the limit central theorem :

$$\frac{\sqrt{N}}{\sigma}(\hat{I}_N - I) \xrightarrow{\mathcal{L}} \mathcal{N}(0,1) \ .$$

The convergence rate is then $\mathcal{O}(N^{-\frac{1}{2}})$.

3.2 Convergence

The random sampling is the basic approach when using a Monte Carlo method and has a convergence rate of $\mathcal{O}(N^{-\frac{1}{2}})$. Many other approaches have been proposed to increase the convergance rate, in particular using pseudo-random sequences. For instance, the methods called Quasi-Monte Carlo [73] are deterministic versions of the Monte Carlo method : the series of samples is deterministic and has a better uniform distribution in the space of input variables. With this type of sampling, the convergence can be $\mathcal{O}(N^{-1}(logN)^{p-1})$ with weak regularity assumptions on f. These methods can be extended by randomizing the deterministic sequences, and the convergence rate can be increased to $\mathcal{O}(N^{-\frac{3}{2}}(logN)^{\frac{p-1}{2}})$.

3.3 Estimation of the sensitivity indices with Monte Carlo

We consider N realisations of the input variables $(X_1, \ldots, X_p)$:

$$\tilde{X}_N = (x_{k1}, \ldots, x_{kp})_{k=1..N} \ .$$

The expectation of Y, $E[Y] = f_0$, and its variance, $V(Y) = V$, are estimated by :

$$\hat{f}_0 = \frac{1}{N}\sum_{k=1}^{N} f(x_{k1}, \ldots, x_{kp}) \ , \tag{B.7}$$

$$\hat{V} = \frac{1}{N}\sum_{k=1}^{N} f^2(x_{k1}, \ldots, x_{kp}) - \hat{f}_0^2 \ . \tag{B.8}$$

To estimate the sensitivity indices, we need to estimate conditional variances. We present the approach due to Sobol [96]. For the first order sensitivity indices (B.4), we need to estimate the quantity :

$$V_i = V(E[Y|X_i]) = E\left[E[Y|X_i]^2\right] - E[E[Y|X_i]]^2 = U_i - E[Y]^2 \ ,$$

while the variance of Y is estimated with (B.8).

At first sight, it might seem that the computational strategy for the estimation of $U_i = E\left[E[Y|X_i]^2\right]$ would be to first use a set of Monte Carlo points to estimate the inner expectation for a fixed value of X_i, and then repeat the procedure many times for different X_i values to estimate the outer expectation. To give an indication, if 1000 points were used to get a good estimate of the conditional expectation $E[Y|X_i]$, and the procedure were repeated 1000 times to estimate the outer expectation, then we would need 10^6 points just for one sensitivity index. This in fact not necessary, as the computation can be accelerated via a shortcut. We denote $\mathbf{x} = (x_i, \mathbf{z})$ some realizations of the input variables, distinguishing between x_i and the other variables denoted by $\mathbf{z}$. We can then rewrite U_i :

$$\begin{aligned} E\left[E[Y|X_i]^2\right] &= \int \left[\int f(\mathbf{x})d\mathbf{z}\right]^2 dx_i \\ &= \int \left[\int f(x_i, \mathbf{z})d\mathbf{z}\right]\left[\int f(x_i, \mathbf{z}')d\mathbf{z}'\right] dx_i \\ &= \int f(x_i, \mathbf{z})f(x_i, \mathbf{z}')d\mathbf{z}d\mathbf{z}'dx_i \end{aligned} \tag{B.9}$$

The idea is to estimate U_i like a normal expectation (B.7) using the formulation (B.9). We hence need two sets of realisations, denoted $\tilde{X}_N^1$ and $\tilde{X}_N^2$. Then an estimator of U_i is :

$$\hat{U}_i = \frac{1}{N}\sum_{k=1}^{N} f\left(x_{k1}^1, .., x_{k(i-1)}^1, x_{ki}^1, x_{k(i+1)}^1, .., x_{kp}^1\right) \times f\left(x_{k1}^2, .., x_{k(i-1)}^2, x_{ki}^1, x_{k(i+1)}^2, .., x_{kp}^2\right) \ .$$

At each sample set k, all variables are sampled twice except X_i. The first order sensitivity indices are estimated by :

$$\hat{S}_i = \frac{\hat{V}_i}{\hat{V}} = \frac{\hat{U}_i - \hat{f}_0^2}{\hat{V}} \ .$$

For the second order sensitivity index $S_{ij} = \frac{V_{ij}}{V}$, where :

$$V_{ij} = V(E[Y|X_i, X_j]) - V_i - V_j = U_{ij} - E[Y]^2 - V_i - V_j \ ,$$

the quantity U_{ij} is estimated in the same way, by sampling all variables twice except X_i and X_j for a sample set k. The index S_{ij} is then estimated by :

$$\hat{S}_{ij} = \frac{\hat{U}_{ij} - \hat{f}_0^2 - \hat{V}_i - \hat{V}_j}{\hat{V}} \quad .$$

And it is the same for indices of greater orders.

Remark. *The estimation of sensitivity indices of order i requires the estimation of indices of order 1 to $i-1$.*

On the contrary, the total sensitivity indices can be estimated directly. From (B.6), we can write :

$$S_{T_i} = 1 - \frac{V\left(E\left[Y|X_{\sim i}\right]\right)}{V(Y)} = 1 - \frac{V_{\sim i}}{V} \quad ,$$

where $V_{\sim i}$ is the variance of the expectation of Y given all variables but X_i :

$$V_{\sim i} = E\left[E\left[Y|X_{\sim i}\right]^2\right] - E\left[E\left[Y|X_{\sim i}\right]\right]^2 = U_{\sim i} - E\left[Y\right]^2 \quad .$$

$U_{\sim i}$ is estimated like U_i, but instead of varying all variables but X_i, we vary only X_i :

$$\hat{U}_{\sim i} = \frac{1}{N}\sum_{k=1}^{N} f\left(x_{k1}^1, .., x_{k(i-1)}^1, x_{ki}^1, x_{k(i+1)}^1, .., x_{kp}^1\right) \times f\left(x_{k1}^1, .., x_{k(i-1)}^1, x_{ki}^2, x_{k(i+1)}^1, .., x_{kp}^1\right) \quad ,$$

and so

$$\hat{S}_{T_i} = 1 - \frac{\hat{U}_{\sim i} - \hat{f}_0^2}{\hat{V}} \quad .$$

Remark. *If the size of the Monte Carlo sampling is N, then the estimation of the sensitivity indices requires $2N$ realisations of the input parameters, because we need two sets of simulations. The number of calls to the model function f is then $N \times (k+1)$, where k is the number of indices to be estimated. For a model with p input parameters, $N \times 2^p$ function calls are necessary to estimate all the indices. On the contrary, if only the first order and total indices are estimated, $N \times (2p+1)$ calls are needed.*

3.4 The FAST method

The FAST method (Fourier Amplitude Sensitivity Test) was first developped in [18]. Its purpose is to estimate the first order sensitivity indices. We consider a function

$$f(\mathbf{x}) = f(x_1, \ldots, x_p) \quad ,$$

where $\mathbf{x} \in [0,1]^p$, and the corresponding stochastic model $Y = f(X_1, \ldots, X_p)$. It is possible to get a decomposition of the variance of Y, like with Sobol's method, by using the multidimensional Fourier transform of f. But the computational cost of such a multidimensional decomposition is too big in practical situations, so the idea of the FAST method is to use a unidimensional decomposition along a curve covering

the space $[0,1]^p$. This curve is defined by a set of parametric equations :

$$x_i(s) = g_i(\sin(w_i s)) \quad \text{for} \quad i = 1, \ldots, p \ ,$$

where g_i are functions which give a uniform covering of $[0,1]^p$, and $(w_1, \ldots, w_p) \in \mathbb{N}^p$ is a set of incommensurate integer frequencies (linearly independent with integer coefficients). When s varies in $\mathbb{R}$, the vector $(x_1(s), \ldots, x_p(s))$ describes a curve covering $[0,1]^p$. It can be shown that :

$$f_0 = \int_{[0,1]^p} f(\mathbf{x}) dx = \lim_{T \to \infty} \frac{1}{2\pi} \int_{-T}^{T} f(\mathbf{x}(s)) ds \ .$$

Because the frequencies $(w_1, \ldots, w_p)$ are integers, the curve does not fill the space $[0,1]^p$ but is 2π-periodic, so :

$$f_0 = \frac{1}{2\pi} \int_{-\pi}^{\pi} f(\mathbf{x}(s)) ds \ .$$

This idea can be used to compute the variance V of a model $Y = f(X_1, \ldots, X_p)$. Denoting $f_0 = E[Y]$, we get :

$$\begin{aligned} V &= \frac{1}{2\pi} \int_{-\pi}^{\pi} f^2(\mathbf{x}(s)) ds - f_0^2 \\ &= \sum_{j=-\infty}^{\infty} (A_j^2 + B_j^2) - A_0^2 \\ &= 2 \sum_{j=1}^{\infty} (A_j^2 + B_j^2) \ , \end{aligned} \tag{B.10}$$

where A_j and B_j are the Fourier coefficients defined as :

$$\begin{aligned} A_j &= \frac{1}{2\pi} \int_{-\pi}^{\pi} f(\mathbf{x}(s)) \cos(js) ds \ , \\ B_j &= \frac{1}{2\pi} \int_{-\pi}^{\pi} f(\mathbf{x}(s)) \sin(js) ds \ . \end{aligned}$$

In the theory of the FAST method, it is explained that the part of the variance (B.10) due to the input variable X_i is the sum of squares of the Fourier coefficients A_j and B_j corresponding to the frequency w_i and its harmonics :

$$V_i = 2 \sum_{k=1}^{\infty} (A_{kw_i}^2 + B_{kw_i}^2) \ .$$

The sensitivity index S_i is then defined by :

$$S_i = \frac{\sum_{k=1}^{\infty} (A_{kw_i}^2 + B_{kw_i}^2)}{\sum_{j=1}^{\infty} (A_j^2 + B_j^2)} \ .$$

The FAST method was extended in [87] for the total sensitivity indices. The part of the variance due to all variables but X_i is evaluated as the sum of squares of the Fourier coefficients corresponding to the frequencies $w_{\sim i}$ different from w_i and its

harmonics :

$$V_{\sim i} = 2\sum_{k=1}^{\infty}(A^2_{kw_{\sim i}} + B^2_{kw_{\sim i}}) \ .$$

Then the total sensitivity index S_{T_i} is given, as with Sobol's method, by :

$$S_{T_i} = 1 - \frac{\sum_{k=1}^{\infty}(A^2_{kw_{\sim i}} + B^2_{kw_{\sim i}})}{\sum_{j=1}^{\infty}(A^2_j + B^2_j)} \ .$$

3.5 Estimation of the FAST sensitivity indices

When estimating the indices defined by the FAST method, it is necessary to define the functions g_i and the frequencies w_i that are used. A boundary M on the number of harmonics considered must also be fixed, in order to compute a finite number of Fourier coefficients. The choice of M is a trade-off between accuracy and computational complexity :

- the greater M, the better the sensitivity indices reflect the effects of the input parameters,
- the greater M, the bigger the sampling size of the input parameters (due to Nyquist-Shannon sampling theorem).

In general, a choice of $M = 4$ or $M = 6$ is sufficient, independently of the dimension of the model. For the choice of the functions g_i, many options are possible, knowing that they must cover as well as possible the space $[0, 1]^p$. As shown in [87], a good choice is :

$$x_i(s) = g_i(\sin(w_i s)) = \frac{1}{2} + \frac{1}{\pi}\arcsin(\sin(w_i s)), \quad s \in [-\pi, \pi] \ .$$

There are also many possibilities for the choice of the frequencies. The theory of the FAST method states that the frequencies must be incommensurate, which can be complicated and lead to the choice of high frequencies. Nevertheless, the fact that only a small number of harmonics are taken into account allow to use frequencies that are not necessarily incommensurate. An automatic approach for the choice of frequencies is described in [87]. The important point is that these frequencies determine the minimum size of sampling for the computation of the indices :

$$N = 2M\max_i(w_i) + 1 \ ,$$

where M is the highest harmonic considered. In general, for the same accuracy, the FAST method requires a smaller size of sampling than Sobol's method.

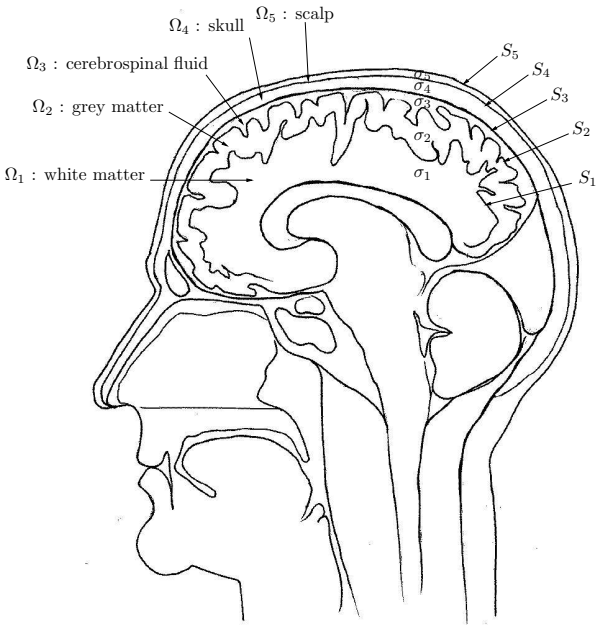

Figure C.1: An example of piecewise constant head model.

APPENDIX C

GESELOWITZ'S FORMULAS

We consider a geometry corresponding to the figure C.1. The head is described as a domain Ω composed of several subregions Ω_k separated by surfaces S_k, each with a constant conductivity σ_k, and with $\sigma = 0$ outside Ω.

1 ELECTRIC POTENTIAL

At the surfaces S_k where the conductivity is discontinuous, we have the following boundary conditions (continuity of potential and current density) :

$$\begin{cases} V_k(\mathbf{r}') = V_{k+1}(\mathbf{r}') \\ \sigma_k \nabla V_k(\mathbf{r}') \cdot \mathbf{n}_k(\mathbf{r}') = \sigma_{k+1} \nabla V_{k+1}(\mathbf{r}') \cdot \mathbf{n}_k(\mathbf{r}') \end{cases} \quad \forall \mathbf{r}' \in S_k \tag{C.1}$$

where $\mathbf{n}_k$ is the outward unit normal to the surface S_k, and V_k is the restriction

of the potential V to the subdomain Ω_k. We assume in the following that $\mathbf{r}$ does not belong to any S_k so that for any $\mathbf{r}' \in S_k$, $\frac{1}{R} = \frac{1}{\|\mathbf{r}-\mathbf{r}'\|}$ is well defined. As a consequence, using the divergence theorem and taking into account the discontinuities, we get :

$$\begin{array}{rcl} \int_\Omega \frac{1}{R}\Delta(\sigma(\mathbf{r}')V(\mathbf{r}'))dr' & = & \sum_k \int_{S_k} \frac{1}{R}(\sigma_k \nabla V_k(\mathbf{r}') \cdot \mathbf{n}_k(\mathbf{r}') - \sigma_{k+1}\nabla V_{k+1}(\mathbf{r}') \cdot \mathbf{n}_k(\mathbf{r}'))ds' \\ & & - \int_\Omega \nabla(\sigma(\mathbf{r}')V(\mathbf{r}')) \cdot \nabla\left(\frac{1}{R}\right) dr' \\ & = & - \int_\Omega \nabla(\sigma(\mathbf{r}')V(\mathbf{r}')) \cdot \nabla\left(\frac{1}{R}\right) dr' \ , \end{array} \tag{C.2}$$

and also

$$\begin{array}{rcl} \int_\Omega \sigma(\mathbf{r}')V(\mathbf{r}')\Delta\left(\frac{1}{R}\right) & = & \sum_k \int_{S_k} (\sigma_k - \sigma_{k+1})V(\mathbf{r}')\nabla\left(\frac{1}{R}\right) \cdot \mathbf{n}_k(\mathbf{r}')ds' - \int_\Omega \nabla(\sigma(\mathbf{r}')V(\mathbf{r}')) \cdot \nabla\left(\frac{1}{R}\right) dr' \\ & = & \sum_k \int_{S_k} (\sigma_k - \sigma_{k+1})V(\mathbf{r}')\nabla\left(\frac{1}{R}\right) \cdot \mathbf{n}_k(\mathbf{r}')ds' + \int_\Omega \frac{1}{R}\Delta(\sigma(\mathbf{r}')V(\mathbf{r}'))dr' \ . \end{array} \tag{C.3}$$

$-\frac{1}{4\pi R}$ is the Green function for the Laplacian operator, meaning that

$$\Delta\left(\frac{1}{R}\right) = -4\pi\delta(\mathbf{r}-\mathbf{r}') \ .$$

As a consequence, if σV is continuous at $\mathbf{r}$, i.e. $\mathbf{r}$ does not belong to any S_k, we have

$$\int_\Omega \sigma(\mathbf{r}')V(\mathbf{r}')\Delta\left(\frac{1}{R}\right) dr' = -4\pi\sigma(\mathbf{r})V(\mathbf{r}) \ .$$

Also, in each domain Ω_k, $\sigma = \sigma_k$ is constant so

$$\Delta(\sigma_k V) = \nabla \cdot (\sigma_k \nabla V) = \nabla \cdot \mathbf{J}^{\mathrm{p}} \ .$$

We hence have

$$\begin{array}{rcl} \int_\Omega \frac{1}{R}\Delta(\sigma(\mathbf{r}')V(\mathbf{r}'))dr' & = & \int_\Omega \frac{1}{R}\nabla \cdot \mathbf{J}^{\mathrm{p}}(\mathbf{r}')dr' \\ & = & -\int_\Omega \nabla\left(\frac{1}{R}\right) \cdot \mathbf{J}^{\mathrm{p}}(\mathbf{r}')dr' \end{array}$$

using the divergence theorem and the fact that $\mathbf{J}^{\mathrm{p}}$ is zero on the boundary of Ω (no brain activity at the surface of the head). So finally, (C.3) becomes :

$$-4\pi\sigma(\mathbf{r})V(\mathbf{r}) = \sum_k \int_{S_k} (\sigma_k - \sigma_{k+1})V(\mathbf{r}')\nabla\left(\frac{1}{R}\right) \cdot \mathbf{n}_k(\mathbf{r}')ds' - \int_\Omega \nabla\left(\frac{1}{R}\right) \cdot \mathbf{J}^{\mathrm{p}}(\mathbf{r}')dr'$$

which can be rewritten

$$\sigma(\mathbf{r})V(\mathbf{r}) = V_0(\mathbf{r}) - \frac{1}{4\pi}\sum_k (\sigma_k - \sigma_{k+1}) \int_{S_k} V(\mathbf{r}')\nabla\left(\frac{1}{R}\right) \cdot \mathbf{n}_k(\mathbf{r}')ds' \tag{C.4}$$

where V_0 is the potential generated by $\mathbf{J}^{\mathrm{p}}$ in an infinite homogeneous medium with unitary conductivity. Because of our assumptions, this formulation is valid only if $\mathbf{r}$ does not belong to any S_k. Let us note

$$I_k(\mathbf{r}) = \int_{S_k} V(\mathbf{r}')\nabla\left(\frac{1}{R}\right) \cdot \mathbf{n}_k(\mathbf{r}')ds' \ .$$

For a point $\mathbf{s} \in S_k$, it can be shown that

$$\lim_{\mathbf{r}\to\mathbf{s}} I_k(\mathbf{r}) = 2\pi V(\mathbf{s}) + I_k(\mathbf{s}) \ .$$

From this result, we can compute the limit of (C.4). For $\mathbf{r} \in S_k$, we get

$$\boxed{\frac{\sigma_k+\sigma_{k+1}}{2} V(\mathbf{r}) = V_0(\mathbf{r}) - \frac{1}{4\pi}\sum_l (\sigma_l - \sigma_{l+1}) \int_{S_l} V(\mathbf{r}')\nabla\left(\frac{1}{R}\right)\cdot \mathbf{n}_l(\mathbf{r}')ds'} \qquad \text{(C.5)}$$

This formula was established in 1967 by Geselowitz [32]. It is an integral equation which determines the value of V on the surfaces S_k. And once V is known on the S_k, we can compute its value in the whole head domain using (C.4). This is the advantage of the piecewise constant model : the potential is fully determined by its value at the surface of discontinuities, what transforms the general potential equation (3.7) into the simpler equation (C.5).

2 MAGNETIC FIELD

The equation of the magnetic field (3.8) can also be simplified in the case of a piecewise constant model. First, we can decompose the integrals on the different domains Ω_k :

$$\mathbf{B}(\mathbf{r}) = \mathbf{B}_0(\mathbf{r}) - \frac{\mu_0}{4\pi}\sum_k \sigma_k \int_{\Omega_k} \nabla V(\mathbf{r}') \times \frac{(\mathbf{r}-\mathbf{r}')}{\|\mathbf{r}-\mathbf{r}'\|^3} dr' \ .$$

Then, using the identity

$$\nabla V(\mathbf{r}') \times \frac{(\mathbf{r}-\mathbf{r}')}{\|\mathbf{r}-\mathbf{r}'\|^3} = \nabla \times \left(V(\mathbf{r}') \frac{(\mathbf{r}-\mathbf{r}')}{\|\mathbf{r}-\mathbf{r}'\|^3} \right)$$

and Stokes' theorem, each integral on a domain Ω_k can be transformed in a surface integral :

$$\int_{\Omega_k} \nabla V(\mathbf{r}') \times \frac{(\mathbf{r}-\mathbf{r}')}{\|\mathbf{r}-\mathbf{r}'\|^3} dr' = \int_{S_{k+1}} V(\mathbf{r}') \frac{(\mathbf{r}-\mathbf{r}')}{\|\mathbf{r}-\mathbf{r}'\|^3} \times \mathbf{n}_{k+1}(\mathbf{r}') - \int_{S_k} V(\mathbf{r}') \frac{(\mathbf{r}-\mathbf{r}')}{\|\mathbf{r}-\mathbf{r}'\|^3} \times \mathbf{n}_k(\mathbf{r}') ds'$$

By grouping pairs of surfaces, we obtain the final result :

$$\boxed{\mathbf{B}(\mathbf{r}) = \mathbf{B}_0(\mathbf{r}) - \frac{\mu_0}{4\pi}\sum_k (\sigma_k - \sigma_{k+1}) \int_{S_k} V(\mathbf{r}') \frac{(\mathbf{r}-\mathbf{r}')}{\|\mathbf{r}-\mathbf{r}'\|^3} \times \mathbf{n}_k(\mathbf{r}') ds' \ .} \qquad \text{(C.6)}$$

This formula for the magnetic field implies that the potential V is known on the surfaces S_k, which is possible due to (C.5). It is again due to Geselowitz [33].

Bibliography

[1] M. Akhtari, H.C. Bryant, A.N. Mamelak, E.R. Flynn, L. Heller, J.J. Shih, M. Mandelkern, A. Matlachov, D.M. Ranken, E.D. Best, M.A. DiMauro, R.R. Lee, and W.W. Sutherling. Conductivities of three-layer live human skull. *Brain Topography*, 14(3):151–167, 2002.

[2] A. El Badia and T. Ha-Duong. An inverse source problem in potential analysis. *Inverse Problems*, 16:651–663, 2000.

[3] Sylvain Baillet and Line Garnero. A bayesian approach to introducing anatomo-functional priors in the EEG/MEG inverse problem. *IEEE Transactions on Biomedical Engineering*, 44(5):374–385, May 1997.

[4] L. Baratchart, J. Leblond, F. Mandrea, and E.B. Saff. How can the meromorphic approximation help to solve some 2D inverse problems for the Laplacian? *Inverse Problems*, 15:79–90, 1999.

[5] L. Baratchart, J. Leblond, and J.-P. Marmorat. Inverse source problem in a 3D ball from best meromorphic approximation on 2D slices. *Electronic Transactions in Numerical Analysis*, 25:41–53, 2006.

[6] S.B. Baumann, D.R. Wozny, S.K. Kelly, and F.M. Meno. The electrical conductivity of human cerebrospinal fluid at body temperature. *IEEE Transactions on Biomedical Engineering*, 44(3):220–223, 1997.

[7] U. Baysal and J. Haueisen. Use of a priori information in estimating tissue resistivities - application to human data in vivo. *Physiol. Meas.*, 25:737–748, 2004.

[8] P. Berg and M. Scherg. A fast method for forward computation of multiple-shell spherical head models. *Electroencephalogr. Clin. Neurophysiol.*, 90(1):58–64, 1994.

[9] K. Brodmann. *Vergleichende Lokalisationslehre der Grobhirnrinde*. J.A.Barth, Leipzig, 1909.

[10] D.P. Buxhoeveden and M.F. Casanova. The minicolumn hypothesis in neuroscience. *Brain*, 125:935–951, 2002.

[11] M. Chafik, A. El Badia, and T. Ha-Duong. On some inverse EEG problems. In M. Tanaka and G. S. Dulikravich, editors, *Inverse Problem in Engineering Mechanics II*, pages 537–544. Elsevier Science Ltd, 2000.

[12] N. Chauveau, X. Franceries, B. Doyon, B. Rigaud, J.P. Morucci, and P. Celsis. Effects of skull thickness, anisotropy, and inhomogeneity on forward EEG/ERP computations using a spherical three-dimensional resistor mesh model. *Human Brain Mapping*, 21:86–97, 2004.

[13] K.S. Cheng, D. Isaacson, J.C. Newell, and D.G. Gisser. Electrode models for electric current computed tomography. *IEEE Transactions on Biomedical Engineering*, 36(9), sep 1989.

[14] E. Chernyaev. Marching cubes 33: Construction of topologically correct isosurfaces. Technical Report CN/95-17, CERN, August 1995.

[15] C.J.S. Clarke and B.S. Janday. The solution of the biomagnetic inverse problem by maximum statistical entropy. *Inverse Problems*, 5:483–500, 1989.

[16] Y. Cointepas, J.-F. Mangin, Line Garnero, J.-B. Poline, and H. Benali. BrainVISA: Software platform for visualization and analysis of multi-modality brain data. In *Proc. 7th HBM*, page S98, Brighton, United Kingdom, 2001.

[17] B.N. Cuffin. EEG localization accuracy improvements using realistically shaped head models. *IEEE Trans. on Biomed. Engin.*, 43(3), 1996.

[18] R.I. Cukier, C.M. Fortuin, K.E. Shuler, A.G. Petschek, and J.H. Schaibly. Study of the sensitivity of coupled reaction systems to uncertainties in rate coefficients - theory. *Journal Chemical Physics*, 59:3873–3878, 1973.

[19] A.M. Dale, B. Fischl, and M.I. Sereno. Cortical surface-based analysis I: Segmentation and surface reconstruction. *NeuroImage*, 9:179–194, 1999.

[20] A.M. Dale and M.I. Sereno. Improved localization of cortical activity by combining EEG and MEG with MRI cortical surface reconstruction: A linear approach. *Journal of Cognitive Neuroscience*, 5(2):162–176, 1993.

[21] G. Dassios and F. Kariotou. Magnetoencephalography in ellipsoidal geometry. *Journal of Mathematical Physics*, 44:220–241, 2003.

[22] J. C. De Munck. The potential distribution in a layered anisotropic spheroidal volume conductor. *J. Appl. Phys*, 64(2):464–470, jul 1988.

[23] J. C. de Munck. A linear discretization of the volume conductor boundary integral equation using analytically integrated elements. *IEEE Trans. Biomed. Eng.*, 39(9):986–990, September 1992.

[24] J.C. de Munck and M.J. Peters. A fast method to compute the potential in the multisphere model. *IEEE Trans. on Biomed. Engin.*, 40(11):1163–1174, 1993.

[25] A. Dervieux and F. Thomasset. A finite element method for the simulation of Rayleigh-Taylor instability. *Lecture Notes in Mathematics*, 771:145–159, 1979.

[26] A. S. Ferguson, X. Zhang, and G. Stroink. A complete linear discretization for calculating the magnetic field using the boundary element method. *IEEE Trans. Biomed. Eng.*, 41(5):455–459, May 1994.

[27] T.C. Ferree, K.J. Eriksen, and D.M. Tucker. Regional head tissue conductivity estimation for improved EEG analysis. *IEEE Transactions on Biomedical Engineering*, 47(12):1584–1592, December 2000.

[28] W.J. Freeman. Simulation of chaotic eeg patterns with a dynamic model of the olfactory system. *Biological Cybernetics*, 56:139–150, 1987.

[29] C. Gabriel, S. Gabriel, and E. Corthout. The dielectric properties of biological tissues: I. literature survey. *Physics in Medicine and Biology*, 41:2231–2249, 1996.

[30] S. Gabriel, R.W. Lau, and C. Gabriel. The dielectric properties of biological tissues: Ii. measurements in the frequency range 10 hz to 20 ghz. *Physics in Medicine and Biology*, 41:2251–2269, 1996.

[31] N.G. Gençer and C.E. Acar. Sensitivity of eeg and meg measurements to tissue conductivity. *Physics in Medicine and Biology*, 49:701–717, 2004.

[32] D. B. Geselowitz. On bioelectric potentials in an homogeneous volume conductor. *Biophysics Journal*, 7:1–11, 1967.

[33] D. B Geselowitz. On the magnetic field generated outside an inhomogeneous volume conductor by internal volume currents. *IEEE Trans. Magn.*, 6:346–347, 1970.

[34] M.B. Giles and N.A. Pierce. An introduction to the adjoint approach to design. *Flow, Turbulence and Combustion*, 65:393–415, 2000.

[35] R. Goldenberg, R. Kimmel, E. Rivlin, and M. Rudzsky. Cortex segmentation: a fast variational geometric approach. *IEEE Transactions on Medical Imaging*, 21(12):1544–1551, 2002.

[36] J. Gomes and O. Faugeras. Reconciling distance functions and level sets. *Journal of Visual Communication and Image Representation*, 11(2):209–223, 2000.

[37] S. Gonçalves, J.C. de Munck, J.P. Verbunt, R.M. Heethaar, and F.H. Lopes da Silva. In vivo measurement of the brain and skull resistivities using an EIT-based method and the combined analysis of SEF/SEP data. *IEEE Transactions on Biomedical Engineering*, 50(9):1124–8, September 2003.

[38] David Guttiérrez, Arye Nehorai, and Carlos H. Muravchik. Estimating brain conductivities and dipole source signals with EEG arrays. *IEEE Transactions on Biomedical Engineering*, 51(12):2113–2122, December 2004.

[39] H. Hallez, B. Vanrumste, P. Van Hese, Y. D'Asseler, I. Lemahieu, and R. Van de Walle. A finite difference method with reciprocity used to incorporate anisotropy in electroencephalogram dipole source localization. *Physics in Medicine and Biology*, 50:3787–3806, 2005.

[40] M. S. Hämäläinen and J. Sarvas. Realistic conductivity geometry model of the human head for interpretation of neuromagnetic data. *IEEE Trans. Biomed. Eng.*, 36(2):165–171, February 1989.

[41] Matti Hämäläinen, Riitta Hari, Risto J. IImoniemi, Jukka Knuutila, and Olli V. Lounasmaa. Magnetoencephalography— theory, instrumentation, and applications to noninvasive studies of the working human brain. *Reviews of Modern Physics*, 65(2):413–497, April 1993.

[42] M.S. Hämäläinen and R.J. Ilmoniemi. Interpreting magnetic fields of the brain: minimum norm estimates. *Medical and Biological Engineering and Computing*, 32(1):35–42, jan 1994.

[43] X. Han, D.L. Pham, D. Tosun, M.E. Rettmann, C. Xu, and J.L. Prince. CRUISE: Cortical reconstruction using implicit surface evolution. *NeuroImage*, 23(3):997–1012, 2004.

[44] X. Han, C. Xu, and J.L. Prince. A topology preserving level set method for geometric deformable models. 25(6):755–768, 2003.

[45] R. Hari and N. Forss. Magnetoencephalography in the study of human somatosensory cortical processing. *Philos Trans R Soc Lond B Biol Sci*, 354(1387):1145–1154, jul 1999.

[46] J. Haueisen, C. Ramon, M. Eiselt, H. Brauer, and H. Nowak. Influence of tissue resistivities on neuromagnetic fields and electric potentials studied with a finite element model of the head. *IEEE Transactions on Biomedical Engineering*, 44(8):727–735, aug 1997.

[47] X. He, T. Lin, and Y. Lin. Approximation capability of a bilinear immersed finite element space. *Numerical Methods for Partial Differential Equations*, 24(5):1265–1300, 2008.

[48] R. Hoekema, G.H. Wieneke, F.S.S. Leijten, C.W.M van Veelen, P.C. van Rijen, G.J.M. Huiskamp, J. Ansems, , and A.C. van Huffelen. Measurement of the conductivity of skull, temporarily removed during epilepsy surgery. *Brain Topography*, 16(1):29–38, 2003.

[49] G. Huiskamp, M. Vroeijenstijn, R. van Dijk, G. Wieneke, and A. C. van Huffelen. The need for correct realistic geometry in the inverse EEG problem. *IEEE Trans. on Biomed. Engin.*, 46(11):1281–1287, November 1999.

[50] Ben H. Jansen and Vincent G. Rit. Electroencephalogram and visual evoked potential generation in a mathematical model of coupled cortical columns. *Biological Cybernetics*, 73:357–366, 1995.

[51] E.G. Jones and A. Peters, editors. *Cerebral cortex, functional properties of cortical cells*, volume 2. Plenum, New York, 1984.

[52] E.R. Kandel, J.H. Schwartz, and T.M. Jessel. *Principles of Neural Science*. McGraw-Hill, 4th edition, 2000.

[53] R.N. Kavanagh, T.M. Darcey, D. Lehmann, and D.K. Fender. Evaluation of methods for 3-dimensional localization of electrical sources in the human brain. *IEEE Trans Biomed Eng*, 25(5):421–429, 1978.

[54] C. Koch. *Biophysics of Computation: Information Processing in Single Neurons*. Oxford University Press: New York, New York., 1999.

[55] J. Kybic, M. Clerc, T. Abboud, O. Faugeras, R. Keriven, and T. Papadopoulo. A common formalism for the integral formulations of the forward EEG problem. *IEEE Transactions on Medical Imaging*, 24:12–28, jan 2005.

[56] J. Kybic, M. Clerc, O. Faugeras, R. Keriven, and T. Papadopoulo. Generalized head models for MEG/EEG: boundary element method beyond nested volumes. *Physics in Medicine and Biology*, 51:1333–1346, 2006.

[57] Y. Lai, W. Van Drongelen, L. Ding, K.E. Hecox, V.L. Towle, D.M. Frim, and B. He. Estimation of in vivo human brain-to-skull conductivity ratio from simultaneous extra- and intra-cranial electrical potential recordings. *Clinical neurophysiology*, 116(2):456–465, 2005.

[58] R.M. Leahy, J.C. Mosher, M.E. Spencer, M.X. Huang, and J.D. Lewine. A study of dipole localization accuracy for MEG and EEG using a human skull phantom. Los Alamos Technical Report LA-UR-98-1442, Los Alamos National Laboratory, March 1998. Revision of LA-UR-97-4804.

[59] S. Lew, C. Wolters, A. Anwander, S. Makeig, and R. MacLeod. Low resolution conductivity estimation to improve source localization. In International Congress Series, editor, *New Frontiers in Biomagnetism. Proceedings of the 15th International Conference on Biomagnetism*, volume 1300, pages 149–152, 2007.

[60] Choh-luh Li, Anthony F. Bak, and Levon O. Parker. Specific resistivity of the cerebral cortex and white matter. *Experimental Neurology*, 20(4):544–557, 1968.

[61] J.L. Lions. *Optimal control of systems governed by partial differential equations*. Springer, 1971.

[62] Adriano Lopes and Ken Brodlie. Improving the robustness and accuracy of the marching cubes algorithm for isosurfacing. 9:16–29, 2003.

[63] F.H. Lopes da Silva, A. van Rotterdam, P. Barts, E. van Heusden, and W. Burr. Model of neuronal populations. the basic mechanism of rhythmicity. *M.A. Corner, D.F. Swaab (eds) Progress in brain research, Elsevier, Amsterdam*, 45:281–308, 1976.

[64] J.A.V. Malmivuo. Distribution of m.e.g. detector sensitivity: an application of reciprocity. *Medical and Biological Engineering and Computing*, 18(3):365–370, 1980.

[65] Gildas Marin, Christophe Guerin, Sylvain Baillet, Line Garnero, and Gérard Meunier. Influence of skull anisotropy for the forward and inverse problems in EEG: simulation studies using FEM on realistic head models. *Human Brain Mapping*, 6:250–269, 1998.

[66] J. W. H. Meijs and M. Peters. The eeg and meg using a model of eccentric spheres to describe the head. *IEEE Transactions on Biomedical Engineering*, 34:913–920, 1987.

[67] J. W. H. Meijs, O. W. Weier, M. J. Peters, and A. van Oosterom. On the numerical accuracy of the boundary element method. *IEEE Trans. Biomed. Eng.*, 36:1038–1049, 1989.

[68] M.D. Morris. Factorial sampling plans for preliminary computational experiments. *Technometrics*, 33(2):161–174, 1991.

[69] John C. Mosher, Paul S. Lewis, and Richard M. Leahy. Multiple dipole modeling and localization from spatio-temporal MEG data. *IEEE Transactions on Biomedical Engineering*, 39(6):541–553, 1992.

[70] V.B. Mountcastle. Modality and topographic properties of single neurons of cat's somatosensory cortex. *Journal of Neurophysiology*, 20:408–434, 1957.

[71] V.B. Mountcastle. The columnar organization of the neocortex. *Brain*, 120:701–722, 1997.

[72] S. Murakami and Y. Okada. Contributions of principal neocortical neurons to magnetoencephalography and electroencephalography signals. *The Journal of Physiology*, 575(3):925–936, 2006.

[73] H. Niederreiter and J. Spanier. *Monte Carlo and quasi-Monte Carlo methods, 1998*. Springer New York, 1999.

[74] G. Nolte. The magnetic lead field theorem in the quasi-static approximation and its use for magnetoencephalography forward calculation in realistic volume conductors. *Physics in Medicine and Biology*, 48:3637–3652, oct 2003.

[75] John Nolte. *The Human Brain*. Mosby, 5th edition, 2001.

[76] Suk H. Oh, Jae Y. Han, Soo Y. Lee, Min H. Cho, Byung I. Lee, and Eung J. Woo. Electrical conductivity imaging by magnetic resonance electrical impedance tomography (mreit). *Magnetic resonance in medicine*, 50(4):875–878, 2003.

[77] Jorma O. Ollikainen, Marko Vauhkonen, Pasi A. Karjalainen, and Jari P. Kaipio. Effects of electrode properties on eeg measurements and a related inverse problem. *Medical Engineering & Physics*, 22:535–545, oct 2000.

[78] T.F. Oostendorp, J. Delbeke, and D.F. Stegeman. The conductivity of the human skull: Results of *in vivo* and *in vitro* measurements. *IEEE Transactions on Biomedical Engineering*, 47(11):1487–1492, December 2000.

[79] S. Osher and J.A. Sethian. Fronts propagating with curvature-dependent speed: Algorithms based on Hamilton–Jacobi formulations. *Journal of Computational Physics*, 79(1):12–49, 1988.

[80] T. Papadopoulo and S. Vallaghé. Implicit meshing for finite element methods using levelsets. In *Proceedings of MMBIA 07*, 2007.

[81] R.D. Pascual-Marqui, C.M. Michel, and D. Lehmann. Low resolution electromagnetic tomography: a new method for localizing electrical activity in the brain. *International journal of psychophysiology*, 18(1):49–65, 1994.

[82] A. Peters and E.G. Jones, editors. *Cerebral cortex, cellular components of the cerebral cortex*, volume 1. Plenum, New York, 1984.

[83] Ceon Ramon, Paul H. Schimpf, and Jens Haueisen. Influence of head models on eeg simulations and inverse source localizations. *BioMedical Engineering OnLine*, 5(10), 2006.

[84] S. Rush and D.A. Driscoll. Eeg electrode sensitivity - an application of reciprocity. *IEEE Transactions on Biomedical Engineering*, 16(1):15–22, 1969.

[85] H. Saleheen and T. Kwong. New finite difference formulations for general inhomogeneous anisotropic bioelectric problems. *IEEE Transactions on Biomedical Engineering*, 44(9):800–809, 1997.

[86] A. Saltelli, K. Chan, and E.M. Scott. *Sensitivity analysis*. John Wiley & sons, 2000.

[87] A. Saltelli, S. Tarantola, and K.P.-S. Chan. A quantitative model-independent method for global sensitivity analysis of model output. *Technometrics*, 41(1):39–56, 1999.

[88] Jukka Sarvas. Basic mathematical and electromagnetic concepts of the biomagnetic inverse problem. *Phys. Med. Biol.*, 32(1):11–22, 1987.

[89] M. Scherg and D. Von Cramon. Evoked dipole source potentials of the human auditory cortex. *Electroencephalography and clinical neurophysiology*, 65(5):344–360, 1986.

[90] P. H. Schimpf. Application of quasi-static magnetic reciprocity to finite element models of the meg lead-field. *IEEE Transactions on Biomedical Engineering*, 54(11):2082–2088, nov 2007.

[91] P.H. Schimpf, C. Ramon, and J. Haueisen. Dipole models for the eeg and meg. *IEEE Transactions on Biomedical Engineering*, 49(5):409–418, 2002.

[92] M. Schneider. A multistage process for computing virtual dipolar sources of eeg discharges from surface information. *IEEE Trans. on Biomed. Eng.*, 19:1–19, 1972.

[93] F. Ségonne, J.-P. Pons, E. Grimson, and B. Fischl. A novel level set framework for the segmentation of medical images under topology control. In *Workshop on Computer Vision for Biomedical Image Applications: Current Techniques and Future Trends*, 2005.

[94] D.W. Shattuck and R.M. Leahy. Brainsuite: An automated cortical surface identification tool. *Medical Image Analysis*, 6(2):129–142, June 2002.

[95] A.Z. Snyder. Dipole source localization in the study of ep generators : a critique. *Electroencephalography and clinical neurophysiology*, 80(4):321–325, 1991.

[96] I.M. Sobol. Sensitivity estimates for nonlinear mathematical models. *Mathematical Modelling and Computational Experiments*, 1:407–414, 1993.

[97] Erkki Somersalo, Margaret Cheney, and David Isaacson. Existence and uniqueness for electrode models for electric current computed tomography. *SIAM Journal on Applied Mathematics*, 52(4):1023–1040, aug 1992.

[98] P. Suffczynski, S. Kalitzin, G. Pfurtscheller, and FH Lopes da Silva. Computational model of thalamo-cortical networks: dynamical control of alpha rhythms in relation to focal attention. *International Journal of Psychophysiology*, 43(1):25–40, 2001.

[99] W.W. Sutherling, Crandall P.H., Cahan L.D., and Barth D.S. The magnetic field of epileptic spikes agrees with intracranial localizations in complex partial epilepsy. *Neurology*, 38(5):778–786, 1988.

[100] D.S Tuch, V.J. Wedeen, A.M. Dale, J.S. George, and J.W. Belliveau. Conductivity tensor mapping of the human brain using diffusion tensor MRI. In *Proceedings of the National Academy of Sciences*, volume 98, pages 11697–11701, 2001.

[101] S. Vallaghé, M. Clerc, and J.M. Badier. In vivo conductivity estimation using somatosensory evoked potentials and cortical constraint on the source. In *Proceedings of ISBI 2007*, pages 1036–1039, apr 2007.

[102] M.J. Van Burik and M.J. Peters. Estimation of the electric conductivity from scalp measurements : feasibility and application to source localization. *Clinical neurophysiology*, 111(8):1514–1521, 2000.

[103] B.D. Van Veen and K.M. Buckley. Beamforming: a versatile approach to spatial filtering. *IEEE Acoustics, Speech, Signal Processing Mag.*, 5:4–24, apr 1988.

[104] N. von Ellenrieder, C. Muravchik, and A. Nehorai. Effect of geometric head model perturbationson the EEG inverse problem. *IEEE Transactions on Biomedical Engineering*, 53(3):421–429, 2006.

[105] D. Weinstein, L. Zhukov, and C. Johnson. Lead-field bases for electroencephalography source imaging. *Annals of Biomedical Engineering*, 28(9):1059–1164, sep 2000.

[106] K. Wendel, N.G. Narra, M. Hannula, P. Kauppinen, and J. Malmivuo. The influence of csf on eeg sensitivity distributions of multilayered head models. *IEEE Transactions on Biomedical Engineering*, 55(4):1454–1456, 2008.

[107] F. Wendling, J.J. Bellanger, F. Bartolomei, and P. Chauvel. Relevance of nonlinear lumped-parameter models in the analysis of depth-eeg epileptic signals. *Biological Cybernetics*, 83:367–378, 2000.

[108] S. J. Williamson and L. Kaufman. Biomagnetism. *Journal of Magnetism and Magnetic Materials*, 22(2):129–201, 1981.

[109] C. H. Wolters, A. Anwander, X. Tricoche, D. Weinstein, M. A. Koch, and R. MacLeod. Influence of tissue conductivity anisotropy on EEG/MEG field and return current computation in a realistic head model: A simulation and visualization study using high-resolution finite element modeling. *NeuroImage*, (3):813–826, 2006.

[110] C. H. Wolters, L. Grasedyck, and W. Hackbusch. Efficient computation of lead field bases and influence matrix for the fem-based eeg and meg inverse problem. *Inverse Problems*, 20:1099–1116, 2004.

[111] CH Wolters, A. Anwander, G. Berti, and U. Hartmann. Geometry-adapted hexahedral meshes improve accuracy of finite-element-method-based eeg source analysis. *Biomedical Engineering, IEEE Transactions on*, 54(8):1446–1453, 2007.

[112] CH Wolters, H. Köstler, C. Möller, J. Härdtlein, L. Grasedyck, and W. Hackbusch. Numerical mathematics of the subtraction method for the modeling of a current dipole in eeg source reconstruction using finite element head models. *SIAM Journal on Scientific Computing*, 30:24, 2007.

[113] M. Yedlin, H. Kwan, J.T. Murphy, H. Nguyen-Huu, and Y.C. Wong. Electrical conductivity in cat cerebellar cortex. *Experimental Neurology*, 43(3):555–569, 1974.

[114] B. Yvert, O. Bertrand, J.-F. Echallier, and J. Pernier. A systematic evaluation of the spherical model accuracy in eeg dipole localization. *Electroenceph clin Neurophysiol*, 102:452–459, 1997.

[115] X. Zeng, L.H. Staib, R.T. Schultz, and J.S. Duncan. Segmentation and measurement of the cortex from 3D MR images using coupled surfaces propagation. *IEEE Transactions on Medical Imaging*, 18(10):100–111, 1999.

[116] LH Zetterberg, L. Kristiansson, and K. Mossberg. Performance of a model for a local neuron population. *Biological Cybernetics*, 31(1):15–26, 1978.

[117] Y.C. Zhang, W. van Drongelen, and B. He. Estimation of in vivo brain-to-skull conductivity ratio in humans. *Applied physics letters*, 89(22), 2006.

[118] Zhi Zhang. A fast method to compute surface potentials generated by dipoles within multilayer anisotropic spheres. *Phys. Med. Biol.*, 40:335–349, 1995.

[119] O.C. Zienkiewicz and R.L. Taylor. *The Finite element method, 4th ed.* Mac Graw Hill, 1987.